sid.inpe.br/mtc-m19/2010/10.07.02.39-TDI

NUMERICAL INVESTIGATION OF AEROTHERMODYNAMIC IN A REENTRY VEHICLE WITH SURFACE DISCONTINUITY-LIKE CAVITY

Rodrigo Cassineli Palharini

Master Thesis at Post Graduation Course in Engineering and Space Technology/Combustion and Propulsion, advised by Dr. Wilson Fernando Nogueira dos Santos, approved in October 21, 2010.

URL do documento original:
<http://urlib.net/8JMKD3MGP7W/38CL3PB >

INPE
São José dos Campos
2010

PUBLISHED BY:

Instituto Nacional de Pesquisas Espaciais - INPE
Gabinete do Diretor (GB)
Serviço de Informação e Documentação (SID)
Caixa Postal 515 - CEP 12.245-970
São José dos Campos - SP - Brasil
Tel.:(012) 3208-6923/6921
Fax: (012) 3208-6919
E-mail: pubtc@sid.inpe.br

CONSELHO DE EDITORAÇÃO E PRESERVAÇÃO DA PRODUÇÃO INTELECTUAL DO INPE (RE/DIR-204):
Presidente:
Dr. Gerald Jean Francis Banon - Coordenação Observação da Terra (OBT)
Membros:
Drª Inez Staciarini Batista - Coordenação Ciências Espaciais e Atmosféricas (CEA)
Drª Maria do Carmo de Andrade Nono - Conselho de Pós-Graduação
Drª Regina Célia dos Santos Alvalá - Centro de Ciência do Sistema Terrestre (CST)
Marciana Leite Ribeiro - Serviço de Informação e Documentação (SID)
Dr. Ralf Gielow - Centro de Previsão de Tempo e Estudos Climáticos (CPT)
Dr. Wilson Yamaguti - Coordenação Engenharia e Tecnologia Espacial (ETE)
Dr. Horácio Hideki Yanasse - Centro de Tecnologias Especiais (CTE)
BIBLIOTECA DIGITAL:
Dr. Gerald Jean Francis Banon - Coordenação de Observação da Terra (OBT)
Marciana Leite Ribeiro - Serviço de Informação e Documentação (SID)
Deicy Farabello - Centro de Previsão de Tempo e Estudos Climáticos (CPT)

REVISÃO E NORMALIZAÇÃO DOCUMENTÁRIA:
Marciana Leite Ribeiro - Serviço de Informação e Documentação (SID)
Yolanda Ribeiro da Silva Souza - Serviço de Informação e Documentação (SID)
EDITORAÇÃO ELETRÔNICA:
Vivéca Sant´Ana Lemos - Serviço de Informação e Documentação (SID)

Ministério da
Ciência e Tecnologia

UM PAÍS DE TODOS
GOVERNO FEDERAL

sid.inpe.br/mtc-m19/2010/10.07.02.39-TDI

NUMERICAL INVESTIGATION OF AEROTHERMODYNAMIC IN A REENTRY VEHICLE WITH SURFACE DISCONTINUITY-LIKE CAVITY

Rodrigo Cassineli Palharini

Master Thesis at Post Graduation Course in Engineering and Space Technology/Combustion and Propulsion, advised by Dr. Wilson Fernando Nogueira dos Santos, approved in October 21, 2010.

URL do documento original:
<http://urlib.net/8JMKD3MGP7W/38CL3PB >

INPE
São José dos Campos
2010

Dados Internacionais de Catalogação na Publicação (CIP)

Palharini, Rodrigo Cassineli.
P176n Numerical investigation of aerothermodynamic in a reentry vehicle with surface discontinuity-like cavity / Rodrigo Cassineli Palharini. – São José dos Campos : INPE, 2010.
xxvi+127 p. ; (sid.inpe.br/mtc-m19/2010/10.07.02.39-TDI)

Master Thesis (Master Thesis in Space Technology) – Instituto Nacional de Pesquisas Espaciais, São José dos Campos, 2010.
Adviser : Dr. Wilson Fernando Nogueira dos Santos.

1. Aerothermodynamics. 2. Direct Simulation Monte Carlo Method (DSMC). 3. Rarefied hypersonic flow. 4. Atmospheric reentry. 5. Cavity. 6. Aerodynamic heating. I.Título.

CDU 629.7

Copyright © 2010 do MCT/INPE. Nenhuma parte desta publicação pode ser reproduzida, armazenada em um sistema de recuperação, ou transmitida sob qualquer forma ou por qualquer meio, eletrônico, mecânico, fotográfico, reprográfico, de microfilmagem ou outros, sem a permissão escrita do INPE, com exceção de qualquer material fornecido especificamente com o propósito de ser entrado e executado num sistema computacional, para o uso exclusivo do leitor da obra.

Copyright © 2010 by MCT/INPE. No part of this publication may be reproduced, stored in a retrieval system, or transmitted in any form or by any means, electronic, mechanical, photocopying, recording, microfilming, or otherwise, without written permission from INPE, with the exception of any material supplied specifically for the purpose of being entered and executed on a computer system, for exclusive use of the reader of the work.

Aprovado (a) pela Banca Examinadora em cumprimento ao requisito exigido para obtenção do Título de Mestre **em**

Engenharia e Tecnologia
Espaciais/Combustão e Propulsão

Dr. Wilson Fernando Nogueira dos Santos

Presidente / Orientador(a) / INPE / Cachoeira Paulista - SP

Dr. Marcio Teixeira de Mendonça

Membro da Banca / IAE/CTA / SJCampos - SP

Dr. Algacyr Morgenstern Júnior

Convidado(a) / IAE/CTA / São José dos Campos - SP

Aluno (a): Rodrigo Cassinelli Palharini

São José dos Campos, 21 de outubro de 2010

“The World is Made by Men and Books”.

MONTEIRO LOBATO

To my parents Darli and Cleide, to my brother Marcelo
and my advisor Wilson

ACKNOWLEDGEMENTS

Firstly, I would like to thank God that allowed me study and improve my knowledge today and always, with all your protection and presence in the most requested moments in my life. I´m grateful to my family for believing in me, support and incentives my victories and always being there for me when I really needed.

To Dr. Wilson F. N. Santos, my advisor, whom I have great admiration and respect, thank you for having awakened me the scientific spirit. Thanks for the personal and professional support, the patience, your lessons have helped me grow and improve as a person, friend and researcher, and also by the constant willingness to help me.

To my true friends, especially Luis Thiago Lucci and Cesar Alejandro Quispe, who directly or indirectly always help me, either with a hint, an encouragement, a laugh in stress times or even with affection at times of sadness.

Thanks to my teachers at the National Institute for Space Research (INPE) than with their knowledge, they formed the basis for the development of this research work.

To all who participated behind the scenes of this project, Mr. Otavio, Maria Aparecida, Maria Ignês, whose yours function were of great importance for the development of this thesis.

To the examiners members for the predisposition in examining this work and suggestions.

I thanks to the Fundação de Amparo à Pesquisa do Estado de São Paulo (FAPESP) for financial support during the development of the Masters course.

INVESTIGAÇÃO NUMÉRICA DA AEROTERMODINÂMICA DE VEÍCULOS NA REENTRADA COM IMPERFEIÇÕES NA SUPERFÍCIE DO TIPO CAVIDADE

RESUMO

No projeto de veículos hipersônicos, o conhecimento dos fatores que afetam as cargas térmicas e aerodinâmicas que agem na superfície do veículo se torna imperativo. Usualmente, no cálculo das cargas térmicas, a análise assume que o veículo possui uma superfície livre de imperfeições ou descontinuidades. No entanto, imperfeições ou descontinuidades estão presentes na superfície de veículos na reentrada visando atender diferentes propósitos. Neste cenário, um estudo numérico é realizado com o propósito de examinar o impacto de cavidades na estrutura do escoamento e nas propriedades aerodinâmicas na superfície de veículos na reentrada, sob condições de escoamento hipersônico rarefeito. A análise foi realizada por um código computacional robusto que leva em conta os efeitos de não-equilíbrio térmico. Uma descrição detalhada do impacto nas propriedades do escoamento – velocidade, massa específica, pressão e temperatura – bem como nas propriedades aerodinâmicas na superfície – fluxo de moléculas, transferência de calor, pressão e atrito – é apresentada para seções nas vizinhanças das cavidades devido as variações na razão largura-profundidade (L/H). A analise mostrou que as recirculações dentro das cavidades são funções da razão L/H. Nos casos onde $L/H < 3$, a estrutura do escoamento sobre as cavidades representa aquela observada para "open cavity". Entretanto, para o caso onde $L/H = 4$, a estrutura do escoamento corresponde a uma "closed cavity". As propriedade aerodinâmicas também foram apresentadas e os maiores valores foram obtidos para a face a montante da cavidade, mais precisamente, na quina das cavidades. A análise mostrou, também, que as cargas aerodinâmicas obtidas são muito maiores a aquelas observadas para uma superfície livre de discontinuidades.

ABSTRACT

In the design of hypersonic vehicles, the knowledge of factors that affects the thermal and aerodynamic loads acting on the vehicle surface becomes imperative. Usually, in the thermal load calculations, the analysis assumes that the vehicle has a smooth surface. However, discontinuities or imperfections are present on the surface of reentry vehicles. In this scenario, a numerical study was performed with the purpose to examine the impact of cavities on the flowfield structure and on the aerodynamic properties on the reentry vehicle surfaces, under conditions of rarefied hypersonic flow. The calculations were performed with a robust computer code that takes into account for the effects of thermodynamic non-equilibrium. A detailed description of the impact on the flowfield properties – velocity, density, pressure and temperature – as well as the aerodynamic properties on the surface – number flux, heat transfer, pressure and skin friction – is presented at the vicinity of the cavities due to variations in the width-to-depth (L/H) ratio. The analysis showed that the recirculation region inside the cavities is a function of the L/H ratio. It was found that, for $L/H < 3$, the cavity flow structure represented that one observed in a "open cavity". Conversely, for $L/H = 4$, the cavity flow structure corresponded to that of a "closed cavity". In contrast, for the aerodynamic quantities acting on the cavity surface, it was found that the pressure load and the heat load presented the maximum values along the cavity downstream faces, more precisely, at the shoulder of the cavities. In addition, these loads are much larger than those attained in a smooth surface.

LIST OF FIGURES

Pág.

1.1 X-38 vehicle leading edge. 2
1.2 (a) Space Shuttle configuration (b) Damage site location. 2
1.3 Flow regimes as a function of the Knudsen number. 4
1.4 Flowfield structure in cavities. 8

2.1 Regimes of applicability of conventional mathematical models as a function of the local Knudsen number (adapted from (BIRD, 1994)). 12
2.2 Flowchart of the DSMC method. 18
2.3 Schematic drawing illustrating the analysis of binary collisions. (a) Planar representation of a collision in the laboratory frame of reference. (b) Binary collision in the center of mass frame of reference (c) Interaction of reduced mass particle with a fixed scattering center (Adapted from Bird (1994)). 29
2.4 Maxwell model of reflection. 33

3.1 Drawing illustrating the cavity. 35
3.2 Drawing illustrating the computational domain. 38

4.1 Drawing illustrating the flat-plate computational domain. 45
4.2 Effect of changing the cell size (x-coordinate direction) on skin friction (top), pressure (middle), and heat transfer (bottom) coefficients. 47
4.3 Effect of changing the cell size (y-coordinate direction) on skin friction (top), pressure (middle), and heat transfer (bottom) coefficients. 48
4.4 Effect of changing the number of molecules on skin friction (top), pressure (middle), and heat transfer (bottom) coefficients. 50
4.5 Effect of changing the flat-plate length on skin friction (top), pressure (middle), and heat transfer (bottom) coefficients. 51
4.6 Density ratio (ρ/ρ_∞) profiles normal to the flat-plate surface for various stations along the flat plate. Solid lines represent the present DSMC simulations, full and empty symbols represent experimental and numerical data, respectively. 55

4.7 Velocity ratio (u/U_∞) profiles normal to the flat-plate surface for various stations along the flat plate. Solid lines represent the present DSMC simulations, full and empty symbols represent experimental and numerical data, respectively. 56
4.8 Temperature ratio (T/T_∞) profiles normal to the flat-plate surface for various stations along the flat plate. Solid lines represent the present DSMC simulations, full and empty symbols represent experimental and numerical data, respectively. 57
4.9 Density ratio (ρ/ρ_∞) profiles along the flat-plate surface at station $y =$ 1.25mm. Solid lines represent the present DSMC simulations, full and empty symbols represent experimental and numerical data, respectively. . 58
4.10 Velocity ratio (u/U_∞) profile along the flat-plate surface at a station $y = 1.25$mm. Solid lines represent the present DSMC simulations, full and empty symbols represent experimental and numerical data, respectively. . 58
4.11 Temperature ratio (T/T_∞) profile along the flat-plate surface at a station $y = 1.25$mm. Solid lines represent the present DSMC simulations, full and empty symbols represent experimental and numerical data, respectively. . 59
4.12 Effect of changing the cell size (x-coordinate direction) on the skin friction coefficient for the $L/H = 1$ case. 62
4.13 Effect of changing the cell size (x-coordinate direction) on the pressure coefficient for the $L/H = 1$ case. 63
4.14 Effect of changing the cell size (x-coordinate direction) on the heat transfer coefficient for the $L/H = 1$ case. 64
4.15 Effect of changing the cell size (y-coordinate direction) on the skin friction coefficient for the $L/H = 1$ case. 65
4.16 Effect of changing the cell size (y-coordinate direction) on the pressure coefficient for the $L/H = 1$ case. 66
4.17 Effect of changing the cell size (y-coordinate direction) on the heat transfer coefficient for the $L/H = 1$ case. 67
4.18 Effect of changing the number of molecules on the skin friction coefficient for the $L/H = 1$ case. 68
4.19 Effect of changing the number of molecules on the pressure coefficient for the $L/H = 1$ case. 69
4.20 Effect of changing the number of molecules on the heat transfer coefficient for the $L/H = 1$ case. 70
4.21 Drawing illustrating the computational domain (left) and a magnified view of the cavity (right) for the $L/H = 1$ case. 71

5.1 Tangential velocity ratio (u/U_∞) profiles for three sections along the surface $S1$ parameterized by the L/H ratio. 77
5.2 Tangential velocity ratio (u/U_∞) profiles for three sections along the surface $S5$ parameterized by the L/H ratio. 78
5.3 Tangential velocity ratio (u/U_∞) profiles for three sections along the surface $S3$ parameterized by the L/H ratio. 79
5.4 Normal velocity ratio (v/U_∞) profiles for three transversal sections inside the cavity as a function of the dimensionless length X'_L. 80
5.5 Distribution of streamline traces inside the cavities for L/H of 1, 2, 3 and 4. 81
5.6 Mach number distribution outside (left) and inside (right) the cavities for L/H ratio of 1, 2, 3 and 4. 82
5.7 Density ratio (ρ/ρ_∞) profiles for three sections along the cavity surface $S1$ parameterized by the L/H ratio. 86
5.8 Density ratio (ρ/ρ_∞) profiles for three sections along the cavity surface $S5$ parameterized by the L/H ratio. 87
5.9 Density ratio (ρ/ρ_∞) profiles for three sections along the cavity surface $S3$ parameterized by the L/H ratio. 88
5.10 Density ratio (ρ/ρ_∞) distribution outside (left) and inside (right) the cavities for L/H ratio of 1, 2, 3 and 4. 89
5.11 Pressure ratio (p/p_∞) profiles for three sections along the cavity surface $S1$ parameterized by the L/H ratio. 92
5.12 Pressure ratio (p/p_∞) profiles for three sections along the cavity surface $S5$ parameterized by the L/H ratio. 93
5.13 Pressure ratio (p/p_∞) profiles for three sections along the cavity surface $S3$ parameterized by the L/H ratio. 94
5.14 Pressure ratio (p/p_∞) distribution outside (left) and inside (right) the cavities for L/H ratio of 1, 2, 3 and 4. 95
5.15 Kinetic temperature ratio (T/T_∞) profiles for three sections along the cavity surface $S1$ parameterized by the L/H ratio. 100
5.16 Kinetic temperature ratio (T/T_∞) profiles for three sections along the cavity surface $S5$ parameterized by the L/H ratio. 101
5.17 Kinetic temperature ratio (T/T_∞) profiles for three sections along the cavity surface $S3$ parameterized by the L/H ratio. 102
5.18 Translational temperature ratio (T_T/T_∞) distribution outside (left) and inside (right) the cavities for L/H ratio of 1, 2, 3 and 4. 103

5.19 Dimensionless number flux N_f distribution along the cavity surfaces as a function of the L/H ratio. 106
5.20 Heat transfer coefficient C_h distribution along the cavity surfaces as a function of the L/H ratio. 110
5.21 Pressure coefficient C_p along the cavity surfaces as a function of the L/H ratio. 113
5.22 Skin friction coefficient C_f distribution along the cavity surfaces as a function of the L/H ratio. 116

LIST OF TABLES

Pág.

3.1 Characteristics of simulated air for DSMC calculations. 37
3.2 Freestream flow conditions. 39

4.1 Freestream main properties. 45
4.2 Number of cells in the (x-direction) and [y-direction] for the flat-plate case. 46
4.3 Number of cells in the (x-direction) and [y-direction] for the L/H=1 case. 60

LIST OF ABBREVIATIONS

CLL – Cercignani-Lamps-Lord reflection model
DCTA – Departamento de Ciência e Tecnologia Espacial
DNI – Direct Numerical Integration method
DSMC – Direct Simulation Monte Carlo method
GHS – Generalized Hard Sphere molecular model
HS – Hard Sphere molecular model
IAE – Instituto de Aeronáutica e Espaço
MD – Molecular Dynamics method
NTC – No-Time-Counter technique
NC – Null-Collisions technique
SARA – SAtélite Recuperável Atmosférico
SHO – Simple Harmonic Oscillator model
TC – Time-Counter technique
TP – Test Particle method
VHS – Variable Hard Sphere molecular model
VSS – Variable Soft Sphere molecular model

LIST OF SYMBOLS

a – speed of sound, m/s
C_f – skin friction coefficient, $\tau_w/(1/2\rho_\infty U_\infty^2)$
C_h – heat transfer coefficient, $q_w/(1/2\rho_\infty U_\infty^3)$
C_p – pressure coefficient, $p_w - p_\infty/(1/2\rho_\infty U_\infty^2)$
$\mathbf{c}$ – molecular velocity vector, m/s
c_r – relative speed, m/s
d – molecular diameter, m
e – specific energy, J/kg
F_N – simulated molecules, *dimensionless*
F_n – intermolecular force, N
f – fraction of molecules reflected diffusely, *dimensionless*
H – cavity depth, λ
Kn – Knudsen number, λ/l
L – cavity length, λ
l – characteristic length, m
M – Mach number, U/a
m – mass, kg
N – number of simulated molecules, *dimensionless*
N_f – number flux, *dimensionless*
n – number density, m^{-3}
P – collision probability, *dimensioless*
p – pressure, N/m^2
q – heat flux, W/m^2
R – gas constant, $J/Kmol$
Re – Reynolds number, $\rho Vl/\mu$
R_f – random function, *dimensionless*
T – temperature, K
U – velocity, m/s
u – tangential velocity, m/s
V_c – volume of the cell, m^3
v – normal velocity, m/s
W – cavity width, λ
Z – collision number, τ/τ_c

Greek Sybols

α – angle of attack, *degree*
ζ – degree of freedom, *dimensioless*
κ – Boltzmann constant, J/K
λ – mean free path, m

μ – dynamic viscosity, $kg/(ms)$
ρ – density, kg/m^3
σ – collision cross section, m
τ – relaxation time, s
τ_c – mean collision time, s
ϕ – average probability of energy exchange, *dimensionless*
$\dot{r}$ – dr/dt, m/s
$\ddot{r}$ – d^2r/dt^2, m/s^2
$\triangle t$ – time step, s

Subscripts

d – refers to downstream surface
i – refers to incident molecule
m – refers to center of mass
R – refers to rotational energy
r – refers to reflected molecule
ref – reference value
u – refers to upstream surface
V – refers to vibrational energy
w – wall conditions
∞ – freestream conditions

CONTENTS

Pág.

1 INTRODUCTION 1
1.1 Motivation 1
1.2 Reentry Flow Regimes 2
1.3 Previous Contributions 4
1.4 Present Work 8

2 COMPUTATIONAL METHOD 11
2.1 Methods for Flows in Transition Regime 11
2.2 Direct Simulation Monte Carlo (DSMC) Method 15
2.2.1 DSMC Methodology 17
2.2.2 Molecular Model 19
2.2.3 Collision Model 24
2.2.4 Binary Elastic Collisions 26
2.2.5 Internal Degrees of Freedom 30
2.2.6 Boundary Conditions 32

3 COMPUTATIONAL PROCEDURE 35
3.1 Geometry Definition 35
3.2 Computational Conditions 36
3.3 Freestream and Flow Conditions 38

4 VERIFICATION AND VALIDATION 41
4.1 Computer Requirements 41
4.2 Computational Mesh 43
4.3 Adaptation of the Computational Mesh 44
4.4 DSMC Test Case 44
4.4.1 Effect of Mesh Resolution 46
4.4.2 Effect of Changing Number of Molecules 49
4.4.3 Effect of Downstream Boundary Condition 49
4.4.4 Experimental and Numerical Comparison 52
4.5 Cavity Case 60

5 COMPUTATIONAL RESULTS AND DISCUSSIONS 73
5.1 Flowfield Structure 73
5.1.1 Velocity Field 73
5.1.2 Density Field 83
5.1.3 Pressure Field 90
5.1.4 Kinetic Temperature Field 96
5.2 Aerodynamic Surface Quantities 104
5.2.1 Number Flux 104
5.2.2 Heat Transfer Coefficient 107
5.2.3 Coefficient of Pressure 111
5.2.4 Skin Friction Coefficient 114

6 CONCLUSIONS 117
6.1 Concluding Remark 117
6.2 Future Work 118

REFERENCES 119

1 INTRODUCTION

1.1 Motivation

In the design and development of hypersonic vehicles, the knowledge of factors affecting the mechanical and thermal loads acting on the reentry vehicle surfaces becomes imperative. Usually, in the thermal load calculation, the analysis assumes that the vehicle has a smooth surface. However, discontinuities or imperfections, such as cavities, gaps or steps, are often present on the aerospace vehicle surfaces due to fabrication tolerances, sensor installations, space between the thermal protection plates, and differential expansion or ablation rates between nonsimilar materials (BERTRAN et al., 1967; BERTRAN M. H.; WIGGS, 1963; HAHN, 1969; JAKUBOWKI A. K.; LEWIS, 1973; MORGENSTERN A.; CHOKANI, 1994; NESTLER et al., 1969; NESTLER, 1982). Such surface discontinuities constitute a potential source of premature transition, from laminar to turbulent, and increased heating.

The flow inside cavities and gaps or around steps can be complex due to pressure gradients (EVERHART et al., 2006), to the fluid structure interaction (HINDERSKS M.; RADESPIEL, 2006), and to others aspects. Moreover, the flow configuration becomes more complex if the vehicle structure is deformed by thermal or mechanical loads. These thermal or mechanical loads may cause significant changes in the dimensions of cavities, gaps or steps between the thermal protection plates located on the vehicle surface. Consequently, such modifications in the geometry of the vehicle can lead to the appearance of stagnation points, hot spots, flow separation or affect the boundary layer transition. The thermal protection system of reentry vehicles, such as that in the space shuttle or in the space vehicle X-38, shown in Figure 1.1, requires cavities and gaps between the ceramic tails in order to compensate the thermal expansion of the material. In this context, a detailed prediction of the flow conditions and the thermal loads due to the presence of cavities, gaps or steps in the thermal protection system becomes necessary.

According to the final report of the Columbia Accident Investigation Board (CAIB) (EVERHART et al., 2006), the probable event resulting in the loss of the space shuttle Columbia, during flight STS-107 on February 1, 2003, was identified as a breach in the thermal protection system of the leading edge of the left wing, caused by a peace of insulation foam, as shown in Figure 1.2.

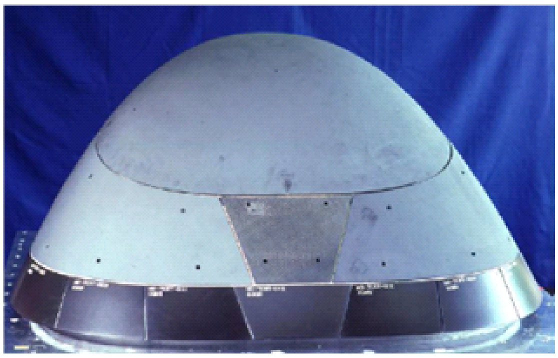

FIGURE 1.1 - X-38 vehicle leading edge.

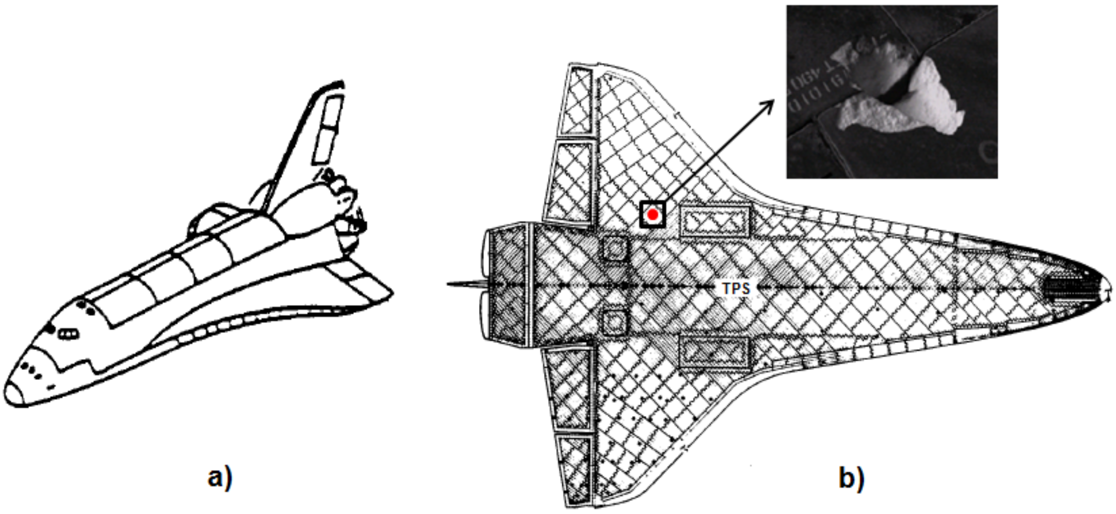

FIGURE 1.2 - (a) Space Shuttle configuration (b) Damage site location.

This example highlight the importance of cavity flow phenomena and their sensitivities. In addition, it indicates that an accurate determination of aerothermodynamic loads is a necessary requirement for an optimal design of reentry vehicles.

1.2 Reentry Flow Regimes

Space vehicles reentering in the Earth´s atmosphere undergo not only different velocity regimes, hypersonic, supersonic and subsonic, but also different flow regimes, free molecular flow, transition and continuum, and flight conditions that may difficult their aerodynamic design. Important physical interactions arise between the vehicle and the environment around the space vehicle. At the highest altitudes, the interaction of the vehicle with the atmospheric air is characterized by the free molecular flow. In this regime, the molecules of the environment collide with the vehicle surface, interact with the surface and are reflected from the surface. Moreover, collisions of reflected molecules with incoming molecules from the freestream are not frequently in this flow regime. As a result, they are ignored.

As the vehicle enters a little deeper into the Earth´s atmosphere, the mean free path between incoming freestream molecules decreases, and collisions between molecules reflected from the vehicle surface and the molecules incoming from the freestream can no longer be ignored. As a result, the flow in this condition defines the transition flow regime, i.e., transition between the collisionless flow regime and the continuum flow regime. In the transition flow regime, the contribution of aerodynamic forces and heat flux to the vehicle surface start to increase rapidly with decreasing altitude, causing large changes in the aerodynamic characteristics of the vehicle when compared with those observed in the free molecular flow. As the vehicle continues to enter into the atmosphere, it finally reaches the continuum flow regime. In this regime, the flow around the vehicle is treated by a macroscopic model that considers the air as a continuum, and the description of the flow is made in terms of spatial and temporal variations of the primary properties, such as velocity, pressure, density and temperature.

The basic criterion that determines the flow regime – collisionless, transition or continuum – is given by the Knudsen number as follows,

$$Kn = \frac{\lambda}{l} \tag{1.1}$$

where λ is the mean free path traveled by molecules between collisions and l is a characteristic length of the body.

A flow is defined in the continuum regime when the Knudsen number tends to zero. On the other hand, a flow is defined in the free molecular flow as the Knudsen number goes to infinity. Figure 1.3 presents the classification of flow regimes as a function of the local Knudsen number.

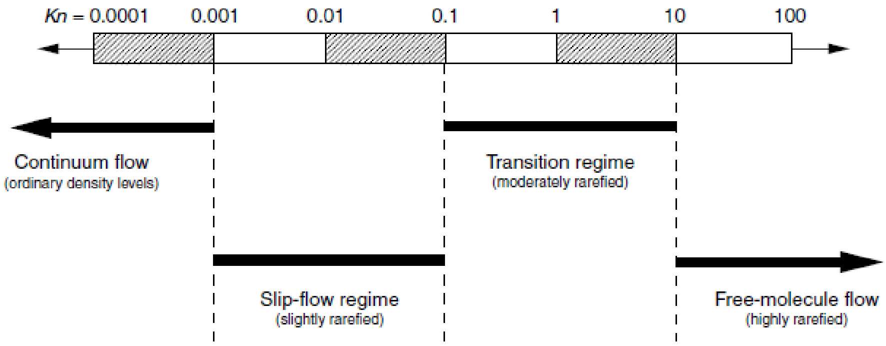

FIGURE 1.3 - Flow regimes as a function of the Knudsen number.

The flow regimes are identified to provide guidance on the required equation sets and physical models for a numerical simulation (ANDERSON, 1989). For instance, for flows around reentry vehicles in the range from 120 to 60 km of altitude, the molecular mean free path λ may be of the order of the dimensions related to the discontinuities on the vehicle surfaces. In such a circumstance, the Knudsen number, which indicates the degree of flow rarefaction, may be in the range of the transition flow regime, i.e., between the continuum regime and the collisionless regime. The dimensions of the imperfections or discontinuities on the surface, the depth H and the width L for cavities or gaps, are usually on the order of 3 to 6 mm (EVERHART et al., 2006; GAI S.; MILTHORPE, 1995). Therefore, as a base of comparison, for 90, 80, 70, and 60 km of altitude, the molecular mean free path λ is 26.03, 4.11, 0.929, and 0.265 mm, respectively. As a result, for H (or L) of 3 mm, the global Knudsen number is the order of 8.67, 1.37, 0.31, and 0.088, for altitudes of 90, 80, 70 and 60 km, respectively. By considering H (or L) of 6 mm, the global Knudsen number is reduced by half. In this scenario, the Knudsen number is in the transitional flow regime, usually defined by the range $0.1 < Kn < 10$. In the transitional flow regime, the concepts of the continuum hypothesis do not apply and the molecular structure of the gas must be considered.

1.3 Previous Contributions

Flows on cavities, gaps, or steps, which are found in many engineering applications, have been investigated for several decades. In aerospace engineering, cavities, gaps or steps appear as design features in modern aerodynamic configurations. Several experimental and numerical studies (CHAPMAN et al., 1958; BERTRAN M. H.; WIGGS, 1963;

CHARWAT et al., 1961a; CHARWAT et al., 1961b; BERTRAN et al., 1967; CHARBONNIER J.; BOERRIGTER, 1993; HAHN, 1969; NESTLER et al., 1969; CHARWAT, 1971; PLENTOVICH et al., 1993; MORGENSTERN A.; CHOKANI, 1994; GAI S.; MILTHORPE, 1995; GROTOWSKY I. M. G.; BALLMANN, 2000; JACKSON et al., 2001; HOZUMI et al., 2004; EVERHART et al., 2006; HINDERSKS M.; RADESPIEL, 2004; HINDERSKS M.; RADESPIEL, 2006; SHANKAR P. N.; DESHPANDE, 2000; ZDANSKI et al., 2004; NARIS S.; VALOUGEORGIS, 2005; LEE G.; CHANDRA, 2006; ROWLEY, 2000; CHENG M.; HUNG, 2006; EVERHART et al., 2006) have been conducted with the purpose of investigating the impact on the flowfield structure of aerospace vehicles due to discontinuities or imperfections present on the surface of such vehicles. For the purpose of this introduction, only a few of these studies will be discussed below.

Charwat et al. (1961a,b) performed a comprehensive study of a low supersonic cavity flow, $M_\infty \sim 3$, and postulated and verified the existence of an alternative emptying and filling of the cavity. Local heat flux to the cavity floor was investigated. Their heat transfer measurements were made by a steady-state technique by utilizing an estimative recovery temperature.

Bertran and Wiggs (1963) have investigated experimentally the effect of distortions, consisting of slots, small steps and local curvatures, on the wing of a hypersonic vehicle. The effect of distortions in the distribution of pressure and heat flux to the surface was investigated for Mach numbers of 7 and 10, and angles of attack up to 20 degrees. According to the results, the surface distortions had a much smaller effect on local pressure than on the local heating. The study showed that all the distortions investigated caused at least high local increase in aerodynamic heating.

An experimental study of the flowfield structure and wall heat transfer within the separated flow region of an annular cavity was investigated by Hahn (HAHN, 1969). Tests were conducted at a freestream Mach number of 7.3, total temperature of 1110K, wall total temperature ratio of 0.26, freestream Reynolds number per meter ranged from 1.6 to 6.3x10^6, and length-to-depth ratio of 5.33, 8.0 and 10.67. The study focused on the effects of Reynolds number and cavity length-to-depth ratio by considering laminar and transitional flows. For laminar flow, it was found that the velocity along the straight line connecting the separation and reattachment locations gradually increase in the downstream direction. The ratio of local dividing streamline velocity to the outer-edge boundary-layer velocity approach 0.35 near the reattachment region for both laminar an transitional flows. In addition, the investigation pointed out that the gas temperature in the cavity increased toward the reattachment region, which is consistent with the heat transfer rate on the cavity wall. Also, the magnitude of the temperature increased with increasing Reynolds number and cavity length-to-depth ratio.

Nestler et al. (1969) conducted an experimental investigation on cavities and steps in a hypersonic turbulent flow. For the flow conditions investigated, they found that the pressure distributions in the cavity presented a typical behavior of closed cavity flow in the sense that the flow expands into the cavity, reattaches to the floor, and separates as it approaches at the downstream corner.

Unsteady hypersonic flow over cavities was investigated numerically by Morgenstern Jr. and Chokani (MORGENSTERN A.; CHOKANI, 1994). The objective of their study was to examine the effects of Reynolds number and the cavity length-to-depth (L/H) ratio. According to the authors, relatively large heat transfer rates and static pressure variations were observed in the rear part of the cavity. In addition, flow oscillations were observed for high Reynolds number flows. Results also showed that the amplitude of these oscillations increased with the cavity L/H ratio.

Jackson et al. (2001) conducted a combined experimental/computational study of an axisymmetric cavity in a low Reynolds number and Mach 9 flow. The cavity length-to-depth (L/H) ratio investigated covered the range from 1 to 8. For the shorter cavities a good agreement between experiment and laminar CFD was found on the front and back faces of the cavities. In the fore-body and after-body, it was observed a strong evidence for laminar flow. In the cavity floor, there was a disagreement between CFD and experiment results when flow unsteadiness was considered as the significant feature.

Everhart et al. (2006) investigated experimentally the effect of a pressure gradient on the local heating disturbance of rectangular cavities in a hypersonic flow conditions using a Mach 10 tunnel. This experimental study showed that for short (open) cavities, pressure gradient has a minimal effect on the average floor augmentation. In the other hand, for long (closed) cavities, pressure gradient increased the average heating by a factor of 50% above the zero gradient conditions, which was approximately 0.3. An assessment of the maximum increasing on the end wall revealed no apparent effect for the short cavity; however the analysis was inconclusive for the long cavity.

Based on the studies available in the open literature (EVERHART et al., 2006), the flow regimes over cavities can be generally classified as illustrated in Figure 1.4. According to this figure, the flow regimes through cavities are identified by the length-to-depth (L/H) ratio. As a result, four main cases can be defined as following:

- $L/H < 1$: short or deep cavities are defined as gaps. The main flow on the gap induces a column of counter-rotating vortices inside the gap. The number of vortices is approximately given by the H/L ratio.

- $1 < L/H < 10$: defined as open cavities. In this range, the flow conditions are stable. The mainstream flow does not enter in the cavity directly. The pressure in the cavity is typically above that of the environment and reaches a peak at the corner of the cavity front face.

- $10 < L/H < 14$: defined as transitional cavities. Cavities in this range are considered as unsteady, since the flow alternates between open and closed cavity. These cavities are avoided in experimental tests due to the complexity of instrumentation and test time necessary to observe the transient process.

- $L/H > 14$: defined as long cavity and denoted by closed cavities. The flow conditions are stable, similar to those in open cavities. In this configuration, three distinct types of flow can occur if the cavity is sufficiently long: (1) the upstream flow is able to penetrate in the cavity and to reach the bottom surface, similar to the flow on a backward-facing step, (2) the boundary layer on the bottom surface may develop and reach the outside, and (3) as the flow reaches the cavity frontal face, it turns outward in a similar way like the flow in a forward-facing step.

It should be mentioned in this context that the precise boundaries between open, transitional, and closed cavity flows depend on the freestream Mach number and on the cavity width-to-depth (W/H) ratio (PLENTOVICH et al., 1993). As matter of fact, different investigations have pointed out L/H ratio values ranging from 9 to 11 as the upper limit for open cavities, and from 12 to 15 as the lower limit for closed cavities.

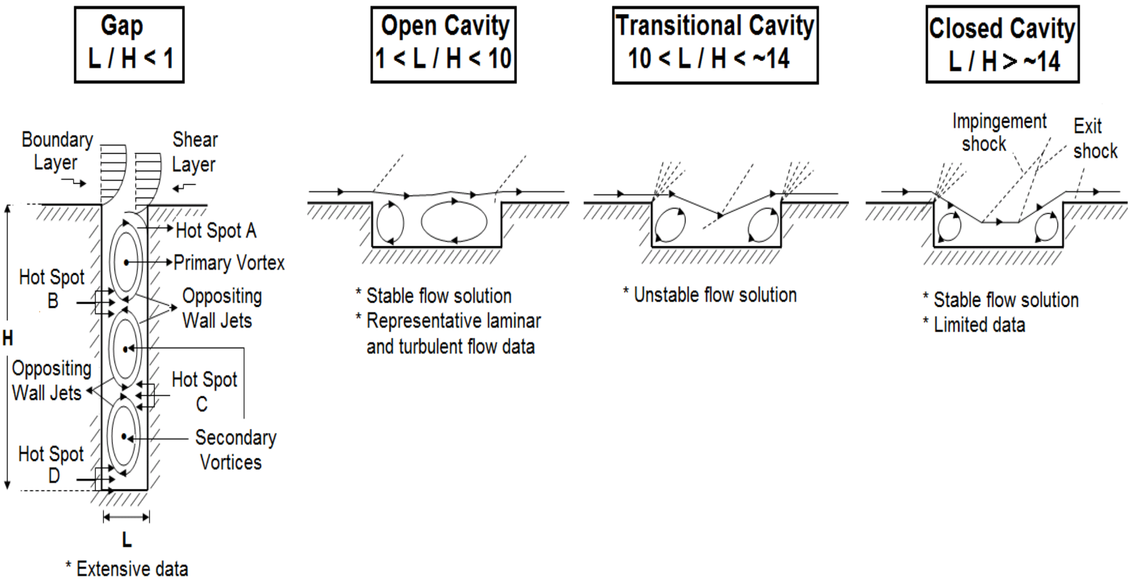
Gap
L / H < 1
Open Cavity
1 < L / H < 10
Transitional Cavity
10 < L / H < ~14
Closed Cavity
L / H > ~14
Boundary Layer
Shear Layer
Hot Spot A
Primary Vortex
Hot Spot B
Oppositing Wall Jets
H
Oppositing Wall Jets
Hot Spot C
Hot Spot D
Secondary Vortices
L
* Extensive data
* Stable flow solution
* Representative laminar and turbulent flow data
* Unstable flow solution
Impingement shock
Exit shock
* Stable flow solution
* Limited data

FIGURE 1.4 - Flowfield structure in cavities.

1.4 Present Work

The purpose of the research described in this dissertation is to investigate the impact of discontinuities or imperfections, often present on reentry vehicle surfaces, on the flowfield structure and on the aerodynamic surface quantities. In this work, the flowfield structure is defined by the distribution of the primary properties, such as velocity, density, pressure, and the kinetic temperature, adjacent to the vehicle surfaces. Aerodynamic surface quantities are identified by the heat flux, and the normal and tangential forces acting on the vehicle surface.

In the present study, discontinuities or imperfections are modeled by cavities situated in a hypersonic flow and a sufficiently high altitude where the appropriate mean free path becomes large for the use of continuum hypothesis but not large enough for applying free molecular concept. In order to assess the overall performance of these cavities, a parametric study related to the effects of the length-to-depth (L/H) ratio will be explored. In pursuit of this goal, two-dimensional hypersonic cavity flows will be investigated by employing the Direct Simulation Monte Carlo (DSMC) method.

The application of the DSMC method has been aimed primarily at the transition flow regime, which is characterized by Knudsen numbers that are above the upper limit for the validity of the Navier-Stokes equations but below the level at which the flow falls into the free molecular flow regime. In the transition flow regime, the aerodynamic heating and the forces acting on the vehicle surfaces are very sensitive to the degree of rarefaction. Therefore, attempts will be made to isolate the sensitivity of the thermal and pressure loads for different Knudsen numbers by changing the cavity L/H ratio.

The material in this dissertation is organized into five more chapters. In **Chapter 2**, a description of the appropriate computational method is presented. Particular emphasis is placed on the DSMC methodology, molecular model, collision model, internal degrees of freedom and boundary conditions. **Chapter 3** deals with the computational procedure. It includes the simulation conditions, the definition of the geometry analyzed in this research as well as the important geometric parameters. **Chapter 4** outlines the procedure for the verification and validation process of the DSMC code employed in the simulations. These procedures are applied in a test case defined by a flat-plate. The DSMC code is validated with simulation of a hypersonic flow over a flat-plate and comparisons with previous experimental and numerical results. Computational results and discussion are presented in **Chapter 5**. In this chapter, the major features of the primary properties, velocity, density, pressure and kinetic temperatures, are discussed in details. Moreover, the aerodynamic surface quantities, number flux to the surface, heat transfer, pressure, and shear stress, expressed in a coefficient form, are carefully examined. Finally, **Chapter 6** is devoted to the conclusion of this dissertation as well as a special section on future work.

2 COMPUTATIONAL METHOD

2.1 Methods for Flows in Transition Regime

The study of physical phenomena in hypersonic flows has been a challenging problem, directly related to the development of new aerospace technologies. The difficulties arising in the study of these flows are caused by problems related to high temperature gas effects, which have great influence on the forces present in the flows (pressure, shear stress), on the energy flux (radiative and convective heating), and on the mass flux (ablation). These problems become even more complex with decreasing the flow density.

The difficulty to find experimental devices for hypersonic flow of high enthalpy and low density, where several physical and chemical processes are relevant, has stimulated the development of various numerical methods to simulate these flows. As a result, nowadays there are many numerical methods which are accurate and capable of solving hypersonic problems in a rarefied environment. The choice of the appropriate method depends on the degree of flow rarefaction, the characteristic length of the problem and the presence of the real gas effects.

Flows are characterized by a variety of dimensionless quantities. For the purpose of this work, the Reynolds number, Re, the Mach number, M, and the Knudsen number, Kn, are the most important. The degree of rarefaction of a flow is usually expressed by the overall Knudsen number defined by Equation 1.1. Considering that the mean free path λ is inversely proportional to the density of the flow, then it should be seen that it is not the density alone that determines the degree of rarefaction, but the ratio of this property to the characteristic dimension of the problem. The continuum flow hypothesis is valid when the overall Knudsen number tends to zero. In this flow regime, one can disregard the microscopic structure and consider only the macroscopic properties such as density, velocity, pressure or temperature. In the opposite limit, when the Knudsen number tends to infinity, the flow regime corresponds to the free molecular flow. In this case, intermolecular collisions can not be ignored and the collisions of particles with the body surface become important. The region defined by $0.1 < Kn < 10$ is referred as the transition flow regime, where not only the gas-surface collisions but also the intermolecular collisions are important. In the transition flow regime, viscosity, heat conduction, chemical relaxation and diffusion processes are important. In this context, the velocity distribution function may deviate from the Maxwell distribution function, which results in a thermodynamic non-equilibrium gas flow.

The identification of a characteristic length l, defined in Equation 1.1, sometimes, is not immediate. In order to circumvent this problem, a local Knudsen number is used instead of the overall Knudsen number. The local Knudsen number is defined by the ratio of the local mean free path, λ, to a characteristic length defined by the gradient of any macroscopic property, hence,

$$l = \frac{\varphi}{|\nabla \varphi|} \tag{2.1}$$

which φ may be density, velocity, pressure or temperature.

The Figure 2.1 shows the range of applicability of conventional mathematical formulations as a function of the local Knudsen number.

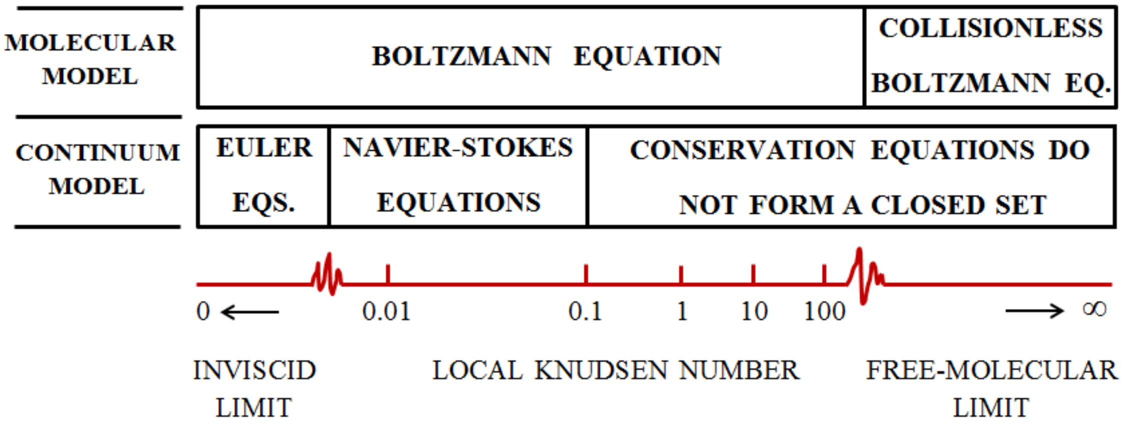
MOLECULAR MODEL
BOLTZMANN EQUATION
COLLISIONLESS BOLTZMANN EQ.
CONTINUUM MODEL
EULER EQS.
NAVIER-STOKES EQUATIONS
CONSERVATION EQUATIONS DO NOT FORM A CLOSED SET
0
0.01
0.1
1
10
100
∞
INVISCID LIMIT
LOCAL KNUDSEN NUMBER
FREE-MOLECULAR LIMIT

FIGURE 2.1 - Regimes of applicability of conventional mathematical models as a function of the local Knudsen number (adapted from (BIRD, 1994)).

In the macroscopic model or continuum model, the general expressions of the fundamental conservation principles that govern the motion of gases are valid for all flow regimes. However, these expressions do not form a system of equations in a closed form. The application of conservation equations requires additional information concerning the shear stress tensor and the heat flux vector expressed in terms of macroscopic quantities. The Euler equations for inviscid flow assume that the flow is in local thermodynamic equilibrium, with the velocity distribution function at any point in the flows equals to the Maxwellian distribution function. This is the limiting case as the Knudsen number tends to zero.

The continuum model, expressed by the Navier-Stokes equations, is assumed to be valid when the Knudsen number is very small in comparison with unit. In this case, the velocity distribution function deviates from the Maxwellian distribution function. However, this deviation is still small enough so that the transport coefficients, obtained from the Chapman-Enskog theory, are valid (CHAPMAN S.; COWLING, 1970). Usually, the term Navier-Stokes refers to the expressions that represent the conservation of linear momentum in viscous fluids. In practice, it is common to include the equations for conservation of mass and energy in this set of equations, known as the Navier-Stokes equations. The Navier-Stokes equations, as usually defined in fluid mechanics, can be applied to the study of Newtonian fluids, where the shear stress tensor is linearly proportional to the deformation rate tensor.

Boyd et al. (1995) have shown that the velocity distribution function differs significantly from the Maxwellian distribution function for a local Knudsen number $Kn > 0.05$, indicating that both the Chapman-Enskog theory and the Navier-Stokes equations are no longer valid. One alternative approach to this problem of the failure of the Navier-Stokes equations is to perform the Chapman-Enskog expansion to high order to obtain the Burnett equations (BURNETT, 1936). Each level of approximation implies a different distribution function that deviates from the Maxwellian distribution function. The interest in the Burnett equations, based on the second order expansion of the Chapman-Enskog for solving problems of rarefied hypersonic flows, has increased (COMEAUX et al., 1995; FISCKO K. A.; CHAPMAN, 1988; LEE, 1994; **??**; TANNEHILL J. C.; EISLER, 1976; ZHONG et al., 1993). However, the application of the Burnett equations has presented additional difficulties with the formulation of the boundary conditions and with instability of these equations for flows involving small disturbances (ZHONG et al., 1993). Moreover, the Burnett equations increase the order of the differential equations that govern the momentum and energy transport in the gas. These equations are harder to be solved numerically, and fail when the degree of rarefaction is sufficiently high. In addition, Burnett equations may not satisfy the second law of thermodynamics in certain situations, such as a negative dissipation function or the presence of a heat flux in an isothermal gas (COMEAUX et al., 1995). Finally, Cheng and Emmanuel (CHENG H. K.; EMMANUEL, 1995) present a detailed description of the use of Burnett equations to solve problems of rarefied hypersonic flow.

In the microscopic model or molecular model, the gas is treated as a collection of particles where the position and velocity of these particles are accompanied individually, such a system requires the solution of Boltzmann equation (CERCIGNANI C.; FREZZOTTI, 1989). Analytical solutions of the Boltzmann equation are possible for collisonless flow, i.e., when the Knudsen number tends to infinity. However, analytical difficulties are found for finite Knudsen number. The Boltzmann equation is an integral-differential equation with the velocity distribution function as the only dependent variable. In contrast, the Navier-Stokes equations have the flow velocity and thermodynamic properties as dependent variables. The reduction in the number of dependent variables in the Boltzmann equation is made at the expense of increasing the number of independent variables from the physical space to that of phase space. Thus, an one-dimensional monoatomic gas problem in a steady state becomes a three-dimensional in phase space.

Analytical solutions of the Boltzmann equation usually involve simple molecular models, one independent macroscopic variable and flows with small disturbances. However, rarefied hypersonic flow problems are associated with complex physical effects, such as chemical reactions and thermal radiation, which have not yet been incorporated into the Boltzmann formulation. Consequently, the mathematical difficulties associated with the direct solution of the Boltzmann equation have stimulated the development of physically-based numerical methods. The Boltzmann equation may be solved numerically by the following methods: Molecular Dynamics Method (MD) (ALDER B. J.; WAINWRIGHT, 1957; WAINWRIGHT, 1958), Test Particle Method (TP) (HAVILAND J. K.; LAVIN, 1962; ALDER; ROTENBERG, 1965), Direct Numerical Integration Method (DNI) and the Direct Simulation Monte Carlo (DSMC) method (BIRD, 1976; BIRD, 1994). By considering the purpose of this work, only the DSMC method will be presented and discussed.

2.2 Direct Simulation Monte Carlo (DSMC) Method

The DSMC method is a numerical simulation technique based on the particle dynamics (BIRD, 1976; BIRD, 1994). The DSMC method is based on physical concepts of rarefied gases and on the physical assumptions that form the basis for the derivation of the Boltzmann equation (CERCIGNANI, 1988). However, the DSMC method is not derived directly from the Boltzmann equation. As both, the DSMC method and the Boltzmann equation, are based on classical kinetic theory, then the DSMC method is subject to the same restrictions of the Boltzmann equation, i.e., the hypothesis of molecular chaos and the restriction of dilute gas.

Currently, the DSMC method has been recognized as a powerful technique capable of evaluating an almost unlimited variety of rarefied flows in the regimes where the Navier-Stokes equations and free-molecular flow (flow where collisions between particles are neglected when compared with those with the body) are not appropriate. The method has been tested in the transition flow regime in the last 50 years, and has produced excellent results when compared with experimental data (HARVEY, 1986; HARVEY J. K.; GALLIS, 2000; HARVEY J. K.; GALLIS, 2003; HOLDEN M. S.; WADHAMS, 2003).

Comparisons with experimental data have given credibility to the method, which has been vital in the receptivity of it. The advantages of the method that make it useful in engineering applications are:

(1) the comparative simplicity of changing 1-D problems into 2-D or 3-D ones;

(2) the possibility of incorporating complex models of gas-surface interaction, including the models of internal degrees of freedom and chemical reactions, without substantial complications in the computer program;

(3) it is well suited for use in parallel computing.

The DSMC method models the flow as a collection of particles or molecules. Each particle has a position, velocity and internal energy. The state of the particle is stored and modified with the time as the particles move, collide and interact with the surface in the simulated physical domain. The assumptions of dilute gas (where the mean molecular diameter is much smaller than the mean molecular space in the gas) allows for the molecular motion to be decoupled from the molecular collisions. The movement of molecules is modeled deterministically, while collisions are treated statistically. Since it is impossible to simulate the real number of molecules in the computational domain, a small number of representative molecules, referred as simulated particles or molecules, is used each representing a large number of real molecules. Simulations can vary from thousands to millions of molecules in rarefied flow problems.

A computational grid, representing the physical space to be investigated, is required for the method execution. The cell provides a convenient reference for the sampling of the macroscopic gas properties and for the choice of the potential collision pairs. The simulated molecules in the cell are considered as representative of the real molecules at the position of the cell, and the relative position of the molecules within the cell is ignored in the collision process of molecules.

The linear dimensions of the cells should be small in comparison with the scale length of the macroscopic flow gradients normal to the streamwise directions, which means that the cell dimensions should be the order of or smaller than the local mean free path, λ (BIRD, 1994; ALEXANDER et al., 1998; ALEXANDER et al., 2000).

An additional requirement of the DSMC method is related to the minimum number of simulated molecules in the cells. As mentioned earlier, the DSMC method uses the cell system for the sampling of the macroscopic properties and for the selection of collision partners. As the collision rate is a function of the number of molecules in the cells, it is desirable that each cell has the largest possible number of molecules. However, the possible number of collision partners is a function of the number of molecules in each cell. In this scenario, the greater the number of molecules, the greater the possible number of pairs to collide. As a result, for the collision process, it is desirable to have the number of molecules per cell as small as possible.

In order to solve this conflict, Bird (BIRD, 1987) introduced the option of subdividing the cells into an arbitrary number of sub-cells for the selection of collision pairs. This procedure improves the accuracy of the method by ensuring that collisions occur only between near neighbor molecules. Thus, it is desirable that each cell has a minimum number around 20 to 30 molecules (BIRD, 1994).

Another requirement of the DSMC method is a proper time step Δt. The trajectories of the molecules in physical space are accompanied considering the decoupling between the molecular motion and the intermolecular collisions. The time step should be chosen to be sufficiently small in comparison with the local mean collision time (GARCIA A. L.; WAGNER, 2000; HADJICONSTANTINOU, 2000). The simulation time can be identified as the real time, and the flow is always calculated as a unsteady flow. The steady state flow corresponds to the unsteady flow for large periods of time.

2.2.1 DSMC Methodology

The steps involved in the application of the DSMC method are illustrated in the flowchart shown in Figure 2.2. The DSMC algorithm can be conveniently divided in four individual steps: movement of the particles, indexing of particles, calculation of the collision and sampling of the particle properties.

The computational domain is initialized with the gas condition in thermodynamic equilibrium based on the freestream conditions in the physical space. Density, temperature, velocity and internal energy of molecules entering in the computational domain during each time step are specified by the known boundary conditions. The velocity of a simulated molecule is assumed as a linear combination of the thermal velocity and the freestream velocity. The boundary conditions corresponding to the desired flow are imposed at the time zero. The boundary conditions should be such that a steady flow is established at a sufficient large time, and the desired steady result is a time average of all values calculated after reaching the steady state.

After defining the position and velocity of each molecule, all molecules are moved through distances appropriate to their velocity components and the size of the time step. After the particle movement, its location in the computational domain is determined. This can be obtained in different ways. For cartesian grids, the new particle position is readily identified, and the destination cell is computed by using the indexing scheme defined by Bird (BIRD, 1994). For structured and unstructured grids, particle location schemes are outlined by Dietrich (DIETRICH, 1990), Laux (LAUX, 1997), and Usami and Nakayama (USAMI M.; NAKAYAMA, 2003), respectively. For more complex computational grids, such as hexahedral or tetrahedral, ray-trading techniques can be used to determine the particle position (NANCE et al., 1997; WILMOTH et al., 1996). Having defined the location of molecules, appropriate actions are taken for molecules crossing boundaries representing solid surfaces, lines or surfaces of symmetry or the outer boundary of flow.

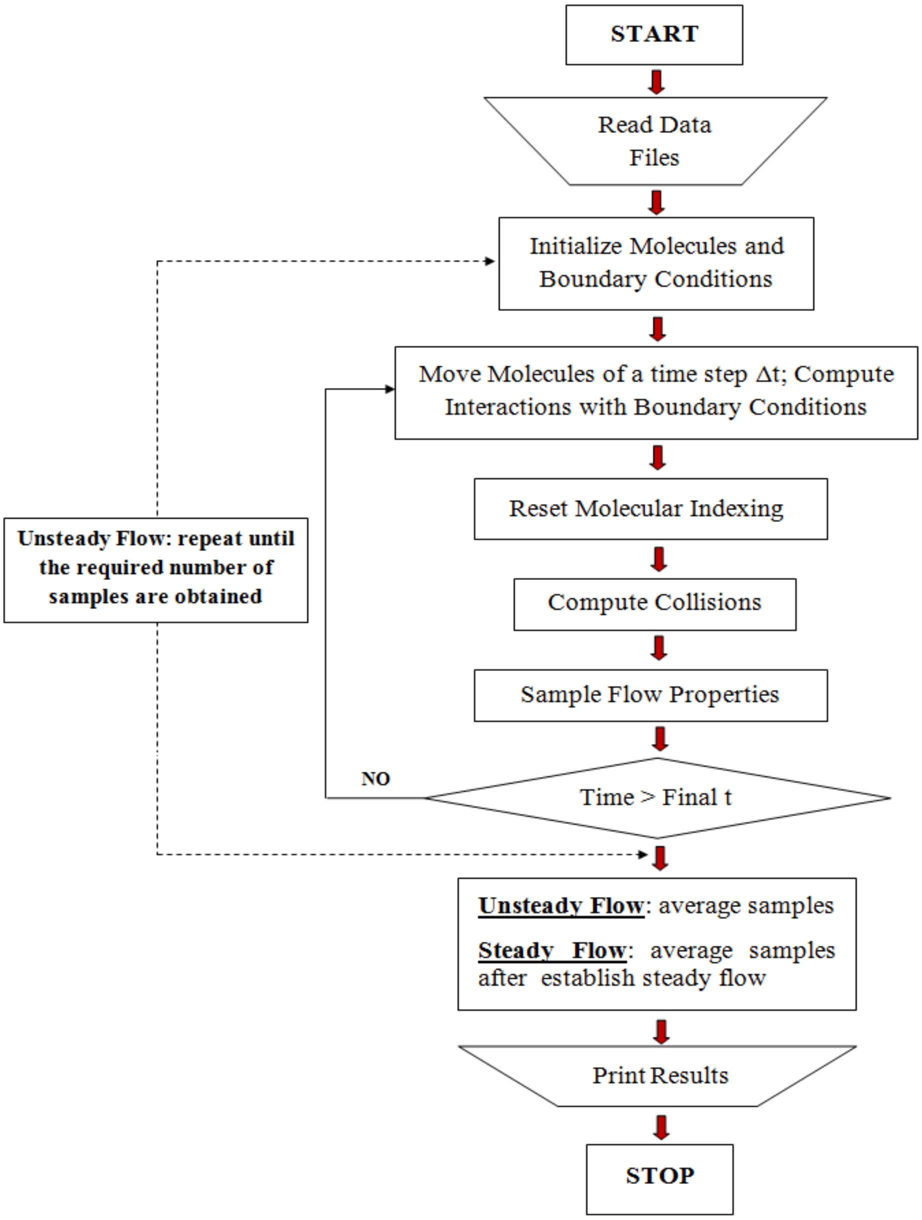
START
Read Data Files
Initialize Molecules and Boundary Conditions
Move Molecules of a time step Δt; Compute Interactions with Boundary Conditions
Reset Molecular Indexing
Compute Collisions
Sample Flow Properties
NO
Time > Final t
Unsteady Flow: repeat until the required number of samples are obtained
Unsteady Flow: average samples
Steady Flow: average samples after establish steady flow
Print Results
STOP

FIGURE 2.2 - Flowchart of the DSMC method.

Molecules leaving the computational domain are removed from the flow. New molecules are introduced into the simulation, at the outer boundaries of the computational domain with the freestream boundary conditions. Collisions with surfaces can be treated as specular, diffuse or a combination of these two types. The treatment of molecule-surface interaction requires the application of the conservation laws instead of using the velocity distribution function. Such application allow the DSMC method to be extended to include physical effects such as chemical reactions, catalytic walls, radiation effects, and ionized flows without major changes in the basic algorithm.

After determining the new location of the molecules, they should be indexed by cell location for the two subsequent steps: calculation of intermolecular collisions and sampling the flowfield. For the selection and calculation of intermolecular collisions, each cell is defined in a index system so that all other molecules in the cell can be reached through a cross-reference list. An efficient indexing scheme was introduced by Bird (BIRD, 1976) in the original DSMC algorithm.

In the next step, calculation of intermolecular collisions, molecular interactions are treated probabilistically instead of deterministically, as treated in the process of moving molecules. In doing so, several different collision modeling schemes have been formulated and applied in the DSMC method. Among them, one has the Time-Counter (TC) technique (BIRD, 1976), Nambu scheme (NAMBU, 1986), Null-Collision (NC) technique (KOURA K.; MATSUMOTO, 1991), No-Time-Counter (NTC) (BIRD, 1989), and the generalized scheme (ABE, 1993) of the NTC technique. The NTC scheme proposed by Bird (1989) is the preferred model currently used.

The collision procedure takes place in a cell-by-cell basis. Therefore, the time step, the cell volume and the number of molecules in the cell, are parameters that determine the number of possible pairs of candidate molecules in the collision process. The pairs of molecules are chosen randomly with the restriction that the mean separation between them be a fraction of the molecular mean free path. This restriction is imposed by selecting collision pairs from the list of molecules in the subcell. The DSMC method evaluates individual collision in a probabilistic basis, conserving momentum and energy.

Finally, the current description is completed by considering the sampling process of the macroscopic flow properties. These properties – density, velocity, temperature and pressure – are computed by appropriate average of the microscopic state of particles in each cell.

2.2.2 Molecular Model

The behavior of molecules during the collision process depends on the choice of the intermolecular force potential. A simple molecular model that is accurate enough for the majority of hypersonic calculations is the inverse power potential. The intermolecular force is modeled as the inverse of the repulsive power force as follows,

$$F_n = \frac{k}{r^{\eta}} \tag{2.2}$$

where r is the distance between the molecules involved in the collision and k and η are the molecular constants. The model proposed in Equation 2.2 corresponds to a Maxwellian gas for $\eta = 5$. The model of hard sphere (HS) is obtained by setting $\eta \rightarrow \infty$. In general, in engineering simulations, millions or billions of collisions are considered. Therefore, a simple interaction model should be considered. In this case, the simplest model is that corresponding to a hard sphere.

In the HS molecular model, the collision cross section is invariant for a single gas species. The scattering angle is isotropic, and the post-collision relative velocity is sampled to form a uniform solid angle distribution. However, the HS molecular model is not realistic, since the total collision cross-section σ_T does not depend on the relative velocity of the pair of molecules involved in the collision process. When the intermolecular potential law is given by Equation 2.2, the theory of Chapman-Enskog provides a direct relationship between the coefficient of viscosity and the gas temperature given by,

$$\mu \propto T^{\left(\frac{1}{2}+\frac{2}{\eta-1}\right)} \propto T^{S} \tag{2.3}$$

According to Equation 2.3, the coefficient of viscosity has a fixed temperature exponent. This exponent is 1 for the Maxwell model and 0.5 for the HS model. HS and Maxwell models are theoretical gases that can be considered as the limiting cases for the behavior of a real gas, since for almost real gases this exponent is generally in the range from 0.6 to 0.9.

Alternative molecular models, based on the HS model, have been proposed. These models have shown to be very successful at reproducing the macroscopic behavior of a gas yet remain computationally efficient. The first alternative model was defined as Variable Hard Sphere (VHS) introduced by Bird (BIRD, 1981). The VHS model treats molecules as "hard-spheres" with respect to the distribution of the scattering angle, i.e., all directions are equally possible for the post-collision velocity in a reference frame based on the center of mass. Moreover, the total cross-section σ_T varies with the relative speed of colliding molecules. The VHS model has been the most popular molecular model used in DSMC applications. It has been recommended for engineering calculations, since, for most flows of interest, it has been observed that the variation in the collision cross section has a far grater influence on the structure of a flow than any variation in the molecular scattering characteristics.

The VHS model has a molecular diameter (d) well defined and follows the same classical scattering law used in the HS model. This diameter is the inverse power law function of energy in the molecular collision, so,

$$\sigma \equiv \pi d^2 \propto \left(\frac{1}{2} m_r c_r^2 \right)^{-\omega} \tag{2.4}$$

where m_r is the reduced mass, c_r is the relative speed of colliding molecules and ω an exponent to be defined subsequently.

The collision cross section σ varies with temperature and collision relative speed c_r according to the following expression:

$$\sigma \propto c_r^{-4(\eta-1)} \propto T^{-2/(\eta-1)} \tag{2.5}$$

A comparison of Equations 2.4 and 2.5, shows that ω is related to the exponent of the inverse power law molecular force as follows:

$$\omega = \frac{2}{\eta - 1} \tag{2.6}$$

Therefore ω is equal to zero for the HS model, 1/4 for the inverse power law model, and 1/2 for the Maxwell model. The mean collision energy in an equilibrium gas at temperature T is:

$$\frac{1}{2}\,\overline{m_r c_r^2} = 2\left(\frac{\eta-2}{\eta-1}\right)\kappa T = (2-\omega)\kappa T \tag{2.7}$$

where κ is the Boltzmann constant. For a gas in thermodynamic equilibrium, the collision cross section is inversely proportional to the temperature to the power $-\omega$,

$$\sigma = \sigma_{ref}\left(\frac{T}{T_{ref}}\right)^{-\omega} \tag{2.8}$$

The reference value for the cross-section is based on a reference temperature T_{ref}. For a non-equilibrium gas the collision energy should be used, and Equation 2.4 may be written as:

$$\sigma = \sigma_{ref}\left(\frac{c_r^2}{c_{r_{ref}}^2}\right)^{-\omega} \tag{2.9}$$

The reference value of the square of relative collision speed can be chosen as the mean value of c_r^2 in an equilibrium gas at the reference temperature. The Equations 2.7 and 2.9 can them be combined as follows:

$$\sigma = \sigma_{ref}\left(\frac{m_r c_r^2}{2(2-\omega)kT_{ref}}\right)^{-\omega} \tag{2.10}$$

The DSMC code sets d_{ref}, T_{ref} and ω as constant, and Equation 2.10 is used to obtaining σ as a function of c_r. In the VHS model, the mean free path is given by,

$$\lambda = \frac{(T/T_{ref})}{(2-\omega)^{\omega}\Gamma(2-\omega)2^{(1/2)}n\sigma_{ref}} \tag{2.11}$$

As a result, the mean free path λ increases with temperature according to the same power law by which the cross section decreases.

In a real gas, the viscosity coefficient μ is given in terms of temperature by:

$$\mu \propto T^{\zeta} \tag{2.12}$$

where the exponent ζ usually varies from 0.6 to 0.9. For a gas in thermodynamic equilibrium, the mean cross section is given by:

$$\overline{\sigma} \propto T^{-\omega} \tag{2.13}$$

The viscosity coefficient, based on the Chapman-Enskog theory, is given by:

$$\mu = \frac{(15m/8)(\pi\kappa T)^{\frac{1}{2}}}{(2-\omega)^{\omega}\Gamma(4-\omega)\overline{\sigma}} \tag{2.14}$$

where m is the molecular mass and κ the Boltzmann constant. By comparing Equations 2.12, 2.13 and 2.14, one has,

$$\zeta = \frac{1}{2} + \omega \tag{2.15}$$

Therefore, by combining Equations 2.11 and 2.15, the mean free path is obtained as a function of the variable ζ,

$$\lambda = \frac{(2\mu/15)(7-2\zeta)(5-2\zeta)(2\pi\kappa T)^{(\frac{-1}{2})}}{\rho} \tag{2.16}$$

Koura and Matsumoto (KOURA K.; MATSUMOTO, 1991; KOURA K.; MATSUMOTO, 1992) further improved the VHS model and introduced the Variable Soft Sphere (VSS) molecular model. The VSS model considers the anisotropic post-collision scattering. The second free parameter introduced by the post-collision scattering dynamic in the VSS model is chosen in order to reproduce correctly the real viscosity and diffusion coefficients on the gases. Hassan and Hash (HASSAN H. A.; HASH, 1993) introduced the Generalized Hard Sphere (GHS) molecular model. The GHS molecular model takes into account both attractive and repulsive parts of the particle-particle interaction. In this model, molecules scatter like hard spheres, as was considered in the VHS model. Since the GHS model can reproduce the effects of attractive portion of an interaction potential, then the model is suitable to simulate low temperature flows that are dominated by attractive collisions (HASH et al., 1993; KUNC et al., 1995).

2.2.3 Collision Model

Several different collision-modeling schemes, which have been formulated and applied in the DSMC method, were previously presented in subsection 2.2.1. Among them, the TC technique (BIRD, 1976), the Nambu scheme (NAMBU, 1986), the NC technique (KOURA K.; MATSUMOTO, 1991), the NTC technique (BIRD, 1989) and the generalized scheme (ABE, 1993) of NTC technique. For the purpose of this study, only the CT technique and NTC will be described.

Procedures for the establishment of the correct collision rate are based on the cells, while the collision pairs are selected from subcells. The time step $\triangle t$, the volume of the cell V_c, and the number of molecules N resident in each cell will determine the possible number of collision pairs that will be evaluated. From the kinetic theory, it can be shown that the number of collisions must be simulated over a time step $\triangle t$, and it is given as follow:

$$N_{coll} = \frac{1}{2} N \triangle t n \overline{\sigma_T c_r} \tag{2.17}$$

where n is the number density.

In order to determine correctly the total number of collisions during the time step $\triangle t$, it would be necessary to calculate the average product of the mean relative speed c_r and the collision cross section σ_T for all possible pairs of molecules. An algorithm that uses this type of procedure would have a computational time proportional to N^2, where N is the total number of simulated molecules. In order to overcome this difficulty, Bird (BIRD, 1976) introduced the parameter $(\sigma_T c_r)_{max}$ where the subscript max denotes the largest value for the product in the cell, and it should be updated during a binary collision if the real product $\sigma_T c_r$ were greater than $(\sigma_T c_r)_{max}$. Furthermore, the parameter $(\sigma_T c_r)_{max}$ is used to determine a real collision according to the following operations:

(1) Two molecules are randomly selected in the cell. The probability that these molecules collide is given by:

$$P = \frac{\sigma_T c_r}{(\sigma_T c_r)_{max}} \tag{2.18}$$

if the probability P is greater than R_f, then the pair of molecules is accepted for the collision. R_f is a uniform random number ranging from 0 to 1. Otherwise, a new pair is randomly chosen and the procedure is repeated. This is the acceptance-rejection method described by Bird (BIRD, 1976) to select the collision pair of molecules.

(2) If the pair of molecules is accepted for the collision process, then a time counter for the current cell is advanced by the amount,

$$\delta t = \frac{2}{N \sigma_T c_r} \tag{2.19}$$

(3) A number of collisions is calculated in the cell until the sum of δt is slightly larger than the time step $\triangle t$. This is the TC scheme proposed by Bird (BIRD, 1976).

In the TC scheme, the total number of collisions within a time step $\triangle t$ depends on the product $(\sigma_T c_r)$ related to the collision pairs, which are randomly selected. Besides, it is not possible to calculate the total number of collisions at the beginning of the-time step interaction. Consequently, a complete vectorization of the collision process is not possible. This difficulty in TC scheme is due to the vector dependence associated with the implementation of summing several values of δt given by Equation 2.19 (BAGANOFF D.; MCDONALD, 1990).

In the NTC scheme, the time increment related to the chosen random pair of molecules is independent of the real product $(\sigma_T c_r)$. The parameter $(\sigma_T c_r)_{max}$ is fixed during a time increment $\triangle t$ and modified after performing all collisions. The idea of a time counter is replaced by the total number of collisions N_{coll} to be sampled in each cell by,

$$N_{coll} = \frac{1}{2}\frac{N\overline{N}F_N(\sigma_T c_r)_{max}\triangle t}{V_c} \tag{2.20}$$

where F_N is the number of real molecules represented by a single simulated molecule, N is the number of molecules inside the cell and $\overline{N}$ is a mean value. The collision probability for each chosen pair is given by Equation 2.18.

The NTC scheme was introduced to minimize difficulties found with the TC scheme in certain regions where the flow is not in thermodynamic equilibrium, for example, strong shock waves. The problem is related to the acceptance of an unlikely collision pairs with a relatively small collision probability (one with a very small value of $(\sigma_T c_r)$). Under such circumstances, the time increment given by Equation 2.19 may substantially exceed the time step $\triangle t$.

2.2.4 Binary Elastic Collisions

It was firmly established in the previous subsections that DSMC is based on the assumption of dilute gases. Usually, in the dilute gases, the intermolecular collisions are considered as being binary collisions. In addition, an elastic collision is defined as one in which there is no interchange of translational and internal energy.

The pre-collision velocities of two partners may be denoted by $\mathbf{c}_1$ and $\mathbf{c}_2$. By knowing the physical properties of the molecules and the orientation of their trajectories, the post-collision velocities $\mathbf{c}_1^*$ and $\mathbf{c}_2^*$ may be determined.

In order to determine the post-collision velocities, it is accepted that linear momentum and energy must be conserved in the collision. In this fashion, one has,

$$m_1\mathbf{c}_1 + m_2\mathbf{c}_2 = m_1\mathbf{c}_1^* + m_2\mathbf{c}_2^* = (m_1 + m_2)\mathbf{c}_m \tag{2.21}$$

$$m_1c_1^2 + m_2c_2^2 = m_1c_1^{*2} + m_2c_2^{*2} \tag{2.22}$$

where m_1 and m_2 are the masses of the two molecules, and $\mathbf{c}_m$ is the velocity of the center of mass of the two molecules. Equation 2.21 shows that the velocity of the center of mass does not change with the collision process. The pre- and post-collision values of the relative velocity between the molecules can be defined by:

$$\mathbf{c}_r = \mathbf{c}_1 - \mathbf{c}_2 \qquad \mathbf{c}_r^* = \mathbf{c}_1^* - \mathbf{c}_2^* \tag{2.23}$$

Equations 2.21 and 2.23 can be combined to provide the following expressions:

$$\mathbf{c}_1 = \mathbf{c}_m + \frac{m_2}{m_1 + m_2}\mathbf{c}_r \qquad \mathbf{c}_2 = \mathbf{c}_m - \frac{m_2}{m_1 + m_2}\mathbf{c_r} \tag{2.24}$$

Similarly, the post-collision components are defined by:

$$\mathbf{c}_1^* = \mathbf{c}_m + \frac{m_2}{m_1 + m_2}\mathbf{c}_r^* \qquad \mathbf{c}_2^* = \mathbf{c}_m - \frac{m_2}{m_1 + m_2}\mathbf{c}_r^* \tag{2.25}$$

In addition, the conservation of angular momentum requires that the projected distance between post-collision velocities be equal to the projected distance between the pre-collision velocities. Equations 2.24 and 2.25 show that,

$$\left.\begin{aligned} m_1 c_1^2 + m_2 c_2^2 &= (m_1 + m_2) c_m^2 + m_r c_r^2 \\ m_1 c_1^{*2} + m_2 c_2^{*2} &= (m_1 + m_2) c_m^2 + m_r c_r^{*2} \end{aligned}\right\} \tag{2.26}$$

where m_r, called the reduced mass, is given by,

$$m_r = \frac{m_1 m_2}{m_1 + m_2} \tag{2.27}$$

A comparison between the Equation 2.26 with the Equation 2.22 shows that the magnitude of the relative velocity does not change in the collision process, i.e.,

$$\mathbf{c}_r^* = \mathbf{c}_r \tag{2.28}$$

Since $\mathbf{c}_m$ and $\mathbf{c}_r$ can be calculated from the pre-collision velocities, the determination of post-collision velocities reduces the calculation of the changing direction of the relative velocity vector. If $\mathbf{F}$ is the force between two spherically symmetric point center of force molecules, and $\mathbf{r}_1$ and $\mathbf{r}_2$ are their positions vectors, then the equations of motion of the molecules are as following,

$$\left.\begin{aligned} m\ddot{\mathbf{r}}_1 &= \mathbf{F} \\ m\ddot{\mathbf{r}}_2 &= -\mathbf{F} \end{aligned}\right\} \tag{2.29}$$

By combining these two equations, one has,

$$m_1 m_2 (\ddot{\mathbf{r}}_1 - \ddot{\mathbf{r}}_2) = (m_1 + m_2)\mathbf{F} \tag{2.30}$$

If the relative velocity vector is denoted by $\dot{\mathbf{r}}$, then one obtains,

$$m_r \ddot{\mathbf{r}} = \mathbf{F} \tag{2.31}$$

Therefore, the motion of the molecule of mass m_1 relative to the molecule of mass m_2 is equivalent to the motion of the molecule of mass m_r relative to the fixed center of force.

For completeness, the results discussed above are summarized in Figure 2.3. Based in this figure, the transformation from the center of mass coordinate system changes the tree-dimensional trajectories into two-dimensional trajectories, which are symmetrical about the apse line AA'.

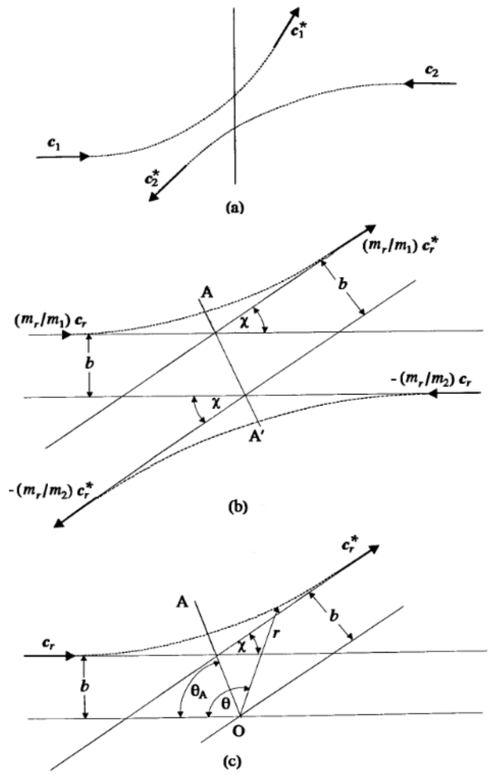

FIGURE 2.3 - Schematic drawing illustrating the analysis of binary collisions. (a) Planar representation of a collision in the laboratory frame of reference. (b) Binary collision in the center of mass frame of reference (c) Interaction of reduced mass particle with a fixed scattering center (Adapted from Bird (1994)).

The two trajectories are reduced to one in the further transformation to the reduced mass frame of reference, and this trajectory remains symmetrical about the transformed apse line which passes through the scattering center O. This symmetry reflects the symmetry of the equation with respect to the pre-collision and post-collision velocities.

2.2.5 Internal Degrees of Freedom

One of the most significant effects observed in a rarefied gas flow is the presence of a large degree of a non-equilibrium between the various internal energy modes of the gas. For polyatomic gases, the transfer of energy to and from the internal modes has to be considered. However, the energy transfer between the translational, rotational and vibrational degrees of freedom can not be computed accurately using a simple collision model.

The internal energy transfer between the various modes is usually implemented into the DSMC method by the phenomenological model introduced by Borgnakke and Larsen (BORGNAKKE C.; LARSEN, 1975). The main feature of this model is that a fraction ϕ of the translational collisions are assumed to be inelastic, and the rest of collisions $(1 - \phi)$ are considered as elastic. The fraction ϕ can be interpreted as the average probability of the energy exchange between rotational or vibrational modes for translational collisions.

This average probability can be determined from measurements of relaxation times. The relaxation time is a function of local flow properties and may be related to the relaxation number (or collision number) Z. The relaxation or collision number Z is usually defined by:

$$Z = \frac{\tau}{\tau_c} \tag{2.32}$$

where τ is the relaxation time and τ_c is the mean collision time. The relaxation or collision number is the average number of molecular collisions that are required for a particular mode to attain equilibrium energy. Therefore, given this number, the average probability ϕ for each mode in a given collision is conveniently defined as,

$$\phi = \frac{1}{Z} \tag{2.33}$$

Traditionally, DSMC calculations use the rotational collision number Z_R around 5. This means that, on average, a molecule rotationally relaxes once every five collisions. In general, this is a good approximation in engineering problems. However, more realistic models for rotational collision number as a function of the translational temperature or translational energy have been proposed (BOYD, 1990a; BOYD, 1990b; BOYD, 1990c).

Lumpkin (LUMPKIN et al., 1991) have noted that the mechanisms of energy transfer used in DSMC calculations affect energy transfer rate. According to them, the value of the collision number used in the DSMC should be approximately half of that determined experimentally and employed in a continuum computation. In this scenario, the following equation should be applied:

$$Z_R^{DSMC} = \frac{Z_R^{cont}}{\left(1 + \frac{\zeta_R}{\zeta_T}\right)} \tag{2.34}$$

where ζ_R and ζ_T are the degrees of freedom for rotational and translational energy, respectively.

The vibrational relaxation number Z_V is also computed as a function of the flow properties. The relaxation number can be easily determined if the collision frequency and the relaxation time are known in Equation 2.32. The relaxation time for vibrational mode is usually at least one order of magnitude greater than those associated with the translational and rotational modes. In DSMC applications, a vibrational relaxation number Z_V on the order of 50 has been employed. This means that, on average, vibrational relaxation occurs for one in every fifty collisions. The Borgnakke-Larsen method can be applied to the vibrational modes by using either a classical or quantum procedure. In the classic procedure, the vibrational energy is treated as a continuous distribution described by the number of vibrational degrees of freedom ζ_V in which is fixed. In the quantum procedure, the discrete nature of the vibrational spectrum is taken into account, since the vibrational spectrum of real molecules is characterized by large gaps between the neighboring energy levels. The quantum procedure allows the sampling post-collision vibrational energy levels from the discrete form of the Simple Harmonic Oscillator (SHO) model. This procedure does not require that the value ζ_V be estimated for the entire flowfield. Instead, ζ_V varies with the local energy contained in the flow. Both procedures – classical and quantum – are discussed in detail by Bird (BIRD, 1994). The number of vibrational relaxation as a function of collision energy is presented by Bergemann and Boyd (BOYD, 1990a; BOYD, 1991; BERGEMANN F.; BOYD, 1994), and as a function of temperature by Hassan and Hash (**??**).

2.2.6 Boundary Conditions

In the gas dynamics problems there are two basic types of boundary conditions: those specified by the freestream quantities and those at a solid surface, where the molecules interact or reflect directly.

The first condition is easily represented by an equilibrium gas moving with a prescribed velocity. The molecular velocity distribution can be given as Maxwellian with an imposed velocity. This distribution is valid for any ideal gas, regardless of the type of forces between the molecules. The second condition depends on the treatment of the gas-surface interaction. The influence of the gas-surface interaction model in the aerodynamic forces and heat transfer increases significantly as the gas rarefaction increases. Therefore, the correct choice of the model for calculating rarefied hypersonic flows plays an important role.

Three models of gas-surface interaction can be employed in the DSMC method: specular, diffuse or a combination of these methods. In a specular reflection, molecules are reflected as an elastic sphere with reversal of the normal component of the velocity and without any changes in the tangential components of velocities and energy. In a diffuse reflection, molecules are reflected equally in all directions with a complete thermal accommodation. The velocity components of the reflected molecules are independent of their incident velocity and direction.

The combination of diffuse reflection with specular reflection (Maxwell model) introduces a single parameter f to indicate the fraction of those molecules reflected diffusely in a complete accommodation fashion according to a Maxwellian distribution corresponding to the wall temperature. The remaining fraction $(1 - f)$ is assumed to reflect specularly.

The Maxwell model was followed by the introduction of three accommodation coefficients that describe the degree of accommodation of the incident normal momentum, tangential momentum and kinetic energy to those of surface. A variety of definitions for coefficients of accommodation exists in the literature. The traditional definition is usually expressed as,

$$\alpha_n = \frac{p_i - p_r}{p_i - p_w} \tag{2.35}$$

$$\sigma_t = \frac{\tau_i - \tau_r}{\tau_i} \tag{2.36}$$

$$\alpha_r = \frac{e_i - e_r}{e_i - e_w} \tag{2.37}$$

where e_i, τ_i and p_i, are flux of energy, tangential and normal momentum, respectively, incident on the surface, e_r, τ_r and p_r, are the fluxes of these quantities reflected from the surfaces, and e_w and p_w $(\tau_w = 0)$, are the flux that would be reflected by a gas in a complete Maxwellian equilibrium with the surface. The model of Maxwell reflection is showed in Figure 2.4.

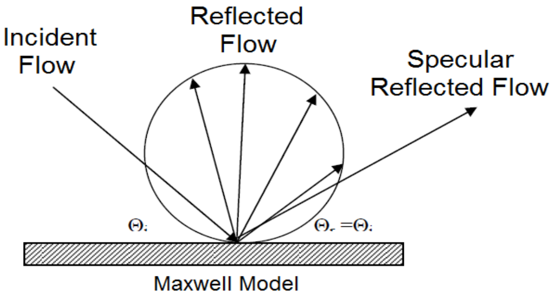

FIGURE 2.4 - Maxwell model of reflection.

3 COMPUTATIONAL PROCEDURE

3.1 Geometry Definition

In the present account, discontinuities, imperfections or distortions, present on reentry vehicle surfaces, will be modeled by cavities. By considering that the cavity length L is usually of the order of 3 to 9 mm (EVERHART et al., 2006; GAI S.; MILTHORPE, 1995; GROTOWSKY I. M. G.; BALLMANN, 2000; HOZUMI et al., 2004; HINDERSKS M.; RADESPIEL, 2006; JACKSON et al., 2001) and that the curvature radius R of a reentry vehicle nose, such as that one shown in Figure 1.1, is about two orders of magnitude larger than these values, then $L/R << 1$ or $H/R << 1$. In this scenario, the flow over the cavity can be modeled by considering the flow over a flat plate with a cavity positioned far from the stagnation point of the vehicle nose.

A schematic drawing of the cavity and the main parameters related to the hypersonic flow are illustrated in Figure 3.1. According to Figure 3.1, M_∞ represents the freestream Mach number, α the angle of attack, H the cavity depth, L the cavity length, L_u and L_d the cavity upstream and downstream lengths, respectively. In this context, for the family of cavities investigated in this work, H was fixed in 3 mm, while L assumed values of 3, 6, 9 and 12 mm. These values correspond to a height of $3.23\lambda_\infty$ and length L of $3.23\lambda_\infty$, $6.46\lambda_\infty$, $9.69\lambda_\infty$ and $12.92\lambda_\infty$, where λ_∞ is the freestream mean free path. Therefore, the cavities investigated correspond to L/H ratio of 1, 2, 3 and 4, respectively. Moreover, it was assumed L_u and L_d of $50\lambda_\infty$.

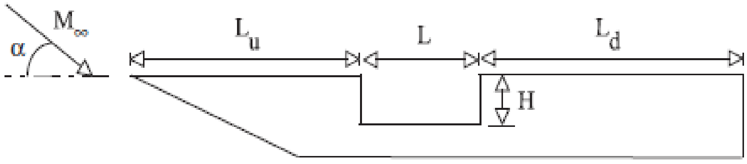

FIGURE 3.1 - Drawing illustrating the cavity.

In order to understand the L/H ratio effect on the flowfield structure and on the aerodynamic properties, it becomes necessary to investigate the flowfield structure behavior on a flat plate without discontinuities, i.e., without cavities. Therefore, the solution for a flat plate without cavities, defined herein by a flat plate case, will be used as a benchmark for cases with a cavity.

3.2 Computational Conditions

The governing equation in the transition flow regime is the Boltzmann equation. The Bolzmann equation is a nonlinear integral-differential equation, closed with respect to the one-particle distribution function, which in turn determines the density of particles in a six-dimensional phase space of particle coordinates and velocities. A detailed treatment of the Boltzmann equation can be obtained by Cercignani (CERCIGNANI C.; FREZZOTTI, 1989).

As discussed in chapter 2, in order to overcome the difficulties of solving directly the Boltzmann equation, the DSMC method has been considered as one of the main alternative methods to solve the Boltzmann equation by simulating the behavior of individual particles. It has been considered as the appropriate choice for problems involving complex flows of rarefied hypersonic aerothermodynamics.

The DSMC code used in this study was developed based on the same physical concepts as described by Bird (BIRD, 1994). In this work, the molecular collisions are modeled using the Variable Hard Sphere (VHS) model and the No-Time-Counter (NTC) method as a collision sample technique, as described in the chapter 2. The energy exchange between kinetic and internal modes is controlled by the Borgnakke-Larsen phenomenological model (BORGNAKKE C.; LARSEN, 1975). Simulations are performed for air as a working fluid with two chemical species, N_2 and O_2. Chemical reactions due dissociation and recombination process were not considered.

The probability of an inelastic collision determines the rate at which energy is transferred between translational and internal modes after an inelastic collision. For a given collision, this probability is defined by the inverse of the relaxation number, which corresponds to the number of collisions necessary, on average, for a molecule to undergo relaxation. The relaxation numbers are assumed to be constant, $Z_R = 5$ for rotational and $Z_V = 50$ for vibrational. The procedure for vibrational energy exchange is also computed by the Borgnakke-Larsen approach with the post-collision vibrational energy levels sampled from the discrete form of the Simple Harmonic Oscillator (SHO) (BIRD, 1994).

The rotational and vibrational relaxation models used in this simulation are adjusted to match continuum values by the correction presented in Equation 2.32.

The freestream coefficient of viscosity μ_∞ and the freestream mean free path λ_∞ are evaluated from consistent definitions (BIRD, 1983). Table 3.1 tabulates the air characteristics employed in the DSMC calculations.

TABLE 3.1 - Characteristics of simulated air for DSMC calculations.

Property	Value	Unit
Working fluid	$N_2 + O_2$	
Molecular weight	28.96	kg/kgmole
Molecular mass O_2	5.312x10^{-26}	kg
Molecular mass N_2	4.650x10^{-26}	kg
Molecular diameter O_2	4.010x10^{-10}	m
Molecular diameter N_2	4.110x10^{-10}	m
Mole fraction O_2	0.237	
Mole fraction N_2	0.763	
Viscosity index O_2	0.77	
Viscosity index N_2	0.74	
Degree of freedom O_2	5 to 7	
Degree of freedom N_2	5 to 7	

The computational domain used for the calculations is large enough so that body disturbances do not reach the upstream and side boundaries, where freestream conditions are specified. The flowfield is divided into an arbitrary number of regions. Each region has a value for the time step $\triangle t$ and a scale factor F_N, which defines the ratio of the number of real molecules to the number of simulated molecules. A schematic drawing of the computational domain is illustrated in Figure 3.2.

According to Figure 3.2, the side $I-A$ represents the cavity surface. Diffuse reflection with complete thermal accommodation is the boundary condition applied to this side. This condition is directly applied to individual molecules interacting with the cavity surface. Side $I-B$ represents a surface where all flow gradients normal to this surface is zero. At the molecular level, this boundary condition is equivalent to a specular reflecting boundary, where the normal component of the incident velocity is reversed, while the parallel component is left unchanged. Sides II and III are boundaries with a specified uniform freestream flow. A set of molecules crossing the boundary into computational domain is generated at these sides. Molecules crossing these sides from the computational domain are removed from the flow. These sides correspond to the correct physical representation of the correct freestream flow as long as the disturbances of the flow, due the presence of the body, do not reach such boundaries. Finally, the side IV is a boundary defined by vacuum or by a group of molecules leaving or entering into the computational domain. The option for vacuum is suitable for an outflowing gas with a high supersonic velocity component across such a boundary, since there are virtually no upstream moving molecules in a flow with Mach number greater than about three (BIRD, 1994). Hence, vacuum is the prescribed boundary condition for this side. The upstream extent of the interference due to this unrealistic boundary condition is determined by increasing the body length.

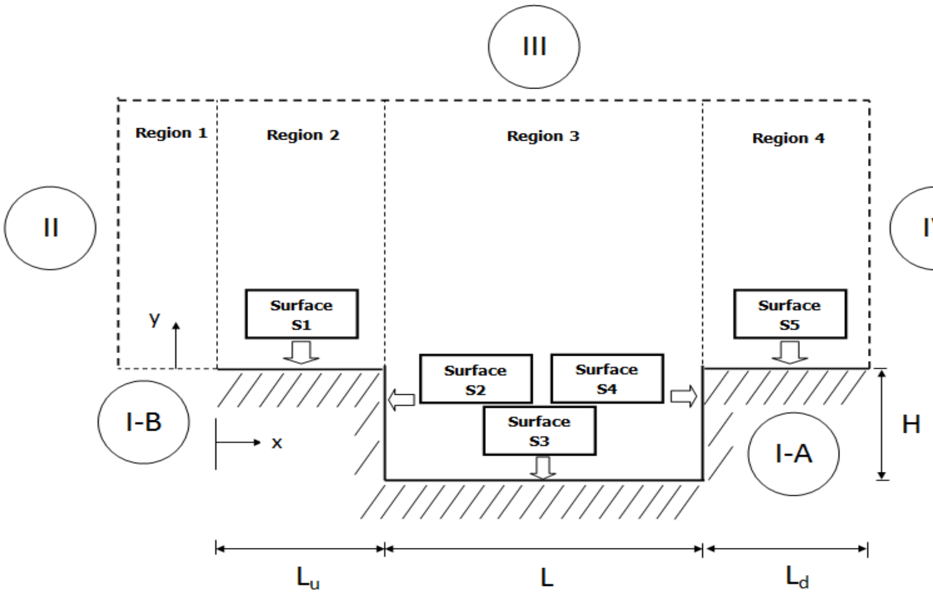

FIGURE 3.2 - Drawing illustrating the computational domain.

The mesh generation scheme, the effect of the mesh resolution, and the complete verification and validation process employed in this study are described in the next chapter.

3.3 Freestream and Flow Conditions

Based on Figure 3.1, the main physical and geometric parameters can be identified by the freestream Mach number M_∞, the angle of attack α, the height H, the width L and the L_u and L_d cavity lengths. Also, the surface temperature T_w and the gas-surface interaction should be added. In this scenario, the flowfield structure on the cavity can be changed due to the effects of compressibility, rarefaction, gas-surface interaction, the surface temperature, the L/H ratio, etc.

The present work focuses on the influence of the cavity L/H ratio on the flowfield structure. Effects of the L/H ratio are investigated for L/H of 1, 2, 3 and 4. The flow conditions represent those experienced by the SARA (acronyms for SAtélite Recuperável Atmosférico) capsule at 70 km of altitude. This capsule has been developed by IAE (Instituto de Aeronáutica e Espaço) at DCTA (Departamento de Ciência e Tecnologia Aeroespacial).

Freestream flow conditions used for the numerical simulations are tabulated in Table 3.2. The freestream velocity U_∞ is assumed to be constant at 7456 m/s, which corresponds to a freestream Mach number M_∞ of 25. The surface temperature T_w is assumed constant at 880 K. This temperature is chosen to be representative of the surface temperature near the stagnation point of the SARA capsule. Machado and Boas (MACHADO et al., 2006) showed that the temperature at the stagnation point of the SARA capsule may reach a maximum value of 950 K for the conditions investigated. In addition, it is considered that the flow is aligned to the cavity, i.e., zero degree angle of incidence.

By assuming the cavity length L as the characteristic length, then the Knudsen number K_{nL}, defined by Equation 1.1, corresponds to 0.3095, 0.1548, 0.1032, and 0.0774 for the length L of 3, 6, 9 and 12 mm, respectively. Finally, the Reynolds number Re_L is around 121.7, 243.4, 365.1, and 486.8 for the length L of 3, 6, 9, and 12 mm, respectively.

TABLE 3.2 - Freestream flow conditions.

Property	Value	Unit (SI)
Velocity (U_∞)	7456	m/s
Temperature (T_∞)	219.69	K
Pressure (p_∞)	5.582	N/m^2
Density (ρ_∞)	8.753x10^{-5}	kg/m^3
Number Density (n_∞)	1.819x10^{21}	m^{-3}
Viscosity (μ_∞)	1.455x10^{-5}	Ns/m^2
Mean free path (λ_∞)	9.285x10^{-4}	m^{-3}

4 VERIFICATION AND VALIDATION

Before proceeding with the computational results, it is imperative to present the verification and validation processes employed in this DSMC code. Verification and validation processes should establish the trust in the computer code that it is suitable for the intended use. The DSMC verification and validation processes consist of three basic steps: (1) verify the appropriate number of cells, (2) verify the appropriate number of molecules, and (3) compare DSMC results with analytic or experimental results available in the open literature. In this context, the purpose of this chapter is to discuss at length these three steps.

4.1 Computer Requirements

The DSMC method has been developed to deal with complex flow phenomena in the transition flow regime. For this method, a computational mesh has to be constructed to form a reference for selecting collision partners and for sampling and averaging macroscopic flowfield properties.

Many practical problems involve complex body shapes, and the generation of a suitable mesh for this problems can be very demanding and time consuming task. Numerous efforts to develop alternative meshes and reduce the computational cost of the method have resulted in several different forms of mesh generation: structured, unstructured, block by zone, cartesian, among others. Among the important contributions are the body-fitted coordinate system implemented by Abe (ABE, 1989), the transfinite interpolation method by Olynick et al. (OLYNICK et al., 1989), and multi-level cartesian mesh proposed by Rault (RAULT, 1994).

In general, three basic types define the schemes for mesh generation: (1) a uniform cartesian mesh, (2) a structured-body-fitted mesh, and (3) an unstructured-body-fitted mesh. Each of these schemes has advantages and disadvantages such as less expensive movement phase, grid clustering in regions of large flow gradients, and application in the simulation of complex geometries. The merits of each scheme in terms of accuracy, computational efficiency and overall ease of use are compared and discussed in detail by Wilmoth et al. (WILMOTH et al., 1996) and Nance et al. (NANCE et al., 1997).

Three primary constrains must be considered in the DSMC method when evaluating computational requirements: (1) the time step must be less than the local mean collision time, (2) the cell size should be smaller than the local mean free path, and (3) the number of particles per cell should be roughly constant in order to preserve the statistics in the collision process. The most important assumption assumed in the DSMC method is that the gas is dilute, i.e., the mean molecular diameter is much smaller than the mean molecular spacing of molecules in the gas. This assumption allows the molecular motion to be decoupled from the molecular collisions of a small local time interval. Thus, the successful application of the method requires the magnitude of the time step to be a small fraction of the mean collision time, and the cell size of the order of a third of the local mean free path.

In order to accurately model collisions by using a statistical approach, the cell size should be on the order of one third or smaller than the local mean free path in the direction of primary gradients (BIRD, 1994). Near to the body surface, the cell size in the normal direction to the surface should also be the order of or smaller than one third of the local mean free path. This is because in certain regions, such as the vicinity of adiabatic surfaces, flowfield gradients must be very small, and the cell size must be small enough to adequately capture flowfield physics near the wall. If the cell dimensions near the body surface are too large, then energetic molecules at the far edge of the cell could transfer energy and momentum to molecules located immediately adjacent to the body surface. The latter molecules may, in turn, transmit this energy and momentum to the surface. This behavior would lead to a over-prediction of the heat flux and of the aerodynamic loads acting on the surface. This type of error can be minimized by reducing the cell size relative to the local mean free path of molecules near the surface. Within the flowfield, the grid points should be close to each other in regions where the physical properties vary rapidly. The cell size should be small in regions where density is large in order to limit not only the number of particles in each cell but also the number of collisions in a given time step.

In order to adequately model the physical processes of interest, the simulation must be performed with a minimum number of molecules in each cell. To obtain accurate collision statistics, it is desirable to have 20 to 30 molecules in each cell. However, the maintenance of this requirement becomes difficult when the distribution of density in the computational domain is no longer uniform. As pointed out by Kannenberg and Boyd (KANNENBERG K. C.; BOYD, 2000), the number of molecules in the cell varies inversely with the density. Thus, high-density regions will tend to have few particles while low-density regions will have a large number of particles resulting in over resolution in the flow domain. In order to overcome this difficulty, i.e., large variations in the number of molecules in cells throughout the computational domain, a variable scaling factor F_N is used with the purpose of controlling the distribution of simulated molecules within cells. F_N represents the ratio of the number of real molecules and the number of simulated molecules.

In this context, the computational effort is substantially reduced by dividing the flowfield into an arbitrary number of regions where the time step $\triangle t$ and the scaling factor F_N remains constant with a region, but can vary from region to region within the computational domain. The combination of dividing the computational domain into regions along with the use of variable cell sizes leads to a substantial reduction in the total number of simulated molecules and a better resolution of the mesh in regions where the gradients are more intense. As a result of this combination, the computational time is substantially reduced. It is important to mention that although the time step $\triangle t$ and the scaling factor F_N can vary from region to region, $F_N/\triangle t$ ratio must be the same for all regions in order to conserve mass flux across region boundaries in the flow.

Finally, details of the requirements for the DSMC method are described, among others, by Rieffel (RIEFFEL, 1999) and Shu and Mao (SHU et al., 2005).

4.2 Computational Mesh

In this work, the mesh generation scheme was based on the procedure presented by Bird (BIRD, 1999) in the DSMC algorithm called DS2G. Basically, the flowfield is divided into an arbitrary number of regions. Each region defined by four sides. Two opposite sides can be curved or straight (e.g., sides I and III in Figure 3.2) and the other two are straight (sides II and IV in Figure 3.2). Along the boundaries, point distributions are generated in such way that the number of points on each side is the same. Next, the cell structure is defined by connecting the corresponding points on each side by straight lines, and them dividing each of these lines segments which are joined to form the system of quadrilateral cells. The distribution of these points can be controlled by different algebraic functions that allow the concentration of points in certain regions where the gradients are more intense or regions where small mean free paths are expected. The distribution of points may be chosen independently for each region.

4.3 Adaptation of the Computational Mesh

The procedure used for the computational mesh adaptation is divided into three steps: (1) a computational mesh is initially generated based on freestream conditions, (2) values for the scaling factor F_N are defined for each region, and the time step $\triangle t$ is estimated subjected to the condition that the ratio $F_N/\triangle t$ is the same for all regions, (3) these parameters are iteratively modified until an acceptance number of simulated molecules, cell size distributions and simulation time step are obtained.

4.4 DSMC Test Case

The problem of a rarefied hypersonic flow over a flat plate without cavity was chosen to validate the two-dimensional version of the DSMC code used in this work. Due to the geometric simplicity, the flat plate has been considered as one of the most useful test cases for verification and validation of the DSMC method through comparisons with experiments. The flat-plate model has been selected because both experimental data (BECKER et al., 1974) and previous numerical simulations (CERCIGNANI C.; FREZZOTTI, 1989; HERMINA, 1989; HURLBULT, 1989b; LORD, 1994) are available in the open literature for comparison. Therefore, a flat plate with characteristics of that investigated by Becker et al. (BECKER et al., 1974) was adopted in this work as a test case.

According to Becker et al. (BECKER et al., 1974), a flat plate of 50.8 mm of length, 25.4 mm of width and leading edge thickness of 0.04 mm was positioned along the centerline of a Helium jet gas. The Helium flowfield was generated by the freejet expansion from a distance of the flat plate resulting in a freestream Mach number of 8.9, temperature of 10.7 K and pressure of 0.3379 N/m^2. The flat-plate surface temperature T_w was 290 K.

Table 4.1 presents the freestream main properties. Based on these properties, the freestream Knudsen number Kn_∞ is 0.0253 and the Reynolds number Re_∞ is 71.3, by considering the flat-plate length as the characteristic length.

In the computational solution, it was assumed that the flat plate is immersed in a uniform stream flowing parallel to the plate itself. The flat plate was modeled as one with zero thickness and length of $102,8$ mm, which corresponds to $80\lambda_\infty$.

The undisturbed freestream boundary condition was imposed at a distance of $5\lambda_\infty$

TABLE 4.1 - Freestream main properties.

Property	Value	Unit (SI)
Velocity (U_∞)	1723	m/s
Temperature (T_∞)	10.7	K
Pressure (p_∞)	0.3379	N/m^2
Density (ρ_∞)	1.520x10^{-5}	kg/m^3
Number density (n_∞)	2.285x10^{21}	m^{-3}
Viscosity (μ_∞)	1.865x10^{-5}	Ns/m^2
Mean free path (λ_∞)	1.286x10^{-3}	m

upstream of the flat-plate leading edge. The computational domain normal to the flat-plate surface covers a distance of $30\lambda_\infty$ above the flat plate.

The computational domain used for the calculation is made large enough so that flat-plate disturbances do not reach the upstream and side boundaries, where freestream conditions are specified. A schematic view of the computational domain is illustrated in Figure 4.1. According to this figure, the computational domain is divided into two regions, which are subdivided into computational cells. Region 1 consists of 10 cells along side $I-B$ and 40 cells along side II. Region 2 consists of 300 cells distributed along side $I-A$ and 80 cells normal to the plate surface, i.e., along side IV. This computational mesh was defined as the standard case. In addition to this mesh, two others meshes, defined as coarse and fine, where used to study the sensitivity of the computations to mesh resolution.

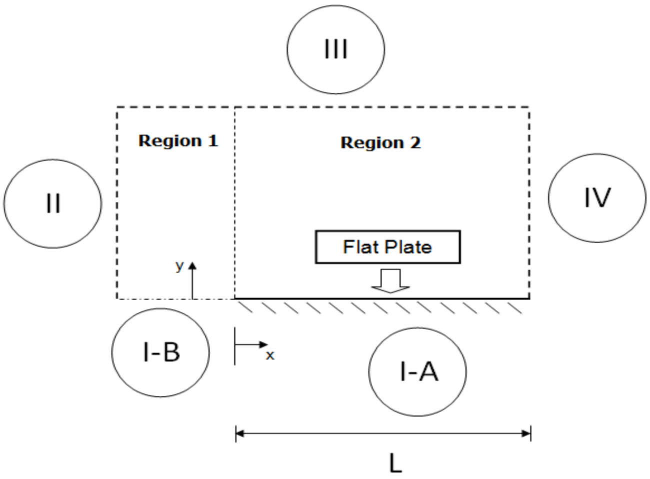

FIGURE 4.1 - Drawing illustrating the flat-plate computational domain.

4.4.1 Effect of Mesh Resolution

The effect of the mesh resolution on the computational results is of particular interest in the present study since insufficient grid resolution can reduce significantly the accuracy of predicted aerodynamic surface quantities. Hence, heat transfer, pressure and skin friction coefficients are used as the representative parameters for the mesh sensitivity study.

The effect of the altering the mesh resolution in the x- and y-directions was investigated for a coarse and fine grids with, respectively, 50% less and 100% more cells with respect to the standard grid. Table 4.2 tabulates the number of cells employed in the two regions for coarse, standard and fine meshes. In addition, each grid was made up of non-uniform cell spacing in both directions.

TABLE 4.2 - Number of cells in the (x-direction) and [y-direction] for the flat-plate case.

	Region 1	**Region 2**	**Cells**
Coarse	(5×40)	(150×80)	$12,200$
	[10×20]	[300×40]	$12,200$
Standard	10×40	300×80	$24,400$
Fine	(20×40)	(600×80)	$48,800$
	[10×80]	[300×160]	$48,800$

The effect of changing the number of cells in the x-direction is illustrated in Figure 4.2 as it impacts the calculated skin friction C_f, pressure C_p and heat transfer C_h coefficients. In this set of plots, X represents the distance x normalized by the freestream mean free path λ_∞. According to Figure 4.2, the comparison shows that the calculations results are insensitive to the range of cell spacing considered for the x-direction.

A similar examination was made in the y-coordinate direction. A new series of three independent simulations were made considering a coarse, standard and fine meshes. The influence of the cells size in the skin friction, pressure and heat transfer coefficients is demonstrated in the Figure 4.3. According to this group of plots, the results for the three independent meshes are approximately the same, indicating that the results for the standard mesh is essentially grid independent.

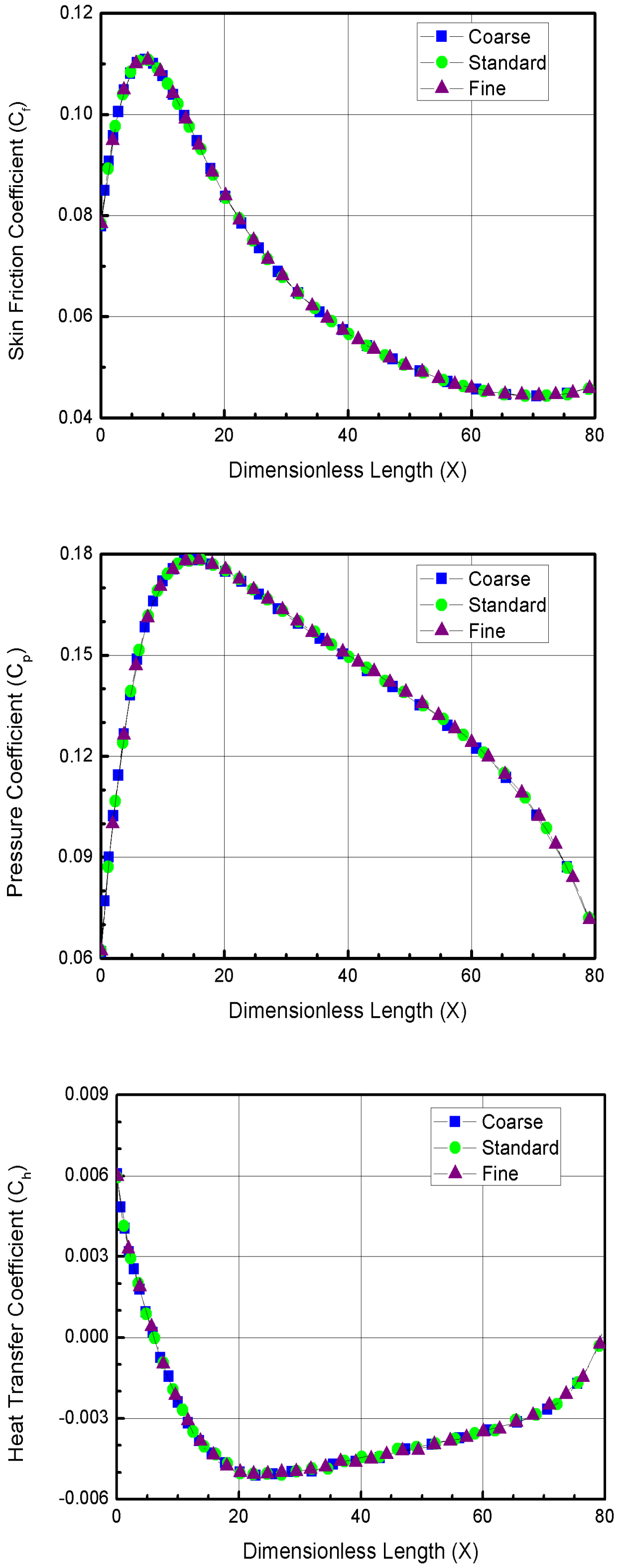

FIGURE 4.2 - Effect of changing the cell size (x-coordinate direction) on skin friction (top), pressure (middle), and heat transfer (bottom) coefficients.

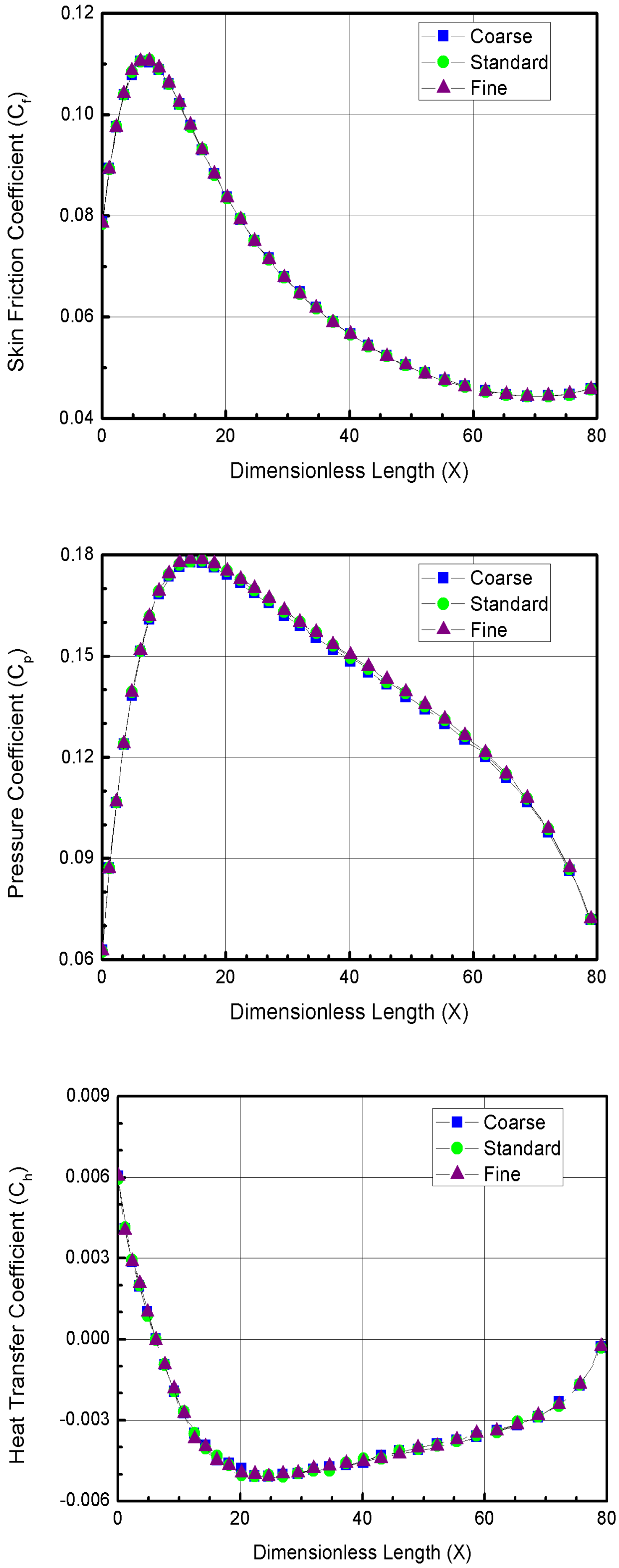

FIGURE 4.3 - Effect of changing the cell size (y-coordinate direction) on skin friction (top), pressure (middle), and heat transfer (bottom) coefficients.

4.4.2 Effect of Changing Number of Molecules

A similar examination was made for the number of molecules. The standard mesh corresponds to a total of $512,800$ molecules. Two new cases were investigated using the same mesh. These two new cases correspond, on average, to $256,400$ and $1,025,600$ molecules in the entire computational domain. The effect on the skin friction, pressure and heat transfer coefficients due to variations in the number of molecules is displayed in Figure 4.4. Based on this figure, it is observed that the results are basically the same for the three cases, indicating that the standard mesh, with a total of $512,800$ molecules is enough for the computation of the flowfield properties.

4.4.3 Effect of Downstream Boundary Condition

As mentioned in chapter 3, a vacuum was defined as the boundary condition on the side IV (see Figure 3.2) in the computational domain. The vacuum option is usually used when the gas velocity through the boundary condition is supersonic. For a flowfield with a Mach number equal to or greater than three (BIRD, 1994), the flux of molecules across the boundary condition into the computational domain can be neglected. However, the downstream effect on the flow, due to the application of this boundary condition, can be estimated by increasing the length of the body. In order to determine the extent of the interference region, two other flat-plate lengths were investigated. Figure 4.5 illustrates a comparison of the aerodynamic surface quantities on the flat-plate surfaces with $60\lambda_\infty$, $80\lambda_\infty$ and $100\lambda_\infty$ of length, which correspond to a short, standard and long flat plate, respectively.

According to Figure 4.5, it is clearly seen that the imposed boundary condition affects the aerodynamic properties on the flat-plate surface in a different way. The largest effect occurs in the pressure coefficient, followed by the heat transfer coefficient and skin friction coefficient, respectively.

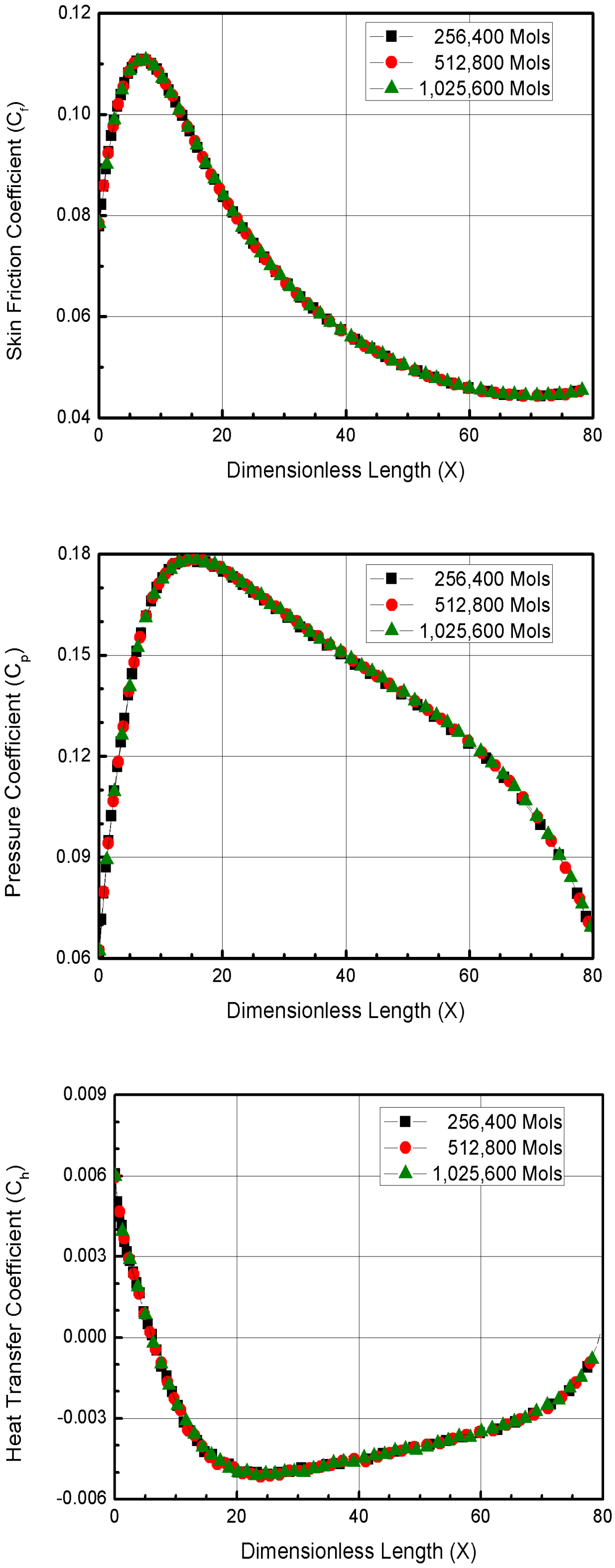

FIGURE 4.4 - Effect of changing the number of molecules on skin friction (top), pressure (middle), and heat transfer (bottom) coefficients.

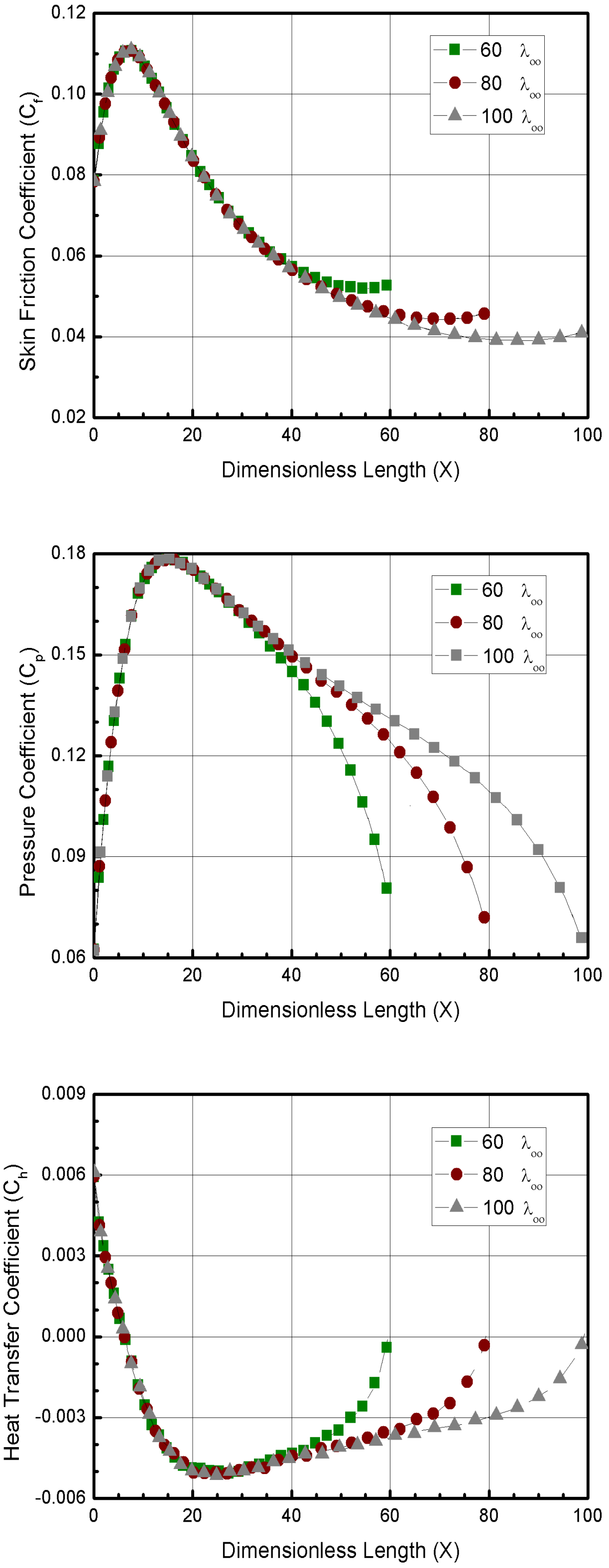

FIGURE 4.5 - Effect of changing the flat-plate length on skin friction (top), pressure (middle), and heat transfer (bottom) coefficients.

4.4.4 Experimental and Numerical Comparison

This subsection presents comparisons with experimental data and with a series of numerical simulation data on a flat plate. Basically, the purpose of this subsection is to show how well the DSMC algorithm employed in this study is able to predict rarefied hypersonic flows. By considering that these data are available in the open literature, details will be kept to a minimum and the discussion restricted to significant conclusions.

Figure 4.6 presents a series of plots for the density distribution normal to the flat-plate surface for six sections covering from 0.5 mm to 31.5 mm. In this group of plots, the density ρ is normalized by the freestream density ρ_∞, and the distance y above the flat-plate is normalized by the molecular mean free path λ_∞. Furthermore, solid lines represent the present DSMC simulations, the full and empty symbols represent, respectively, experimental and numerical data available in the literature. In addition, the dependence of the density with the axial position was measured for only three values of the y-coordinate, i.e., $y = 1.25$, 2.5 and 5.0 mm. Details of the experimental tests are given by Becker et al. (BECKER et al., 1974). The numerical simulation data shown were obtained by Hermina (HERMINA, 1989), through the DSMC method, and by Cercignani and Frezzoti (CERCIGNANI C.; FREZZOTTI, 1989) by means of the Boltzmann equation.

According to the Figure 4.6, it is clearly seen a good agreement between the present DSMC simulation data and the experimental and numerical data close to the flat-plate leading edge. However, as the trailing edge is approached, a significant disagreement is observed between experimental results and those of the present simulations, which predict higher density ratios.

Figure 4.7 illustrates the corresponding variation in tangential velocity u, normalized by the freestream velocity U_∞. As shown in this group of diagrams, for $Y \cong 0$, the tangential velocity is different from zero. This slip velocity presents a great value near the leading edge and decreases along the flat plate due to the increasing number of molecular collisions with the flat-plate surface. The comparison of the computed results with the experimental data shows that at the vicinity of the leading edge the computed velocities are larger than the measured velocities. In contrast, when the flow departs from the leading edge, the computed velocities are smaller than those obtained experimentally. According to Hermina (HERMINA, 1989), this behavior indicates that the accommodation coefficient used in the simulations is to small near the leading edge and to large at the downstream positions. In contrast to the density profiles, the velocity profiles obtained in the present DSMC simulations present a good agreement as compared to those of other numerical simulations.

Similarly, variations in temperature profiles T, normalized by the freestream temperature T_∞, are depicted in Figure 4.8. Based on these plots, it is noticed a temperature jump near to the flat-plate surface, $Y \cong 0$, in the sense that the temperature T differs from the wall temperature T_w. It is important to mention that the temperature ratio T/T_w is approximately equal to $(T/T_\infty)/29$. Therefore, the temperature at the vicinity of the flat plate reaches the wall temperature near the trailing edge. Again, in contrast to the density profiles, the temperature profiles have a good agreement when compared with those obtained experimentally and numerically.

Longitudinal variations of the flow properties are demonstrated in Figures 4.9, 4.10 and 4.11. In this group of figures, X represents the distance x normalized by the mean free path λ_∞. Also, solid lines stand for the present DSMC simulations, full and empty symbols represent experimental and numerical data, respectively.

Figure 4.9 displays the longitudinal variation of density ρ, normalized by the freestream density ρ_∞, at a distance 1.25 mm from the flat plate. According to this figure, a good agreement is observed between the present simulation and the simulation presented by Lord (LORD, 1994). However, both DSMC solutions deviate from the experimental results as the axial position increases. According to Lord (LORD, 1994) this discrepancy cannot be attributed to the surface accommodation, which appears to have very little effect, and is currently unexplained. In his analysis, the effects due of the gas-surface interaction were investigated assuming that molecules are reflected from the flat-plate surface according to the Cercignani-Lampis-Lord (CLL) (LORD, 1991) model.

The corresponding longitudinal variation of the tangential velocity u is illustrated in Figure 4.10. From this figure, it is observed a good agreement between the computational solutions. However, the comparison with experimental data shows that the calculated axial velocities drop much faster downstream of the leading edge than the measured ones.

Finally, Figure 4.11 displays the corresponding variation of the gas temperature normalized by its freestream value. From this figure, it is apparent that optimal agreement is obtained between the calculated results yielded by the DSMC method, except the calculated results presented by Hurlbut (HURLBULT, 1989a). Despite having significantly different computational results, Hurlbut (HURLBULT, 1989a) and Lord (LORD, 1994) used the same cell structure.

Comparisons between experimental and numerical simulation data were made for hypersonic gas flow of Helium over a flat plate. The examination of the numerical results leads to the conclusion that agreement with the experimental results is remarkably close to the leading edge but becomes less exact close the trailing edge. If the disagreement were attributed to the computational method, it would point out to an inadequate model for the gas-surface interaction. This hypothesis is further corroborated by the results presented by Hermina (HERMINA, 1989), Hurlbut (HURLBULT, 1989a), and Cercignani and Frezzotti (CERCIGNANI C.; FREZZOTTI, 1989), which showed a better agreement by taking into account the incomplete accommodation on the surface. However, comparisons taking into account results for incomplete accommodation on the surface are beyond the scope of the present validation process, which it is restricted only to complete accommodation on the surface.

Moreover, some caution must also be exercised in drawing definitive conclusions from comparisons since each simulation differs in some characteristics. For example, Hermina (HERMINA, 1989) considered a diverging flow of Helium gas along a flat plate, and took into account for the finite plate thickness and leading-edge bevel angle, as used in the experimental model. Cercignani and Frezzotti (CERCIGNANI C.; FREZZOTTI, 1989) assumed that the flat plate was positioned inside an axisymmetric jet originated from a sonic orifice. The interaction between the axisymmetric jet and the flat plate was not handled correctly, because the resulting 3-D flow was calculated as a 2-D one. Therefore, the effect of the jet diverging on the entire flowfield is to be expected. In addition, a uniform stream flowing parallel to the plate rather than a field having the divergence of the free jet flow has been used in the present DSMC simulation and the simulations carried out by Hurlbut (HURLBULT, 1989a) and Lord (LORD, 1994).

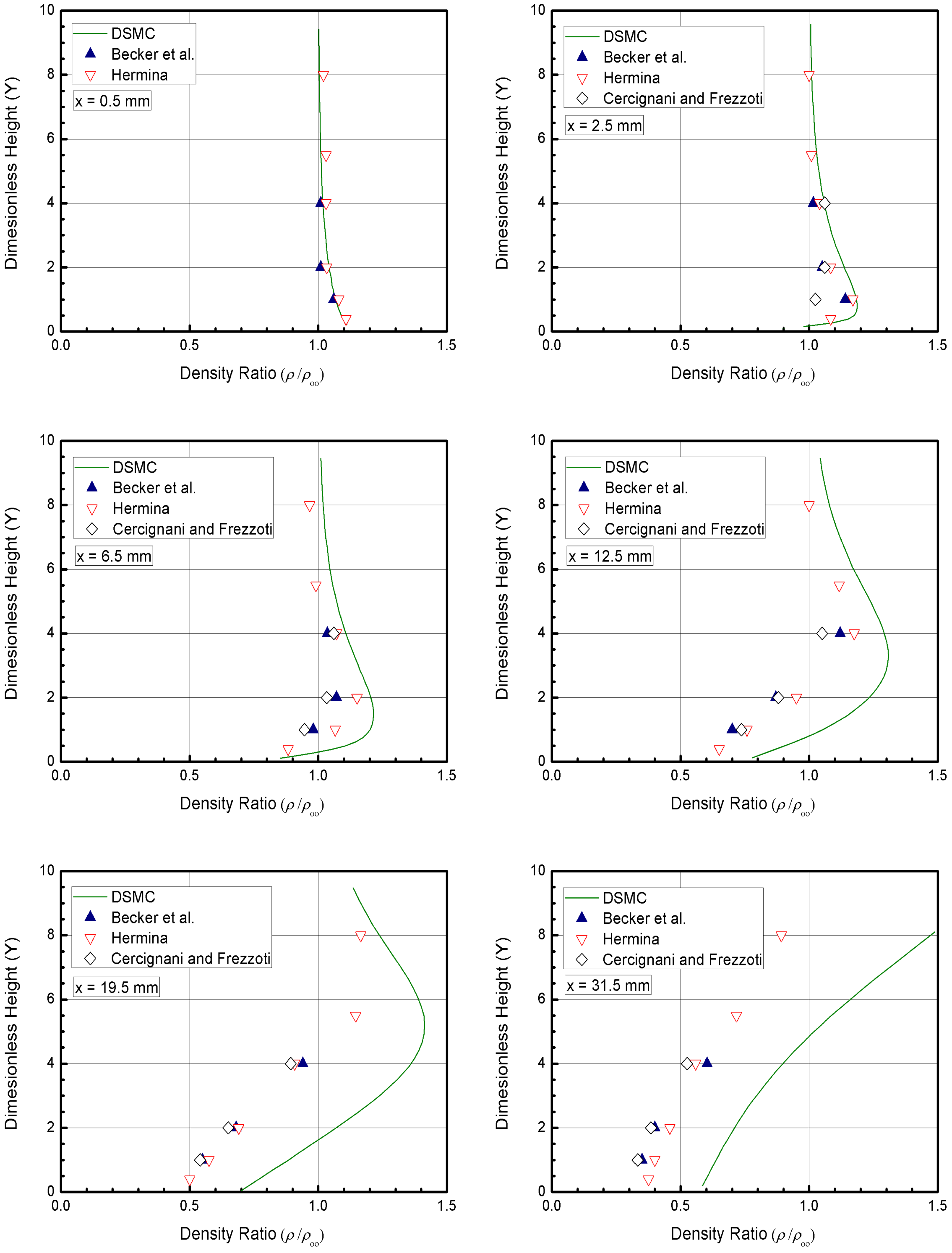

FIGURE 4.6 - Density ratio (ρ/ρ_{∞}) profiles normal to the flat-plate surface for various stations along the flat plate. Solid lines represent the present DSMC simulations, full and empty symbols represent experimental and numerical data, respectively.

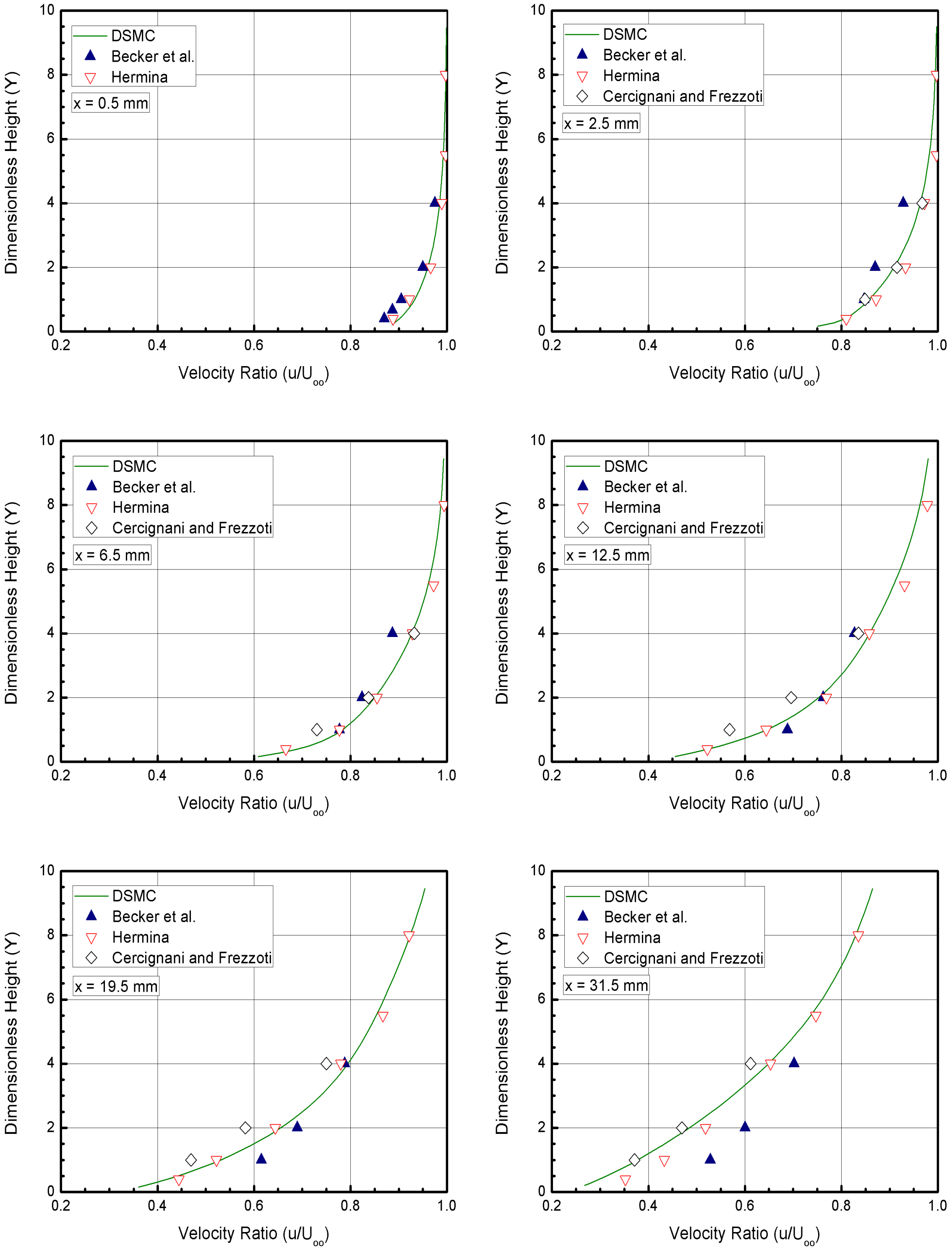

FIGURE 4.7 - Velocity ratio (u/U_∞) profiles normal to the flat-plate surface for various stations along the flat plate. Solid lines represent the present DSMC simulations, full and empty symbols represent experimental and numerical data, respectively.

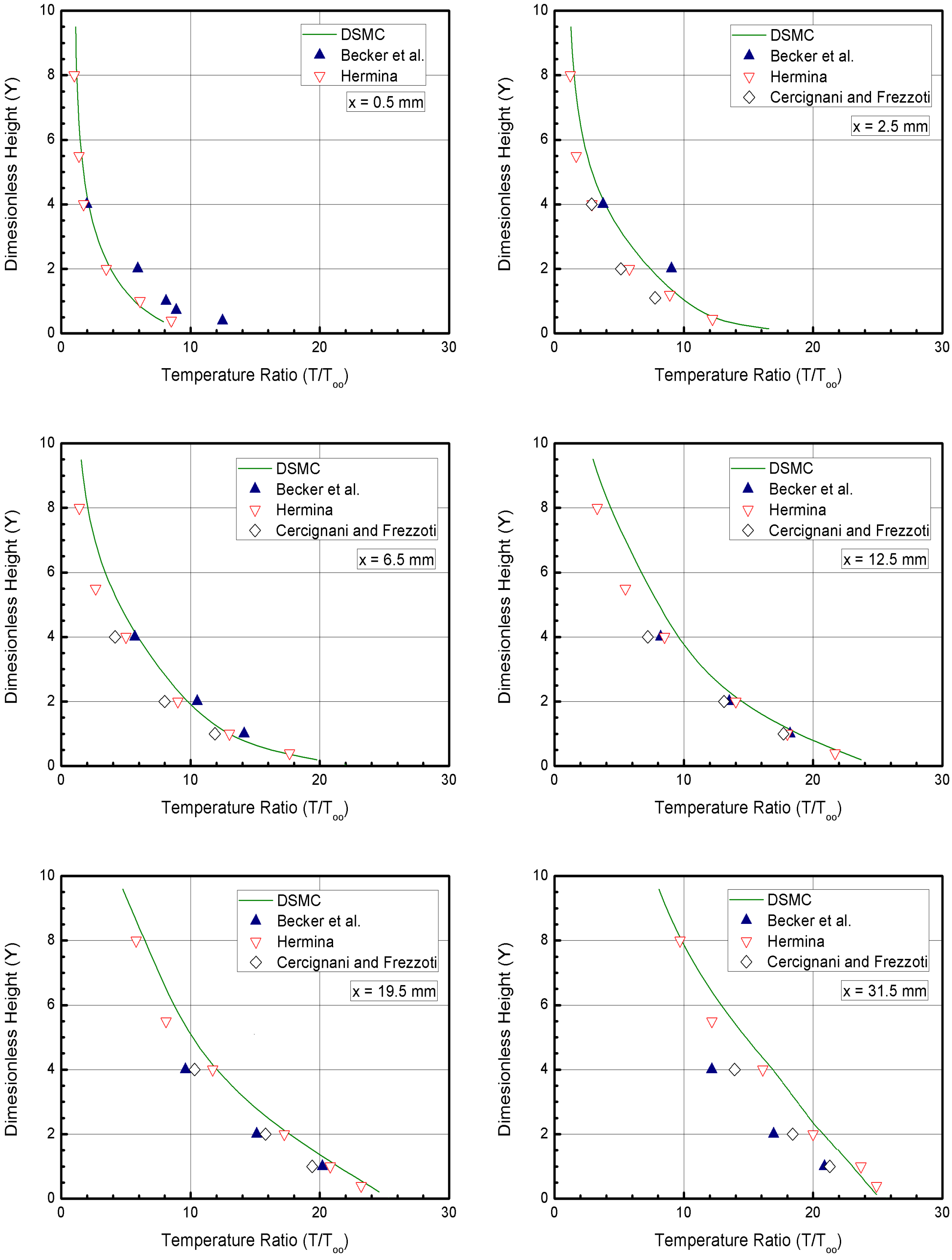

FIGURE 4.8 - Temperature ratio (T/T_∞) profiles normal to the flat-plate surface for various stations along the flat plate. Solid lines represent the present DSMC simulations, full and empty symbols represent experimental and numerical data, respectively.

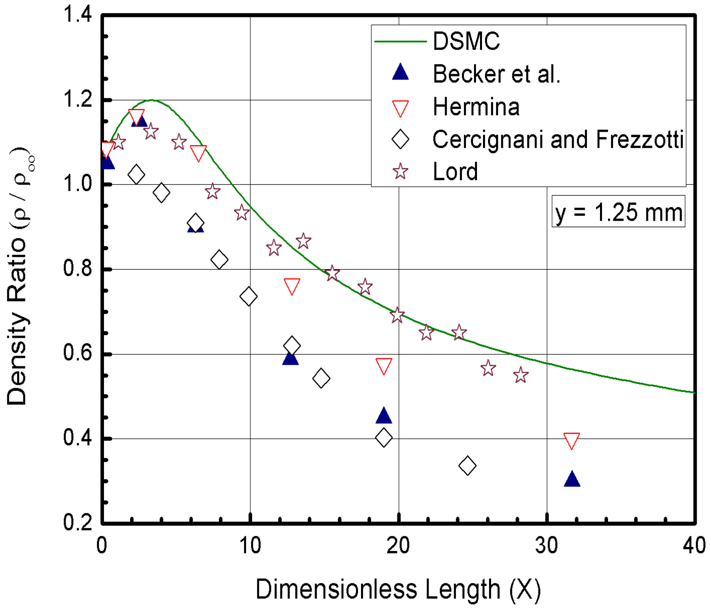

FIGURE 4.9 - Density ratio (ρ/ρ_∞) profiles along the flat-plate surface at station $y =$ 1.25mm. Solid lines represent the present DSMC simulations, full and empty symbols represent experimental and numerical data, respectively.

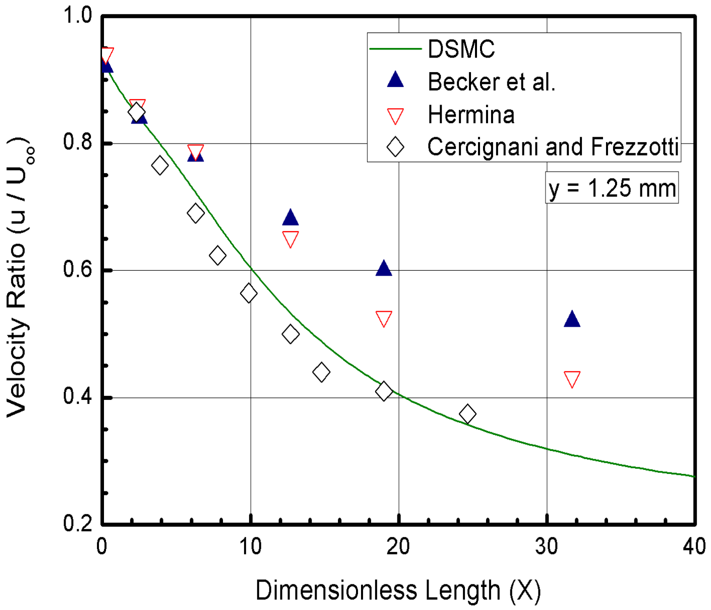

FIGURE 4.10 - Velocity ratio (u/U_∞) profile along the flat-plate surface at a station $y =$ 1.25mm. Solid lines represent the present DSMC simulations, full and empty symbols represent experimental and numerical data, respectively.

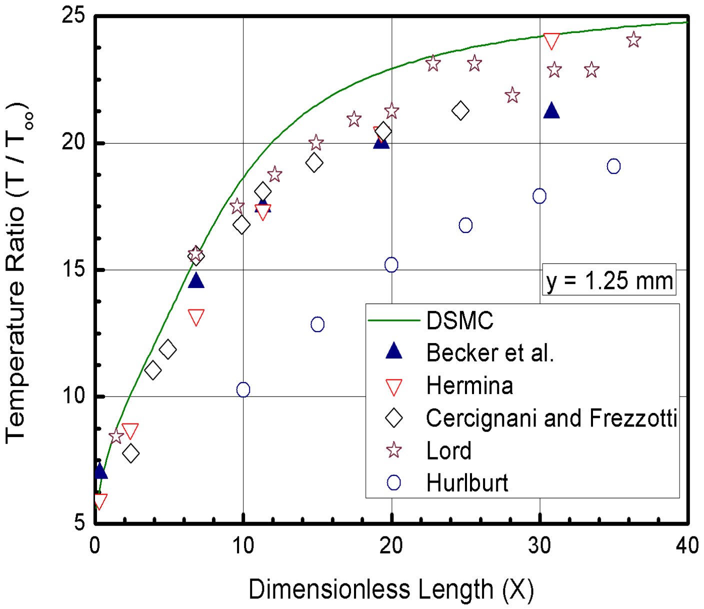

FIGURE 4.11 - Temperature ratio (T/T_∞) profile along the flat-plate surface at a station $y = 1.25$mm. Solid lines represent the present DSMC simulations, full and empty symbols represent experimental and numerical data, respectively.

4.5 Cavity Case

The simulation procedures adopted in the previous sections for the hypersonic flow over a flat plate were also applied to the cavities defined in chapter 3. Simulations were performed with computational meshes that met the general requirements for the DSMC method already presented in sections 4.1 to 4.3. As discussed, cells dimensions are more critical in the direction with high gradients. For cavities, the gradients are important in the direction normal to the cavity surface and inside of them. The computer simulations were performed by considering computational meshes containing cells distributed in four regions. Table 4.3 tabulates the number of cells employed in the four regions for coarse, standard and fine meshes for the particular case of $L/H = 1$.

TABLE 4.3 - Number of cells in the (x-direction) and [y-direction] for the L/H=1 case.

	Region 1	**Region 2**	**Region 3**	**Region 4**	**Cells number**
Coarse	(5×40)	(60×50)	(10×70)	(60×60)	$7,500$
	$[10 \times 20]$	$[120 \times 25]$	$[20 \times 35]$	$[120 \times 30]$	$7,500$
Standard	10×40	120×50	20×70	120×60	$1,000$
Fine	(20×40)	(240×50)	(40×70)	(240×60)	$30,000$
	$[10 \times 80]$	$[120 \times 100]$	$[20 \times 140]$	$[120 \times 120]$	$30,000$

The effect of altering the cell size in the x-direction was investigated for a coarse and fine meshes with, respectively, 50% less and 100% more cells with respect to the standard grid. Figures 4.12, 4.13, and 4.14 illustrate cell size effects on the skin friction, pressure and heat transfer coefficients, respectively. In this group of plots, X represents the length x normalized by the mean free path λ_∞, X' refers to the length $(x - L_u)$ normalized by the cavity length L, and Y_H refers to the height y normalized by the cavity depth H.

In analogous fashion, an examination was made in the y-direction with coarse and fine meshes with, respectively, 50% less and 100% more cells with respect to the standard mesh only in the y-direction. In addition, each mesh was made up of a non-uniform cell spacing in both directions. Moreover, point clustering is used close to the solid walls and to the horizontal plane connecting the two corners.

Figures 4.15, 4.16, and 4.17 demonstrate cell size effects on the skin friction coefficients, pressure and heat transfer coefficients, respectively. According to the two set of figures, the effect of changing cell size in both directions on the aerodynamic surface quantities was rather insensitive to the range of cell spacing considered, indicating that the standard grid, with a total of $15,000$ cells, for the $L/H = 1$ case, is essentially grid independent.

A similar examination was made for the number of molecules. The standard mesh for the $L/H = 1$ case corresponds to a total of $314,700$ molecules. Two new cases using the same mesh were investigated. These two new cases corresponds to $157,500$ and $630,600$ molecules in the entire computational domain. The impact of the number of molecules on the skin friction, pressure and heat transfer coefficients is displayed in Figures 4.18, 4.19, and 4.20, respectively. These cases presented the same results for the aerodynamic surface quantities, hence the standard mesh with a total of $314,700$ molecules is considered enough for the computation of the flowfield properties. For the propose of illustration, Figure 4.21 displays the standard mesh for the $L/H = 1$ case.

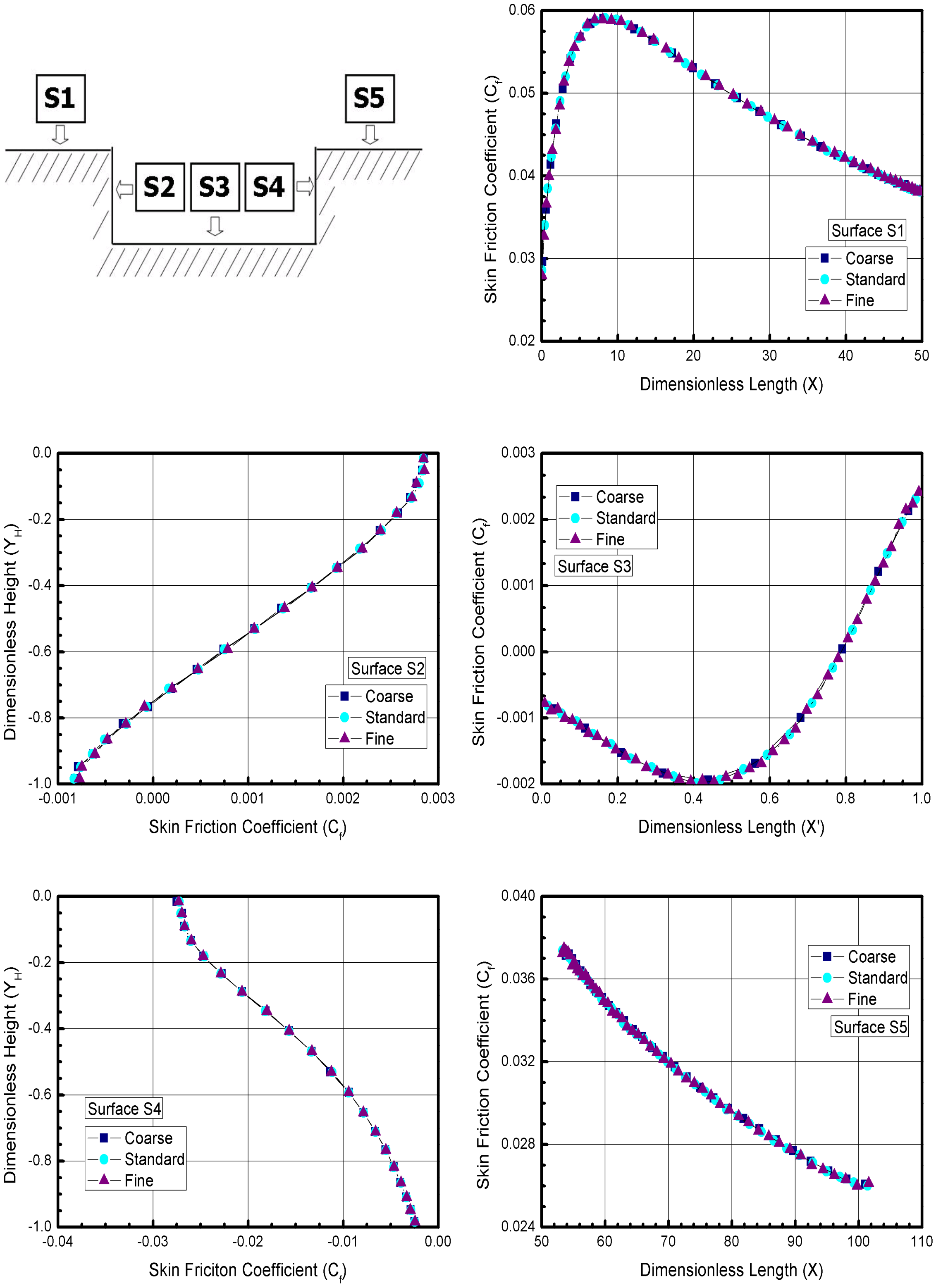

FIGURE 4.12 - Effect of changing the cell size (x-coordinate direction) on the skin friction coefficient for the $L/H = 1$ case.

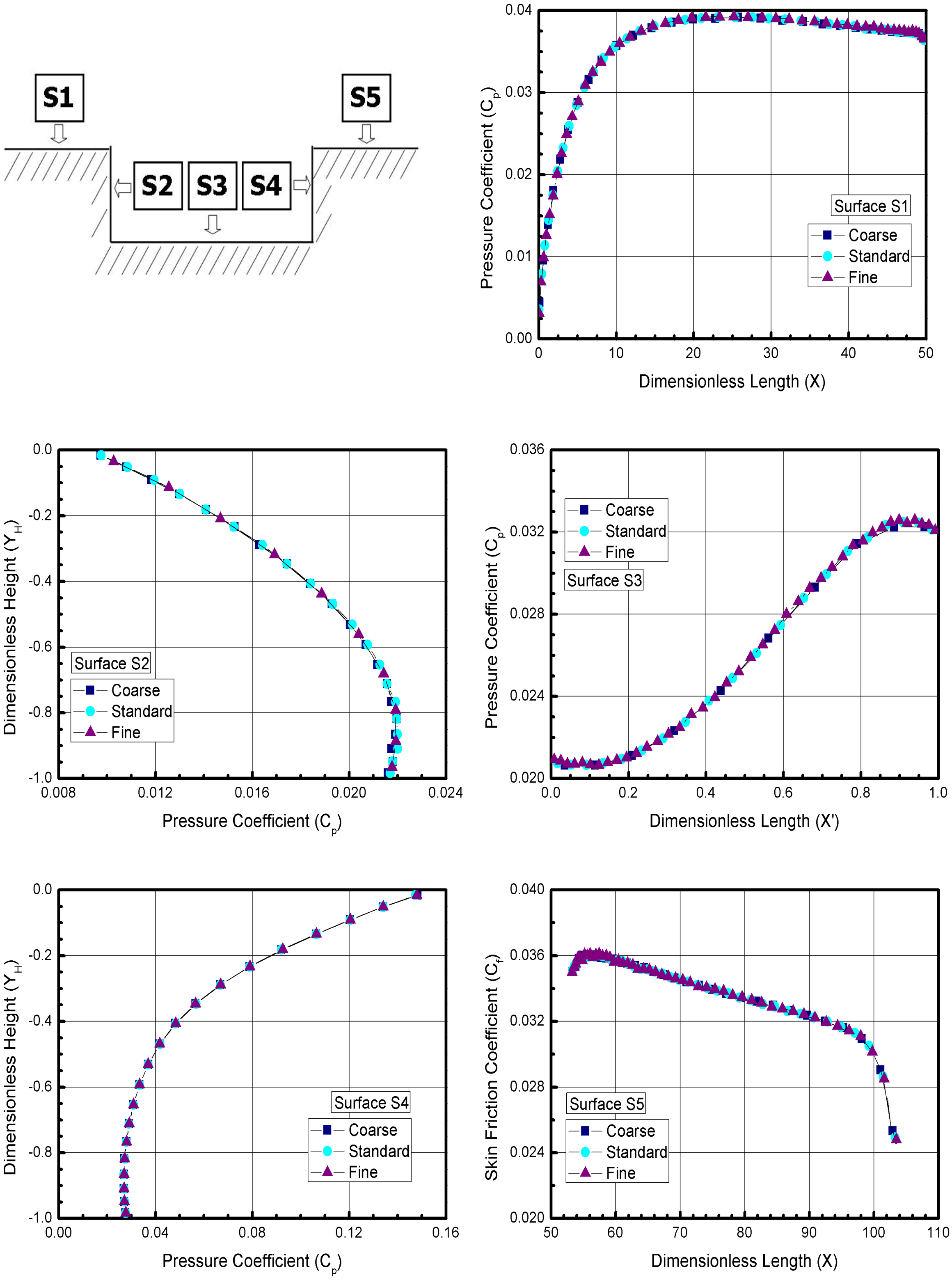

FIGURE 4.13 - Effect of changing the cell size (x-coordinate direction) on the pressure coefficient for the $L/H = 1$ case.

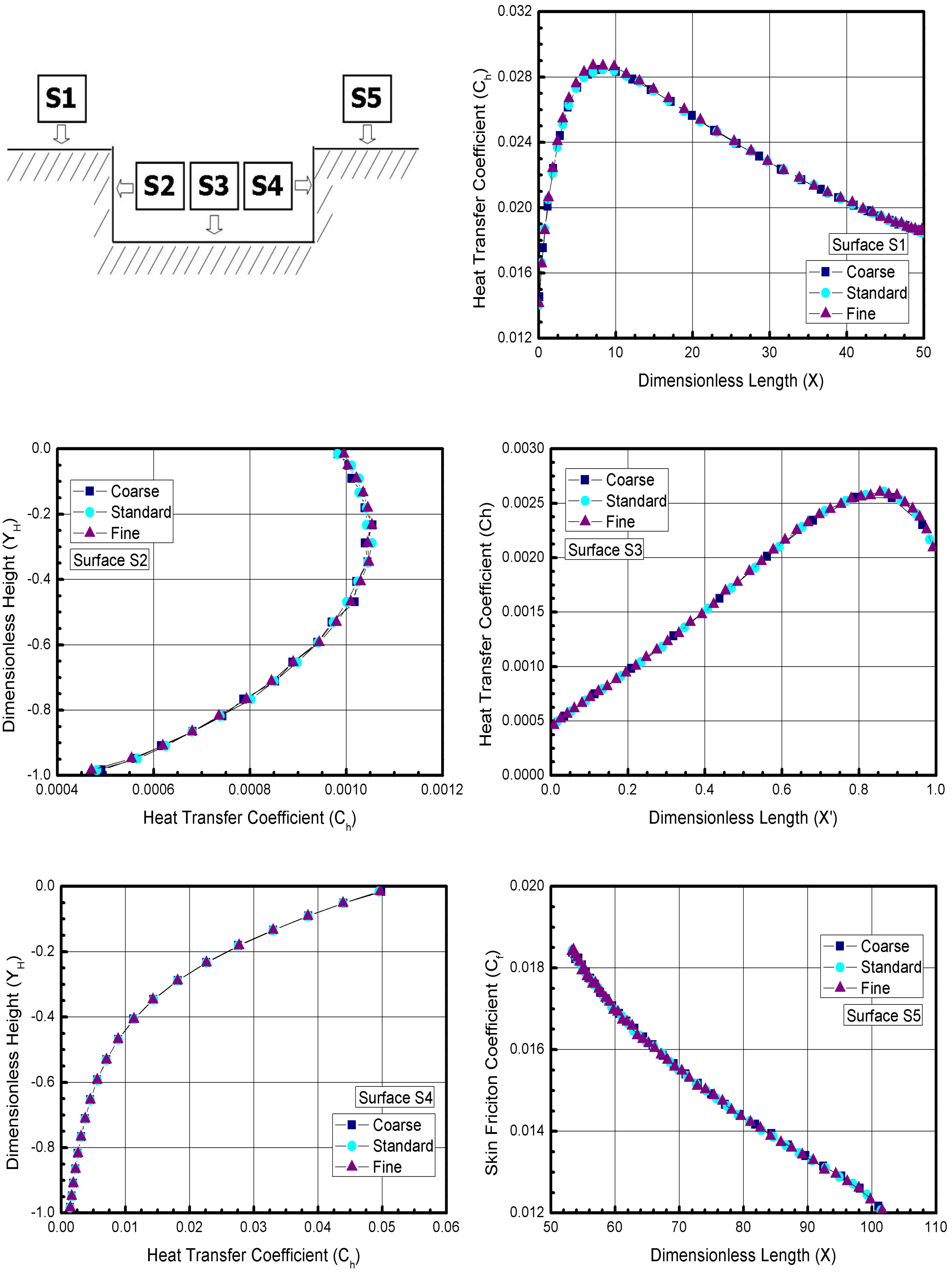

FIGURE 4.14 - Effect of changing the cell size (x-coordinate direction) on the heat transfer coefficient for the $L/H = 1$ case.

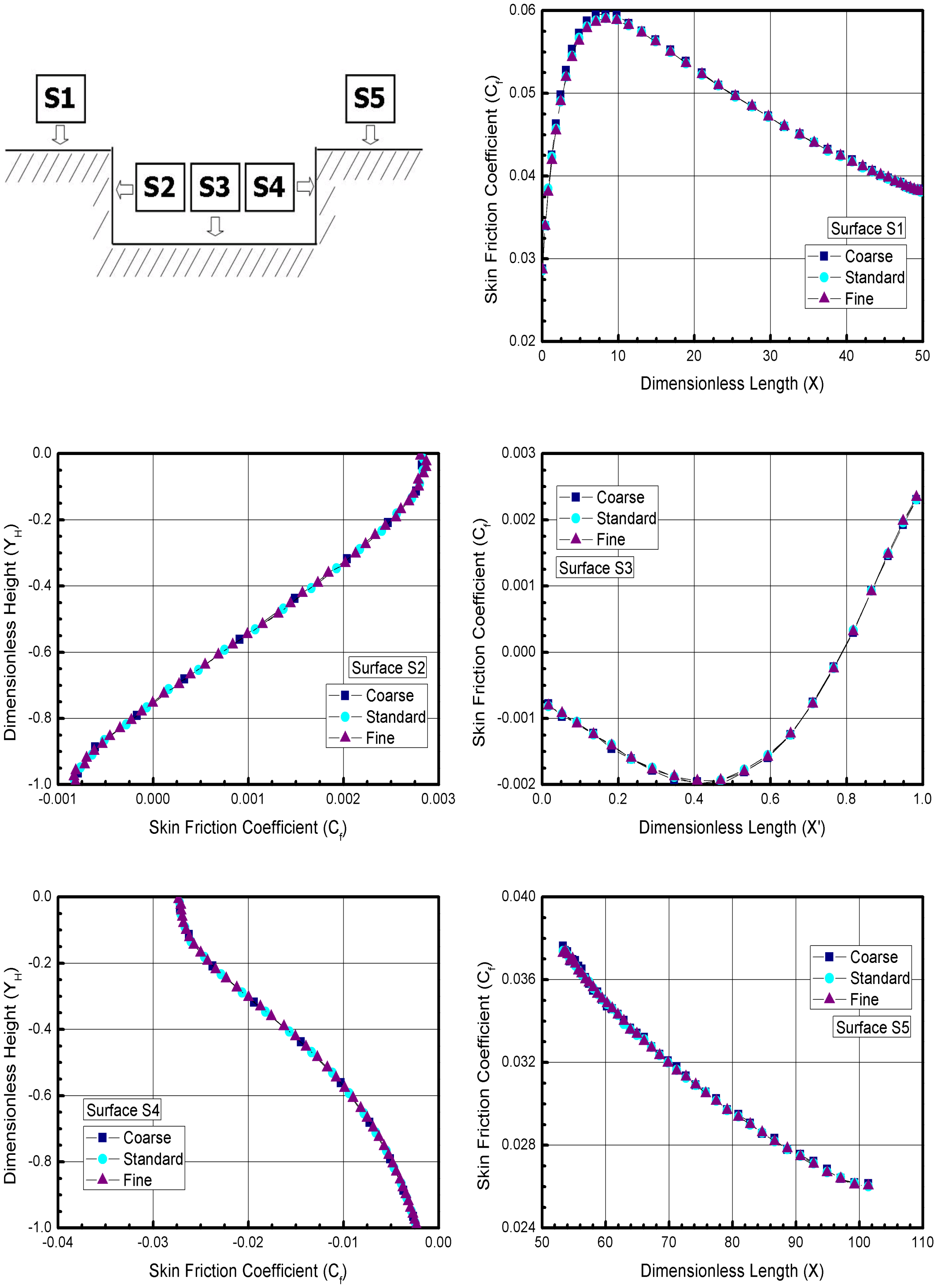

FIGURE 4.15 - Effect of changing the cell size (y-coordinate direction) on the skin friction coefficient for the $L/H = 1$ case.

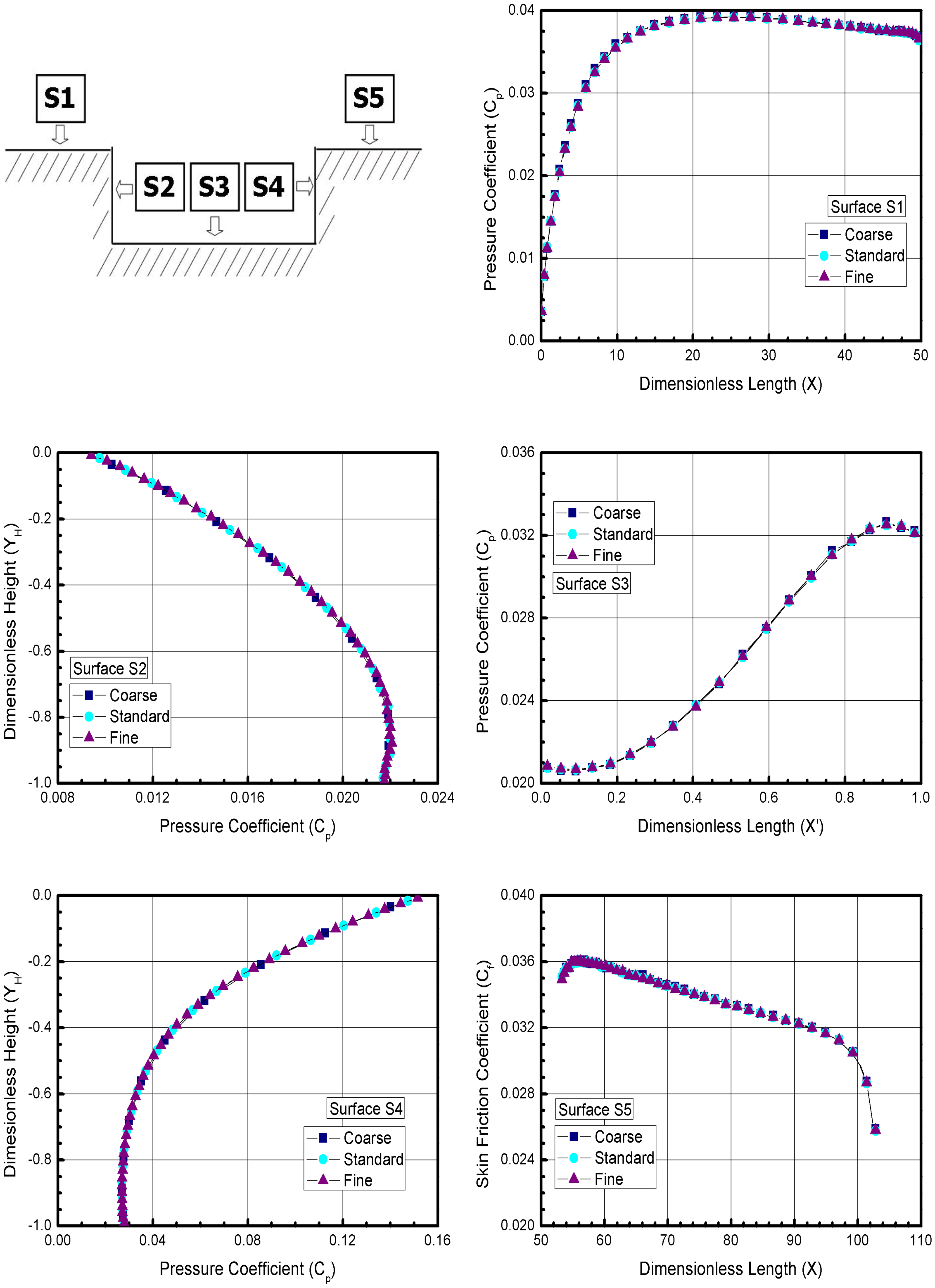

FIGURE 4.16 - Effect of changing the cell size (y-coordinate direction) on the pressure coefficient for the $L/H = 1$ case.

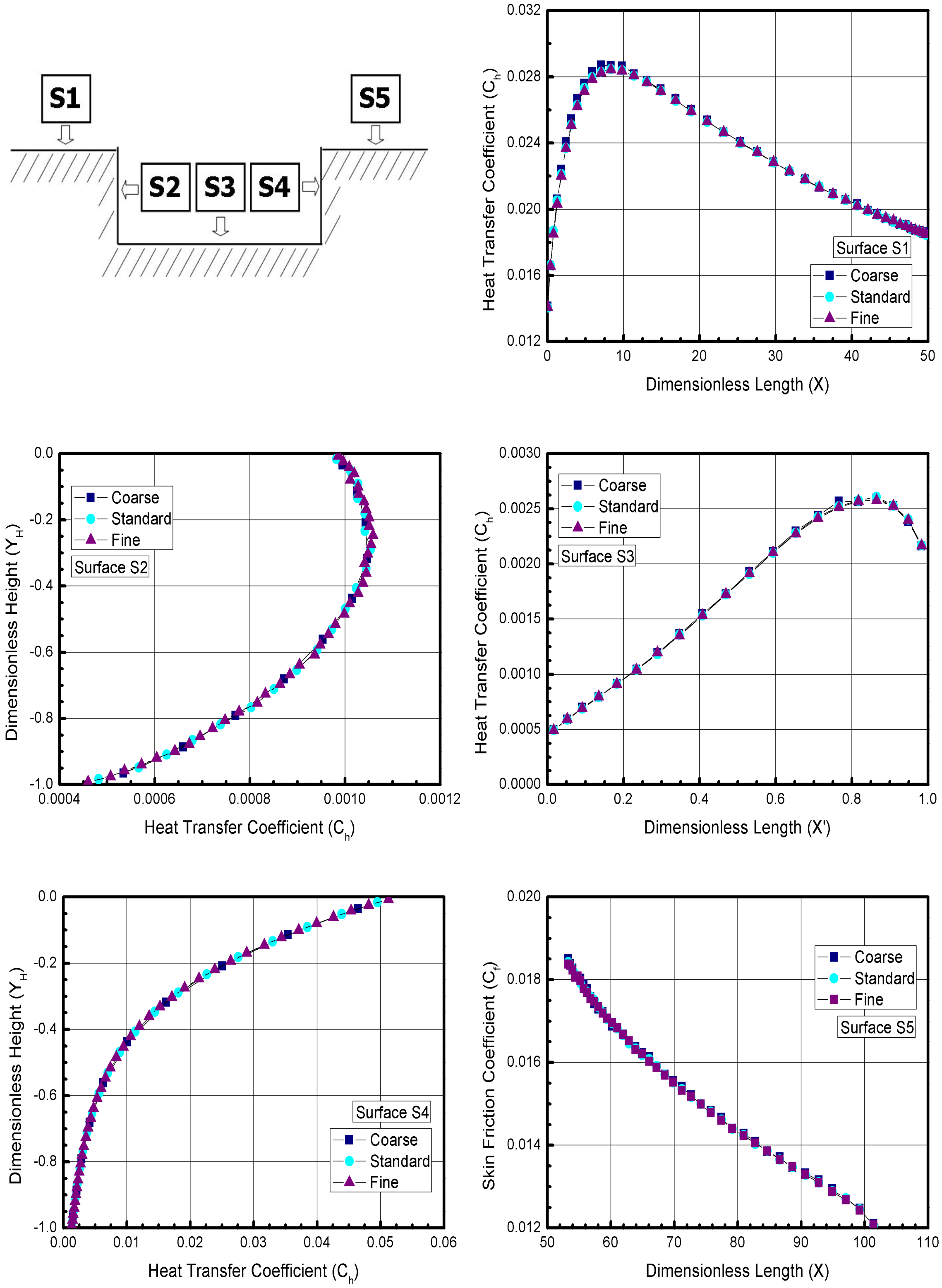

FIGURE 4.17 - Effect of changing the cell size (y-coordinate direction) on the heat transfer coefficient for the $L/H = 1$ case.

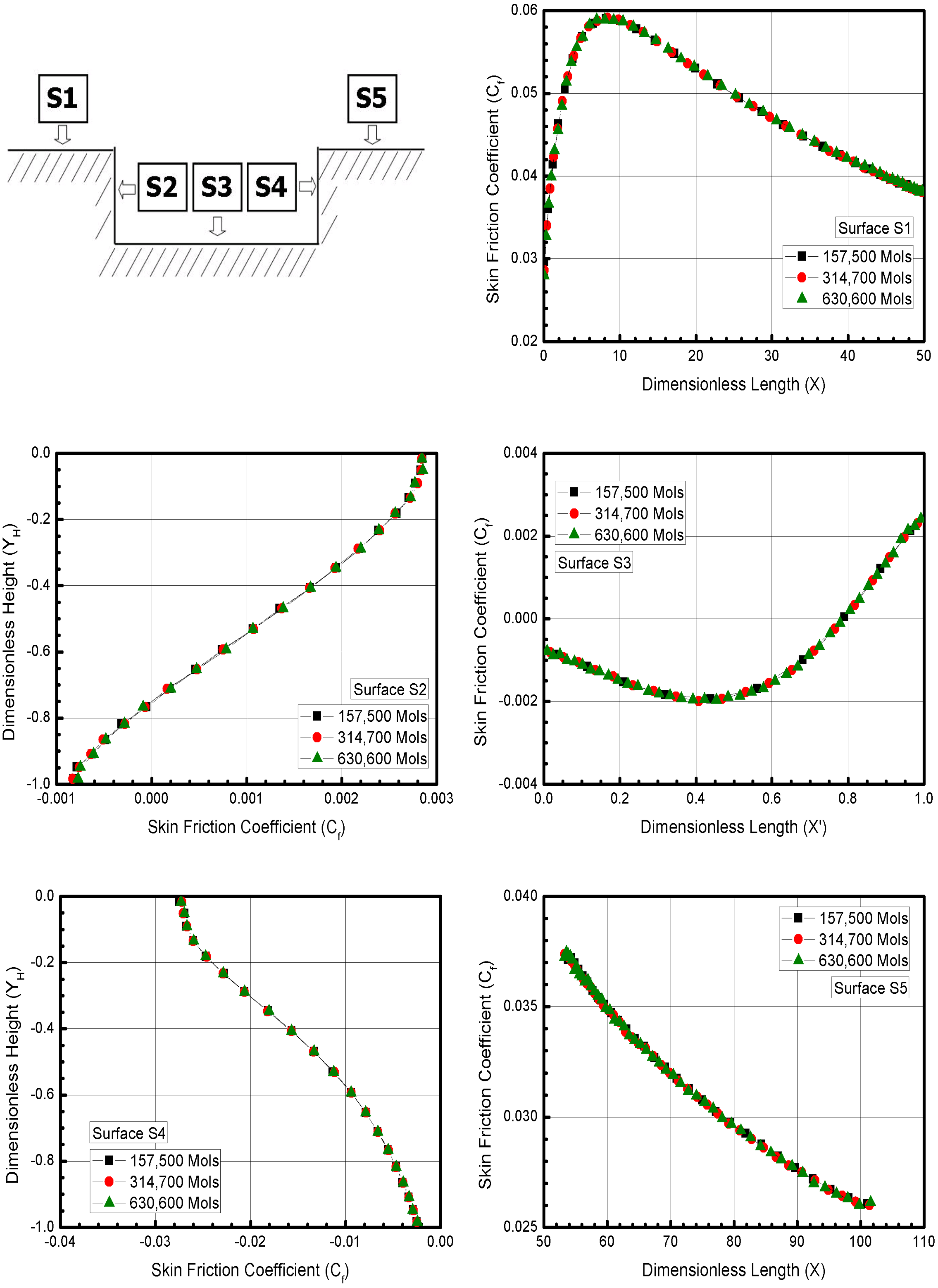

FIGURE 4.18 - Effect of changing the number of molecules on the skin friction coefficient for the $L/H = 1$ case.

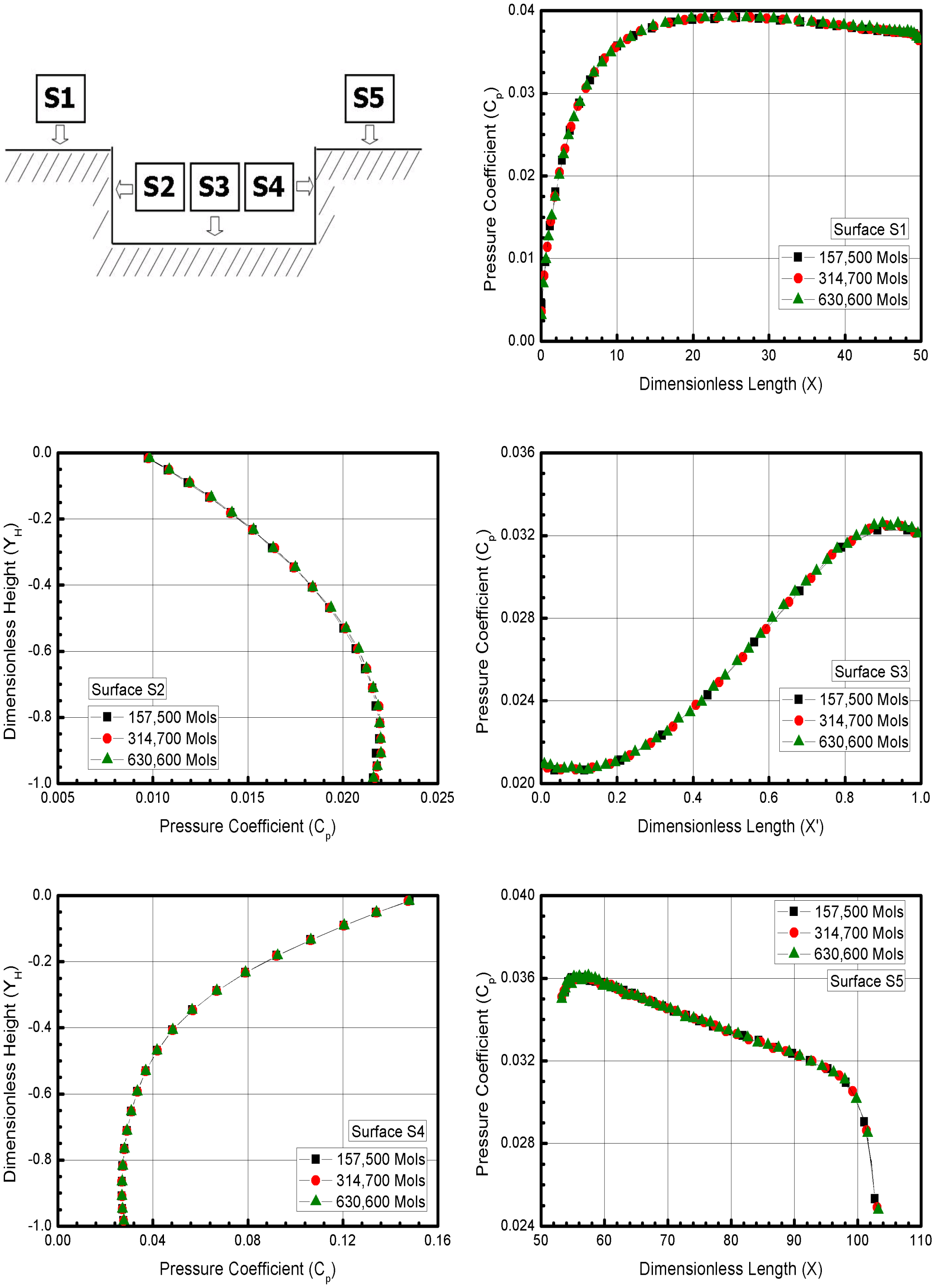

FIGURE 4.19 - Effect of changing the number of molecules on the pressure coefficient for the $L/H = 1$ case.

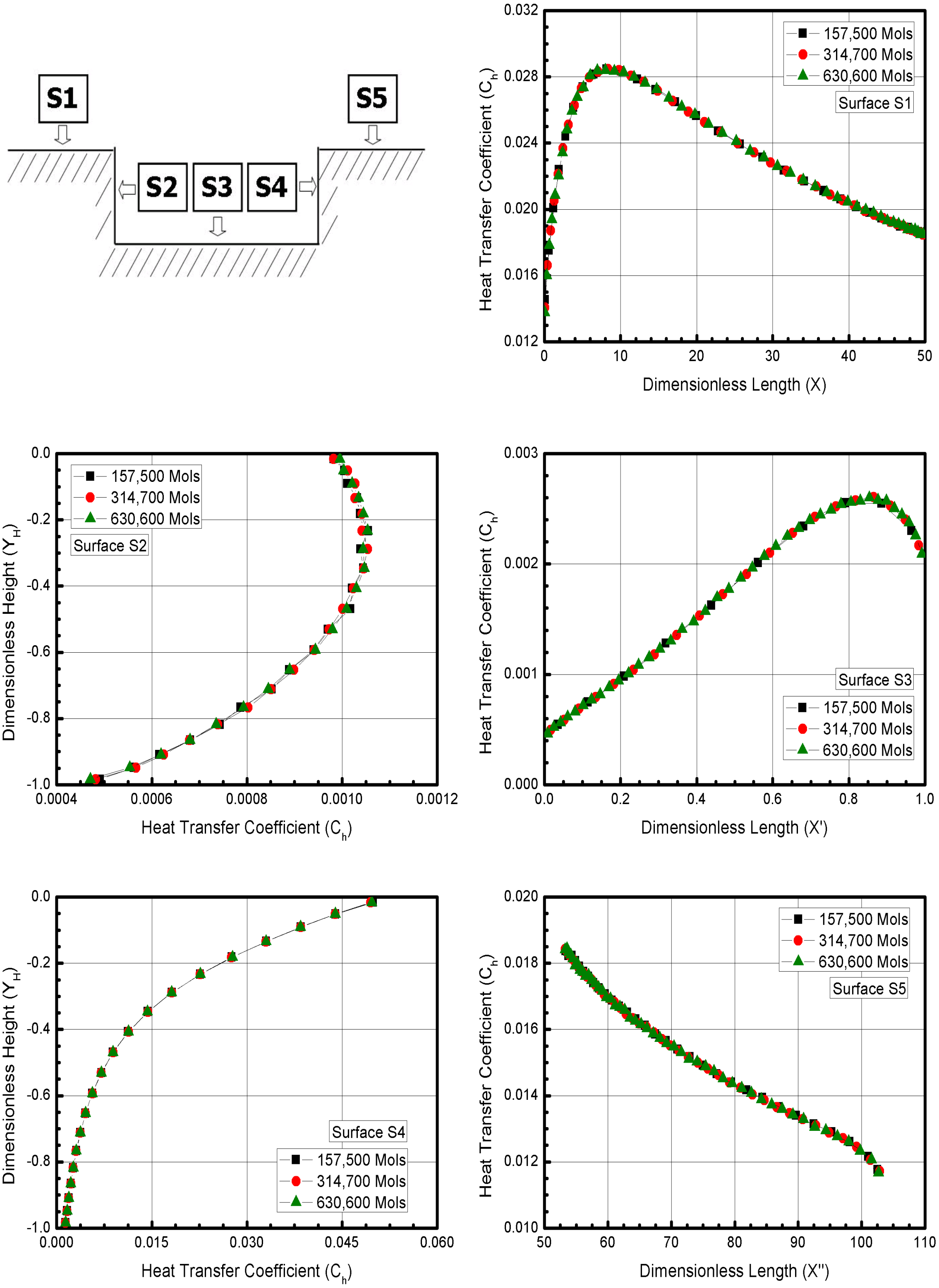

FIGURE 4.20 - Effect of changing the number of molecules on the heat transfer coefficient for the $L/H = 1$ case.

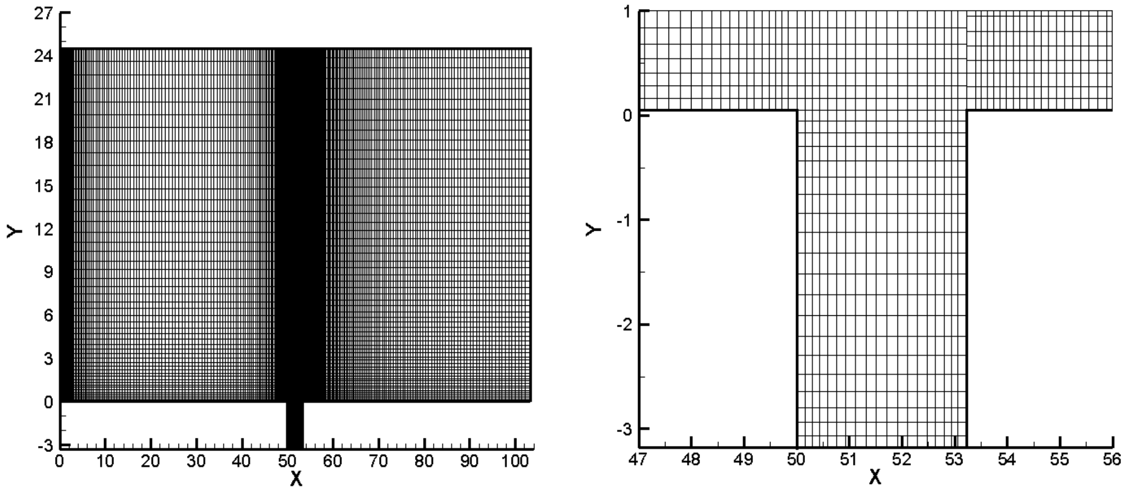
27
24
21
18
15
12
9
6
3
0
-3
Y
0
10
20
30
40
50
60
70
80
90
100
X
1
0
-1
-2
-3
Y
47
48
49
50
51
52
53
54
55
56
X

FIGURE 4.21 - Drawing illustrating the computational domain (left) and a magnified view of the cavity (right) for the $L/H = 1$ case.

s

5 COMPUTATIONAL RESULTS AND DISCUSSIONS

Having computed flowfield properties over a wide range of simulation parameters, it is worth taking a closer look at the results. In this manner, the purpose of this Chapter is to discuss and to compare differences in the flowfield structure as well as in the aerodynamic surface quantities due to variations in the cavity L/H ratio.

5.1 Flowfield Structure

This section focuses on the calculations of the primary properties obtained from the DSMC results. The primary properties of particular interest in this dissertation are velocity, density, pressure and kinetic temperatures.

5.1.1 Velocity Field

The DSMC method is essentially a statistical method. In this way, the macroscopic properties are computed as averages from the microscopic properties in each cell in the computational domain. As a result, the velocity vector is given by the following expression,

$$\mathbf{c}_0 = \frac{\sum_{j=1}^{N} m_j \mathbf{c}_j}{\sum_{j=1}^{N} m_j} \tag{5.1}$$

where N, m and $\mathbf{c}_j$ represent, respectively, the number of molecules, the mass, and the velocity vector of the molecules in each cell.

It should be remarked that the mean molecular velocity $\mathbf{c}$ ($\equiv \mathbf{c}_0 \equiv u\mathbf{i} + v\mathbf{j} + w\mathbf{k}$) defines the macroscopic mean velocity. In addition, the velocity of the molecules relative to the macroscopic mean velocity defined as thermal or peculiar velocity, is denoted by $\mathbf{c}' \equiv \mathbf{c}$ - $\mathbf{c}_0$.

The tangential velocity profiles u/U_∞ for three sections along the upstream cavity surface, surface $S1$, are illustrated in Figure 5.1 as a function of the L/H ratio. In this set of plots, the tangential velocity u is normalized by the freestream velocity U_∞, X and Y represent, respectively, the distance x and the height y normalized by the freestream mean free path λ_∞. Furthermore, for comparison purpose, the tangential velocity ratio profiles for the flat-plate case, i.e., a flat plate without cavities, are presented in the same plots.

According to Figure 5.1, it is noted that the tangential velocity profiles for the cavities are identical to those for the flat-plate case, indicating that the presence of the cavities basically does not influence the flowfield far upstream. This domain of influence is confined in a small region of a couple of mean free paths. Particular attention is paid to the magnitude of the velocity at $Y = 0$ for sections X shown. It is clearly noted that the velocity ratio is not zero at the wall; there is a velocity slip, a characteristic of a rarefied flow. As a result, the condition $u/U_\infty = 0$, no-slip velocity, does not apply in a rarefied flow.

Tangential velocity profiles for three sections along the cavity downstream surface, surface $S5$, are illustrated in Figure 5.2 as a function of the L/H ratio. In this group of plots, X''_L represents the distance $(x - L_u - L)$ normalized by L_d, the cavity downstream length. Again, for comparison purpose, the tangential velocity ratio profiles for the flat-plate case are presented in the same plots.

According to Figure 5.2, it is seen that the tangential velocity profiles for the cavities are practically identical to those for the flat-plate case, indicating that the presence of the cavities do not influence the flowfield far downstream. This domain of influence is confined in a small region close to the cavity corners. In addition, similar to the tangential velocity profiles on the surface S1, the tangential velocity ratio is not zero at the wall, there is a slip velocity, a characteristic of a rarefied flow.

An interesting characteristic in the tangential velocity profiles illustrated in Figures 5.1 and 5.2 is the similarity of the profiles along the body surface. This is an indication that the velocity profiles may be expressed in terms of functions that, in appropriate coordinates, may be independent of one of the coordinate directions. However, no attempts have been done to find such functions.

In what follows, tangential velocity profiles for three sections along the cavity surface $S3$ are demonstrated in Figure 5.3 parameterized by the L/H ratio. In this set of diagrams, the left-column diagrams correspond to u/U_∞ inside the cavity and right-column diagrams to the profiles outside the cavity. Also, the dimensionless height Y is the height y normalized by the freestream mean free path λ_∞, and X'_L is the length $(x - L_u - L/2)$ normalized by the cavity length L. In this manner, section

$X'_L = 0.25$ is located close to the cavity back face, section $X'_L = 0.50$ corresponds to the center of the cavity, and section $X'_L = 0.75$ is located at the vicinity of the frontal face.

On examining Figure 5.3, it is seen that the tangential velocity ratio is basically negative at the bottom of the cavities, at section $Y \approx -1$. After that, in the upward direction, the tangential velocity ratio becomes positive at the top of the cavities, at section $Y = 0$. Still further upward, the tangential velocity u increases significantly and tends to the freestream velocity U_∞ close to the upper boundary of the computational domain.

As a base of comparison, at section $X'_L = 0.25$, the tangential velocity ratio changes from negative to positive values at section Y of -0.2886, -0.4070, -0.5311 and -0.7665 for L/H ratio of 1, 2, 3, and 4, respectively. On the other hand, at section $X'_L = 0.75$, the velocity ratio changes from negative to positive values at section Y of -0.3467, -0.5312, -0.6533, -0.9092 for L/H ratio of 1, 2, 3, and 4, respectively. Therefore, the separated boundary layer increases with the L/H ratio and increases from section $X'_L = 0.25$ to $X'_L = 0.75$.

Normal velocity profiles inside the cavities are displayed in Figure 5.4 for three transversal sections as a function of the streamwise distance X'_L and parameterized by the L/H ratio. In this set of diagrams, the normal velocity v is normalized by the freestream velocity U_∞, and the three sections correspond to the transversal sections defined by the dimensionless height Y_H of -0.25, -0.50, and -0.75. According to these plots, near the cavity back face, $X'_L < 0.2$, the normal velocity ratio profiles basically present positive values for the L/H cases investigated, meaning that the flow is moving upward. Conversely, at the vicinity of the cavity frontal face, $X'_L > 0.8$, the normal velocity ratio profiles present negative values for $L/H < 3$, indicating that the flow is moving downward. Therefore, based on the two opposite behaviors for the normal velocity ratio, it may be inferred in passing that there is another region of clockwise circulating flow. In addition, of particular interest is the behavior of the normal velocity profiles for the $L/H = 3$ and 4 cases.

At this point, it is worth taking a closer look at the recirculation region. In this manner, streamline traces inside the cavities are depicted in Figure 5.5. In this set of plots, the dimensionless height Y_H is the height y normalized by the cavity height H, and X'_L is the length $(x - L_u)$ also normalized by the cavity length L. Based on these plots, it is clearly noticed that the flow within the cavities are characterized by the appearance of recirculation regions. For the $L/H = 1$ case, the streamline pattern shows that the flow is characterized by a primary vortex system. For the $L/H = 2$ case, a similar flow structure is observed. Nevertheless, in contrast to the previous case, the vortex core approached the frontal face of the cavity. In addition, for the $L/H = 1$ and 2 cases, it is noteworthy that the recirculation region fills the entire cavities. In the following, for the $L/H = 3$ case, a different flow structure is observed; two vortices are formed, one of them close to the back face and another one near the frontal face of the cavity. It should be remarked that the external stream does not reach the bottom surface of the cavity. Finally, for the $L/H = 4$ case, the recirculation regions are well defined when compared to the previous case. Furthermore, for this particular case, the external flow reaches the cavity floor. It should be emphasized that the flow topology observed here for the $L/H = 4$ case in a rarefied environment is usually observed in the continuum flow regime for $L/H > 14$, which represents that for a “closed cavity”, as shown in **Chapter1**.

Before proceeding with the analysis of density profiles, it proves instructive to illustrate the distribution of Mach number in the cavities. In doing so, Figure 5.6 displays contour maps for the distribution of Mach number in the entire computational domain. In this family of plots, dimensionless height Y stands for the height y normalized by the freestream mean free path λ_∞, and the dimensionless length X refers to the length x also normalized by the λ_∞. Also, the plots in the left column represent the Mach number in the entire computational domain, and the plots in the right column correspond to a magnified view of the Mach distribution inside the cavities. Moreover, attention should be paid to the different Mach number scale used in right-column plots. According to the plots in the right column, it is firmly established that the Mach number at the vicinity of the back-face corner is larger than that at the vicinity of the frontal-face corner, as a result of the flow separation and flow reattachment on these faces.

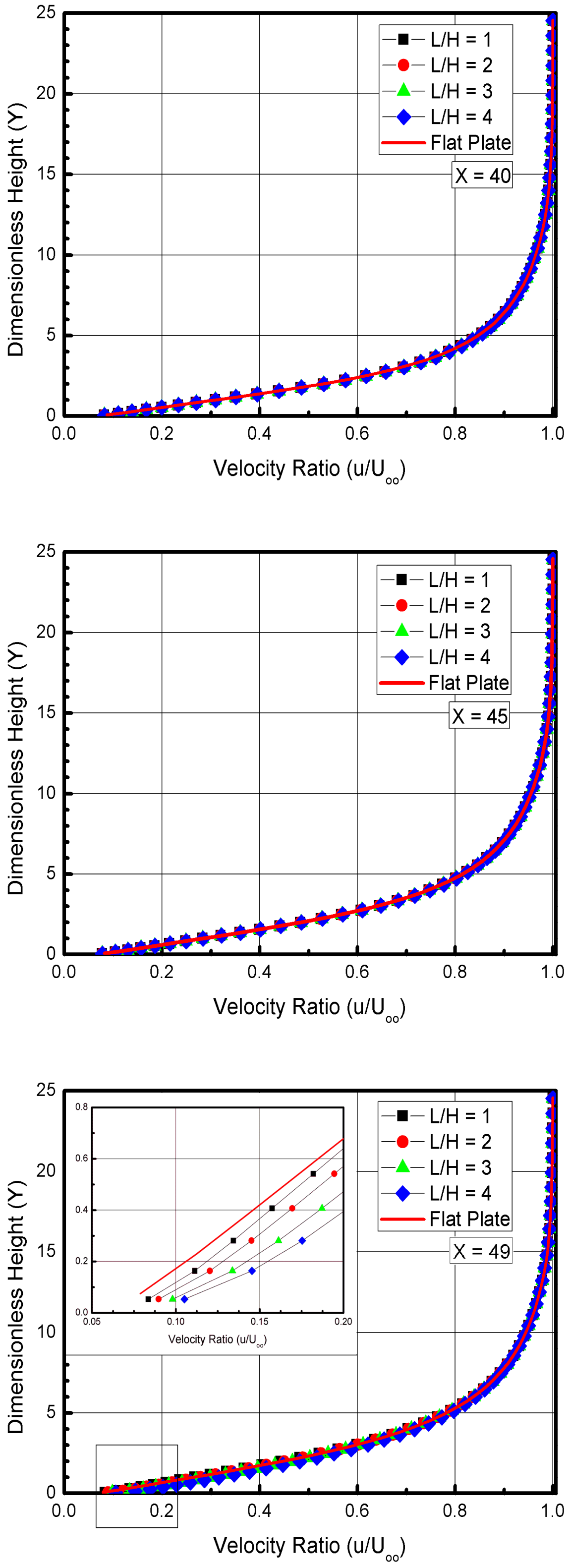

FIGURE 5.1 - Tangential velocity ratio (u/U_∞) profiles for three sections along the surface $S1$ parameterized by the L/H ratio.

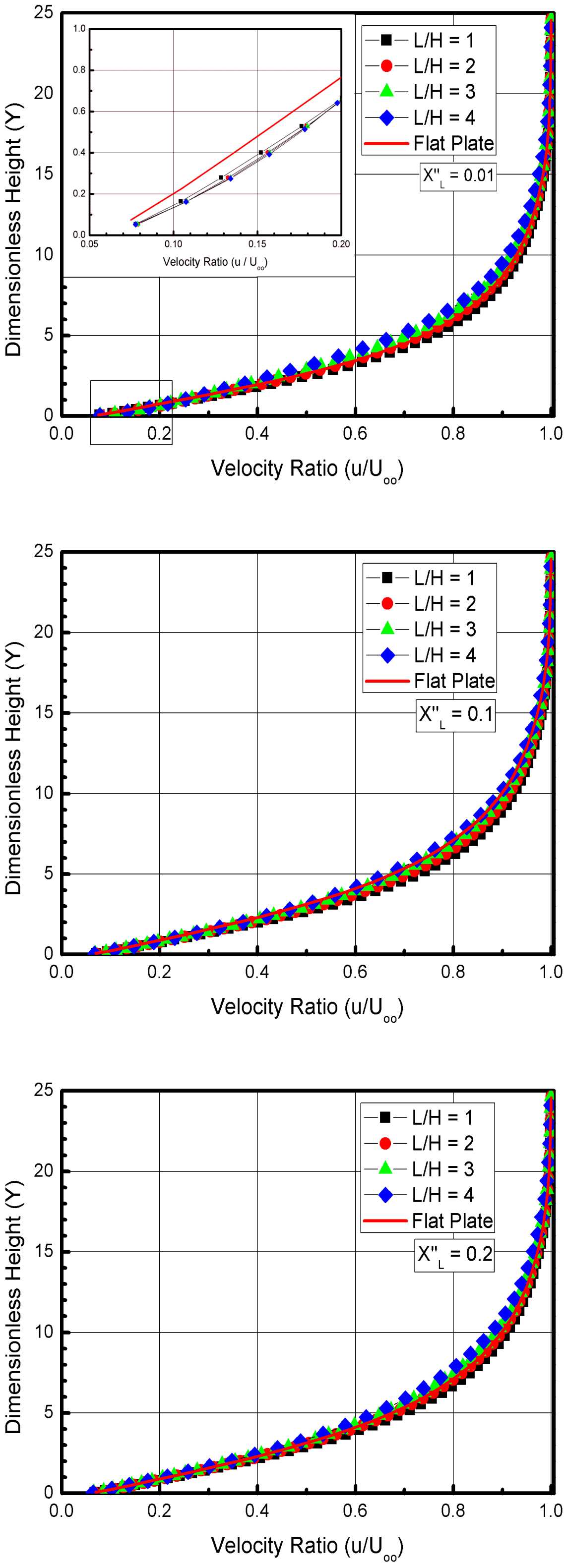

FIGURE 5.2 - Tangential velocity ratio (u/U_∞) profiles for three sections along the surface $S5$ parameterized by the L/H ratio.

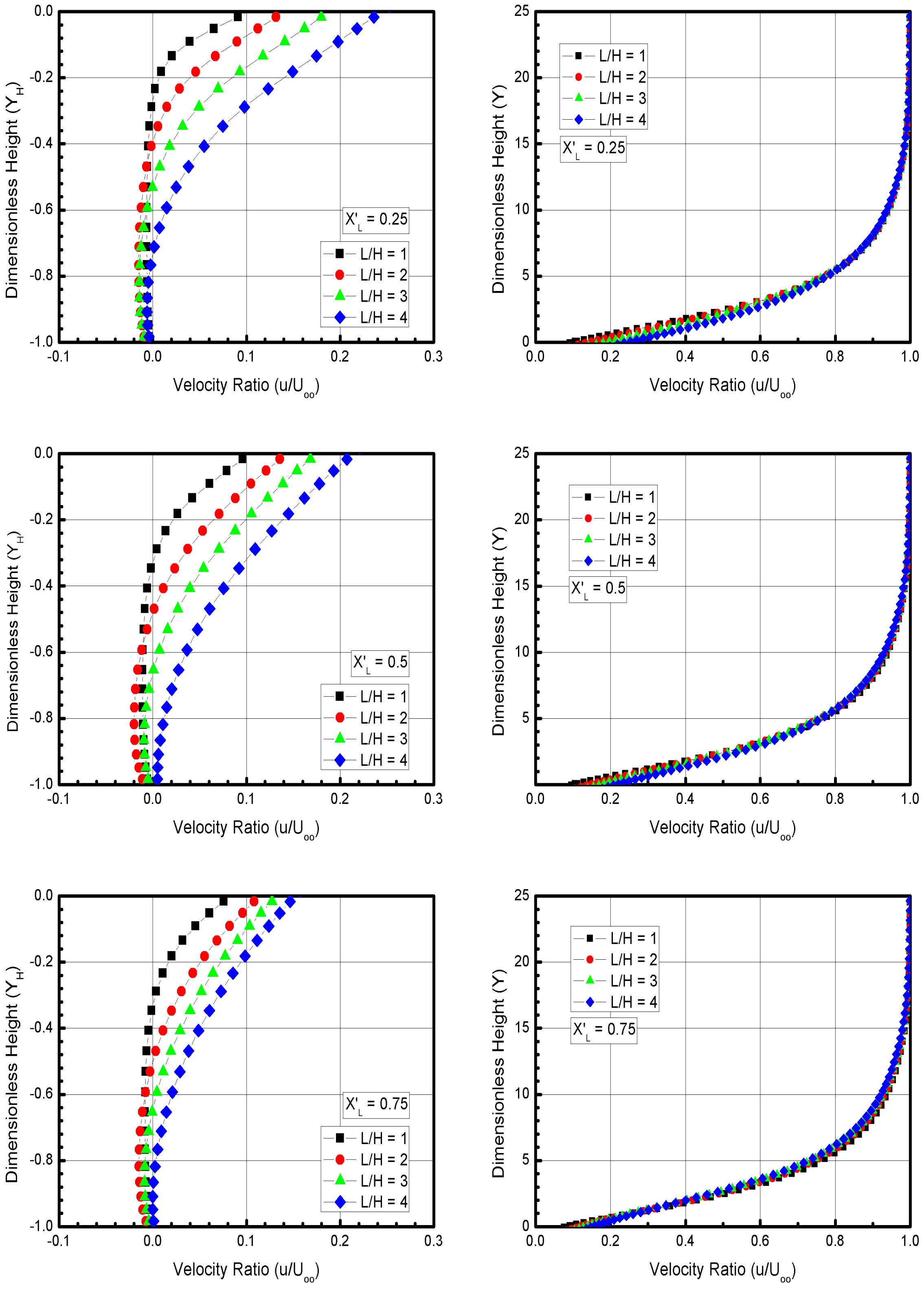

FIGURE 5.3 - Tangential velocity ratio (u/U_∞) profiles for three sections along the surface $S3$ parameterized by the L/H ratio.

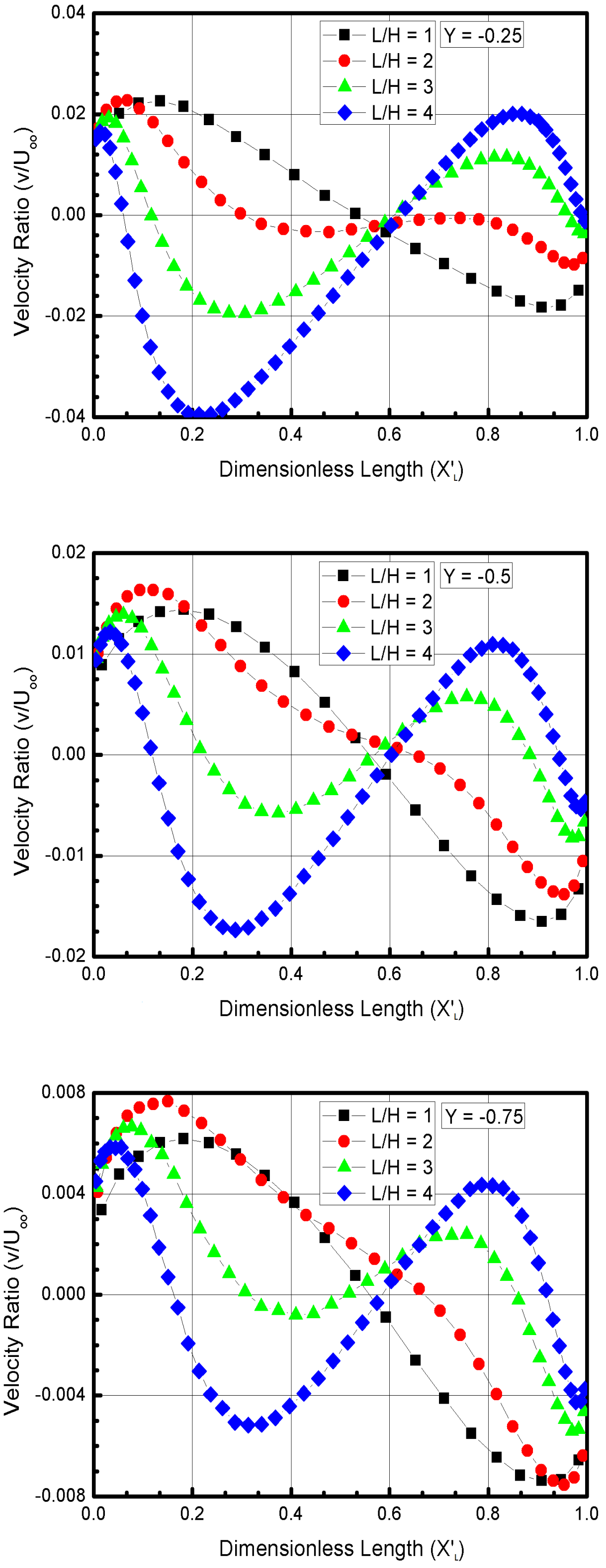

FIGURE 5.4 - Normal velocity ratio (v/U_∞) profiles for three transversal sections inside the cavity as a function of the dimensionless length X'_L.

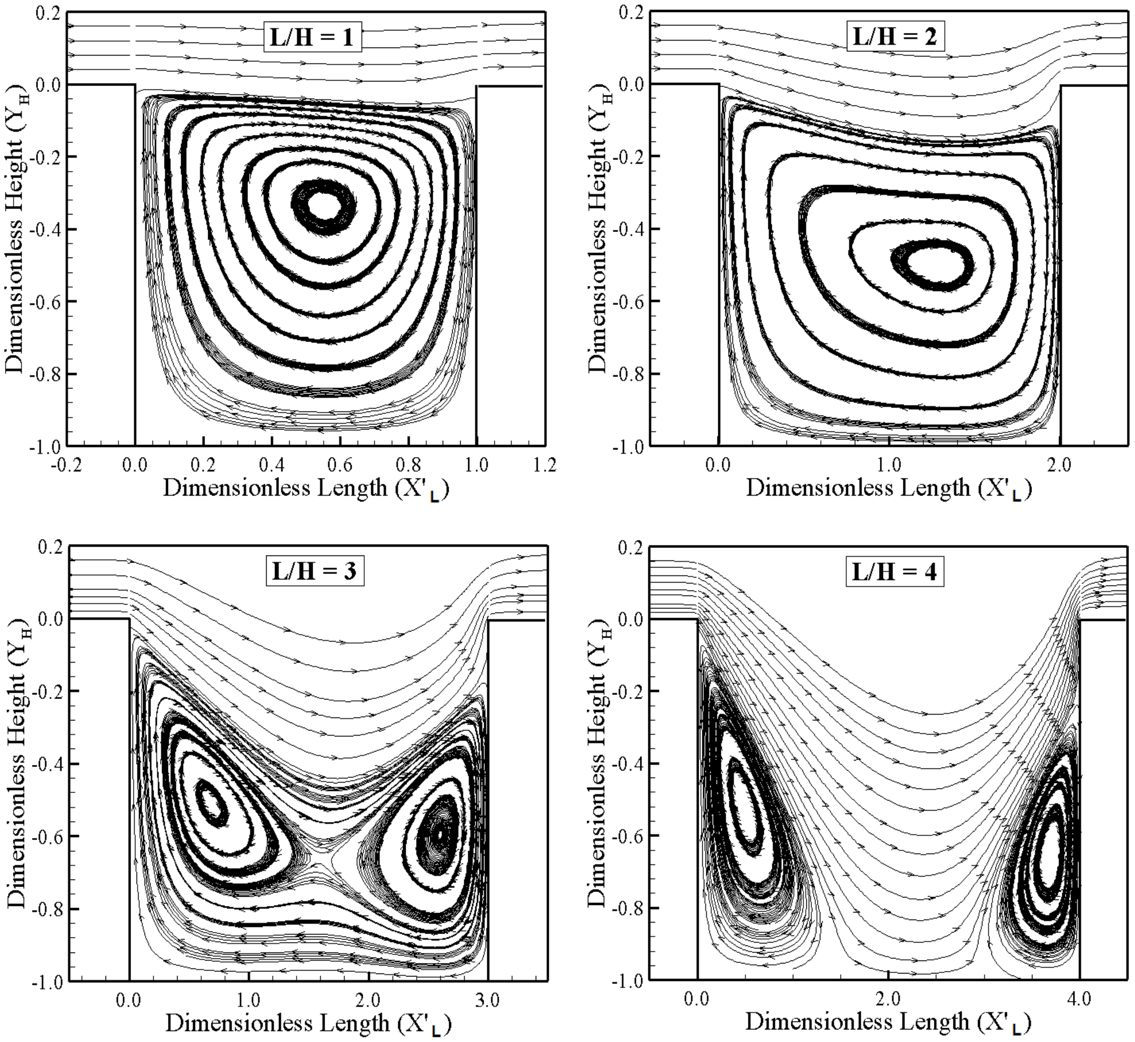

FIGURE 5.5 - Distribution of streamline traces inside the cavities for L/H of 1, 2, 3 and 4.

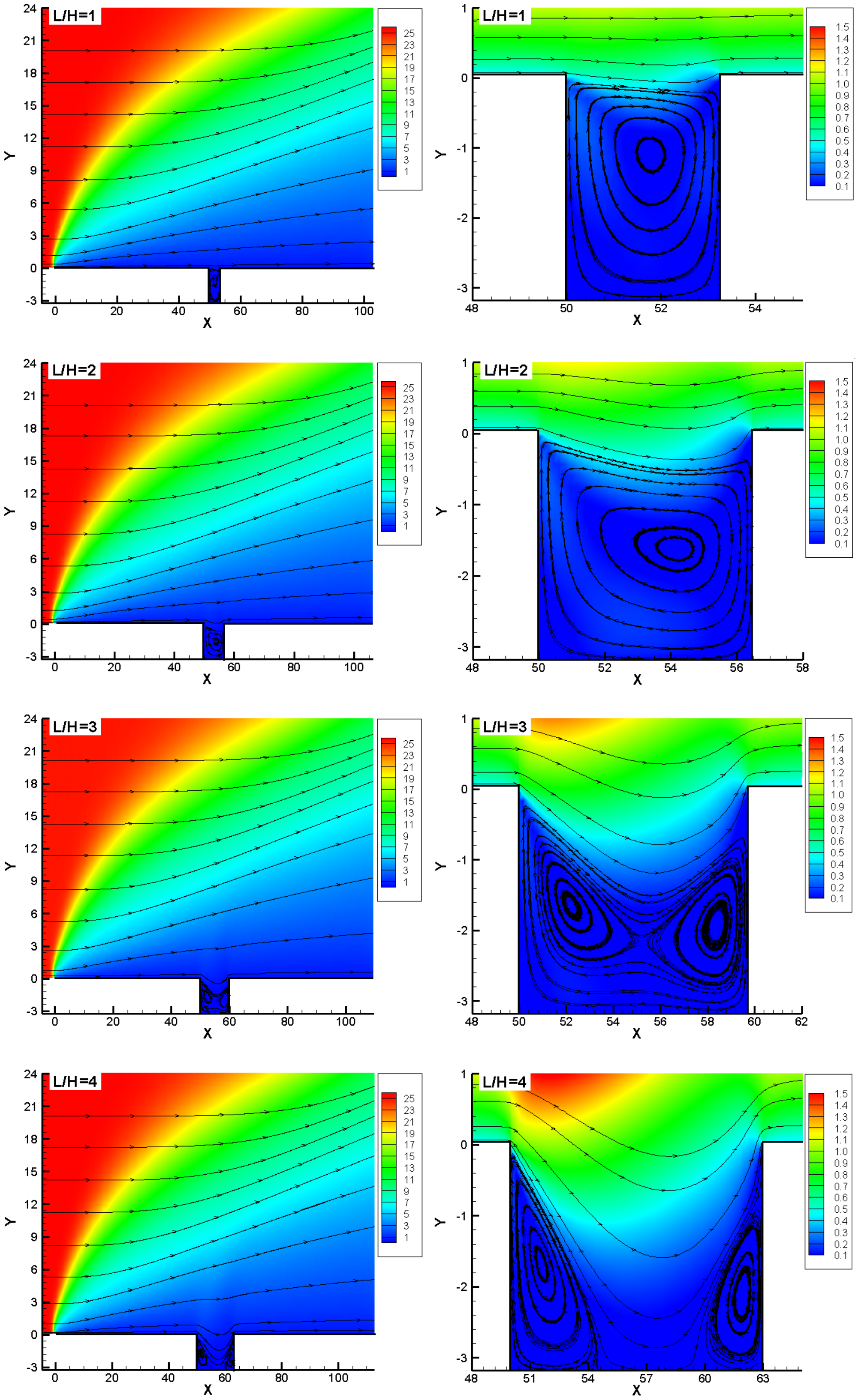

FIGURE 5.6 - Mach number distribution outside (left) and inside (right) the cavities for L/H ratio of 1, 2, 3 and 4.

5.1.2 Density Field

The density in each cell in the computational domain is obtained by the following expression,

$$\overline{\rho} = \frac{1}{NV_c}\sum_{j=1}^{N} m_j \tag{5.2}$$

where N is the number of molecules in the cell, m the mass of molecules and V_c the volume the cell.

The impact on the density profiles due to changes on the L/H ratio is illustrated in Figure 5.7 for three sections along the cavity upstream surface, surface $S1$. In this group of plots, density ρ is normalized by the freestream density ρ_∞, X and Y are dimensionless length and height, respectively, as defined previously in the velocity ratio profiles. Besides, as a base of comparison, density ratio profiles for the flat-plate case are presented in the same plots.

According to Figure 5.7, it is observed that the density ratio experiences significant changes in the direction perpendicular to the surface $S1$ as the flow moves downstream along the surface. The density ratio is high adjacent to the wall, $Y \approx 0$, and rapidly decreases inside a layer of thickness around two to three freestream mean free paths, where the density ratio is less than one for the sections shown. It means that the density is smaller than the freestream density ρ_∞. This characteristic is observed when the body surface is very much colder than the stagnation temperature of the incoming gas. As a result, the gas near the body surface tends to be much denser and cooler (see next sections) than the gas in the rest of the boundary layer. As Y increases, the density ratio increases significantly at a maximum value, around $\rho/\rho_\infty = 1.6$, inside the shock wave. After that, the density decreases and reaches the freestream density value as $Y \to \infty$.

Still referring to Figure 5.7, it is noticed that, for section $X < 45$, the density ratio profiles for the cavities are identical to those for the flat-plate case, indicating that the presence of the gaps does not influence the flowfield far upstream. However, for section $X \approx 50$, density ratio for the cavities is smaller than that for the flat-plate case, indicating that the presence of the cavities is only felt a small distance upstream the cavity corner, due to the flow expansion around the cavity corner.

Effects on the density profiles due to changes on the L/H ratio is demonstrated in Figure 5.8 for three sections along the cavity downstream surface, surface $S5$. Based on this group of plots, it is noticed that density ratio profiles are similar to those for the tangential velocity profiles in that profiles for the cavities are practically identical to those for the flat-plate case, except very close to the cavity corners. Therefore, this behavior indicates that the presence of the cavities basically do not influence the flowfield far downstream. The influence is confined in a small region very close to the cavity corners.

Effects of the L/H ratio on density ratio profiles along the cavity surface $S3$ are displayed in Figure 5.9 for three sections defined by X'_L of 0.25, 0.50, and 0.75. In this set of plots, similar to the tangential velocity profiles, the left-column plots correspond to ρ/ρ_∞ inside the cavity and right-column diagrams to the profiles outside the cavity. Also, the dimensionless height Y and length X'_L are similar to those defined in the tangential velocity profiles.

Referring to Figure 5.9, it may be recognized that the density ratio presents significant changes not only in the direction perpendicular to the cavity surface but also along the cavity bottom surface, surface S3. At section $X'_L = 0.25$, it is observed that the density ratio decreases with the L/H ratio rise. For $L/H = 3$ cases, the density ρ is smaller than the freestream density ρ_∞. This behavior is explained by the fact that with increasing the L/H ratio, the flow penetrates more deeply inside the cavity due to the flow expansion around the corner of the cavity back face. As a result, a recirculation zone is formed characterized by a zone of low density. Conversely, at section $X'_L = 0.75$, the flow experiences a compression, and the density ρ is well above the freestream density ρ_∞, with increasing the L/H ratio.

Finally, in attempting to bring out the essential features of the density behavior in the cavities, Figure 5.10 displays contour maps for the density ratio distribution in the entire computational domain. In this group of plots, similar to the Mach number distribution, dimensionless height Y stands for the height y normalized by the freestream mean free path λ_∞, and the dimensionless length X refers to the length x also normalized by the λ_∞. Furthermore, the plots in the left column represent the density ratio in the entire computational domain, and the plots in the right column correspond to a magnified view of the density ratio distribution inside the cavities. Looking first to the plots in the left column, it is observed that, in general, the density ratio distribution follows that presented by the flat-plate case. Turning to the plots in the right column, it is noticed that the density ratio is low at the vicinity of the back-face corner, due to the flow expansion, and it is high at the frontal-face corner, because of the flow compression region. It is also observed that the density ρ is, at least, twice the freestream density ρ_∞ at the bottom surface of the cavities, for the L/H ratio investigated.

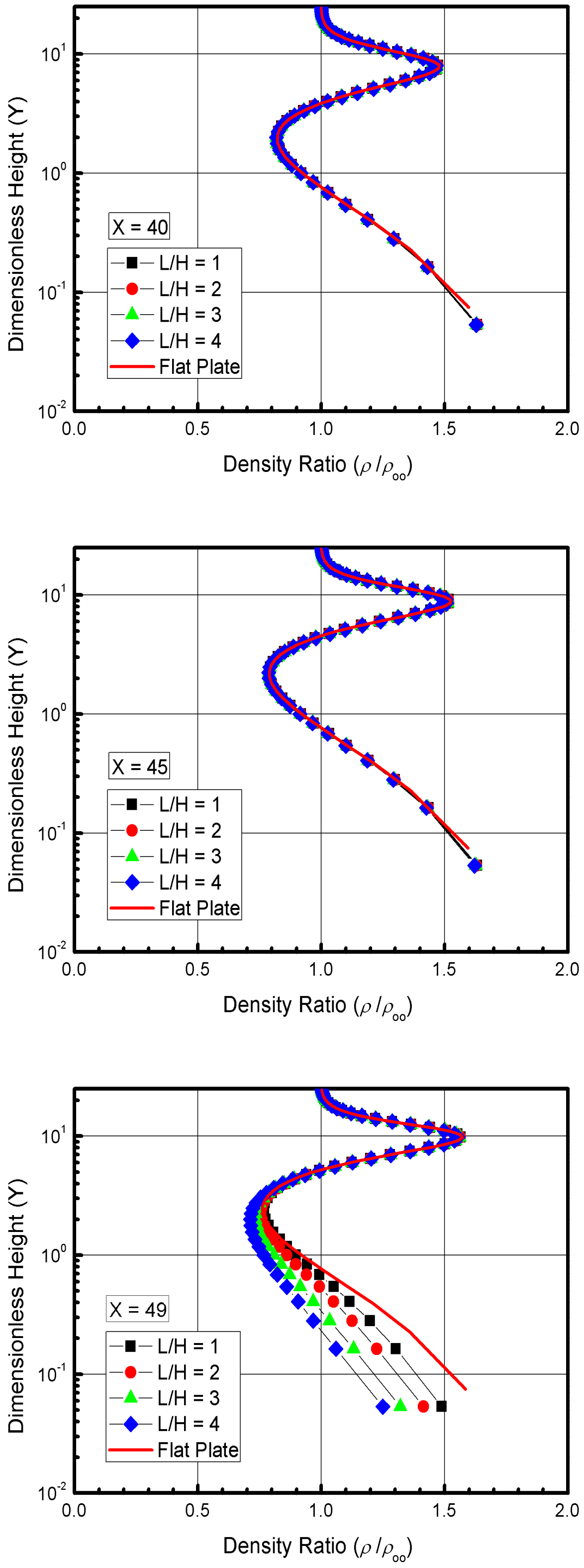

FIGURE 5.7 - Density ratio (ρ/ρ_∞) profiles for three sections along the cavity surface $S1$ parameterized by the L/H ratio.

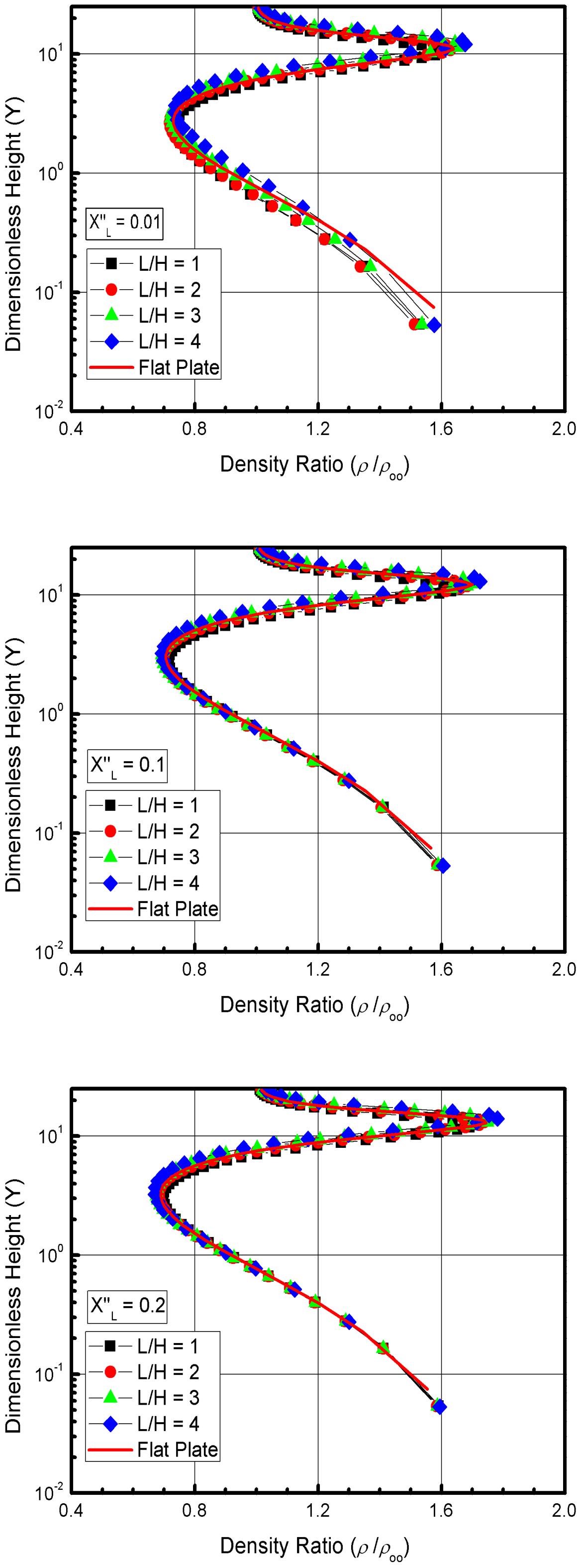

FIGURE 5.8 - Density ratio (ρ/ρ_∞) profiles for three sections along the cavity surface $S5$ parameterized by the L/H ratio.

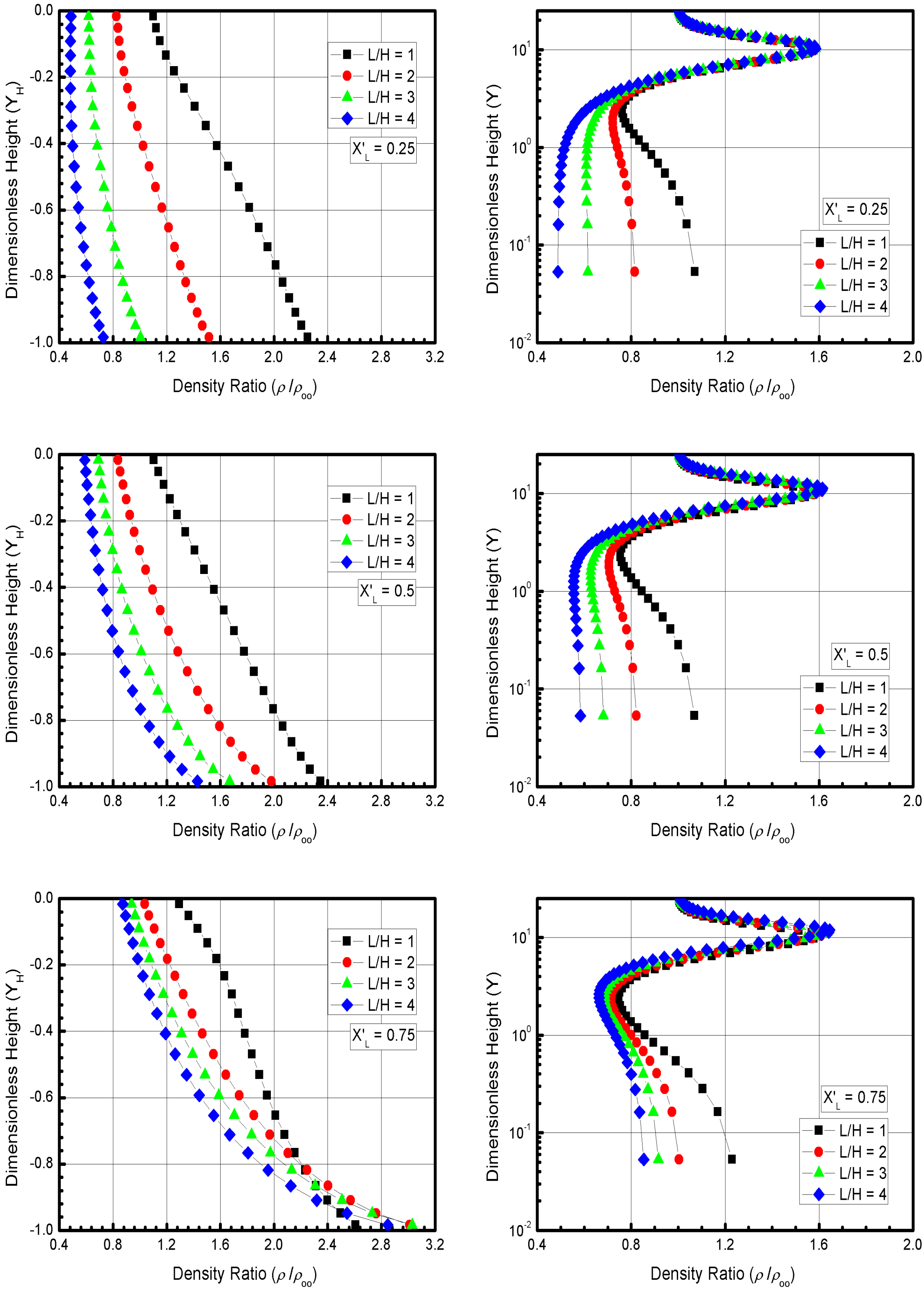

FIGURE 5.9 - Density ratio (ρ/ρ_∞) profiles for three sections along the cavity surface $S3$ parameterized by the L/H ratio.

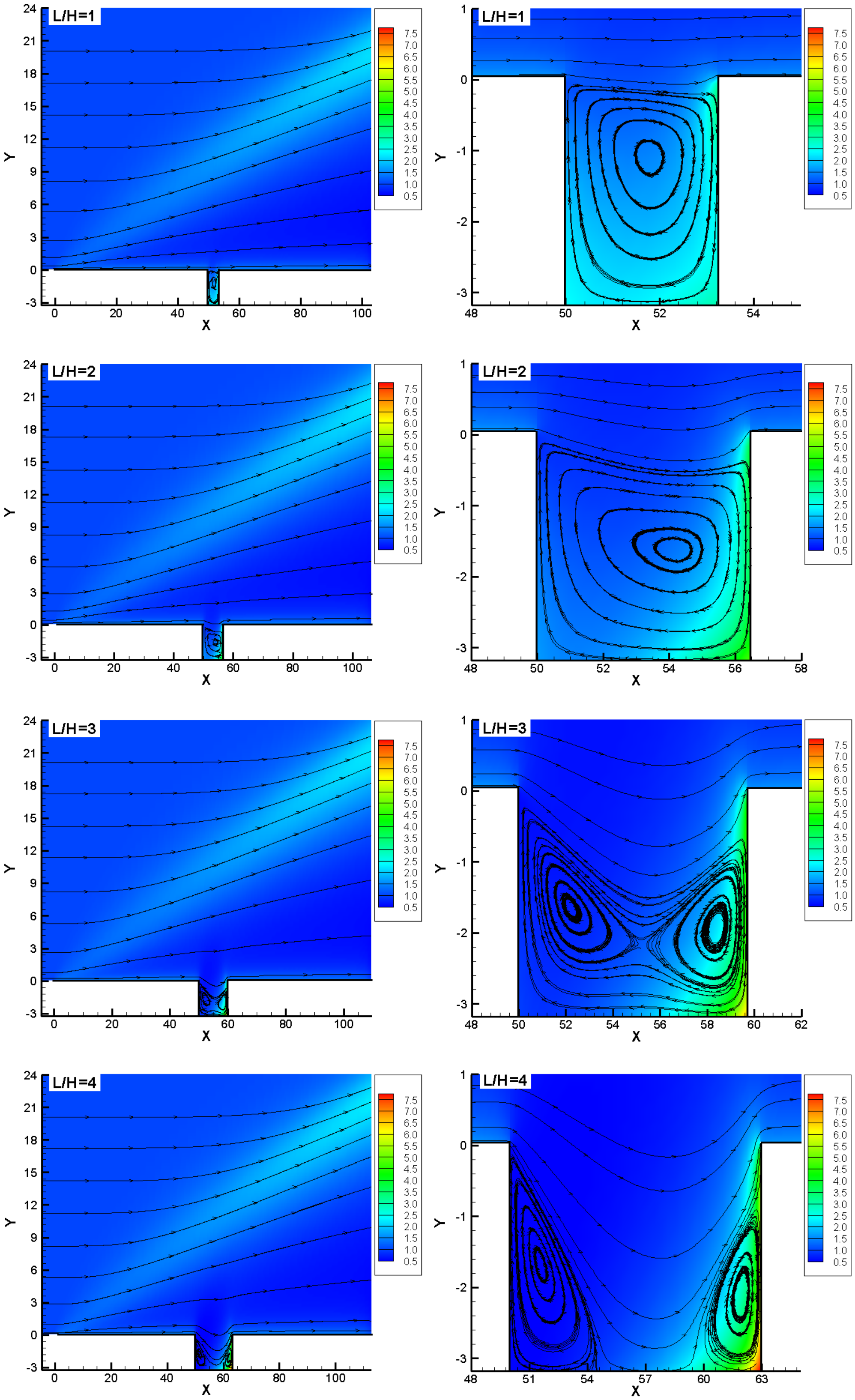

FIGURE 5.10 - Density ratio (ρ/ρ_∞) distribution outside (left) and inside (right) the cavities for L/H ratio of 1, 2, 3 and 4.

5.1.3 Pressure Field

The pressure in each cell in the computational domain is obtained by the following equation,

$$\overline{p} = \frac{1}{3V_c} \sum_{j=1}^{N} \frac{m\mathbf{c}'^2}{N} \tag{5.3}$$

where N is the number of molecules in the cell, m the mass of the molecules, V_c is the volume of the cell, and $\mathbf{c}'$ is the thermal velocity of the molecules.

The influence of the L/H ratio on pressure profiles along surface $S1$ is exhibited in Figure 5.11 for three sections. In this set of diagrams, pressure p is normalized by the freestream pressure p_∞, X and Y are dimensionless variables as defined previously in the density ratio profiles. Moreover, for comparative purpose, pressure ratio profiles for the flat-plate case are also exhibited in the same diagrams.

According to this set of diagrams, it is noticed that pressure ratio profiles follow a similar behavior as compared to those presented by density ratio profiles in the sense that they differ from those for the flat-plate case in a small region above the surface. In this small region, the pressure ratio for the L/H ratio investigated is lower than that for the flat-plate case. Beyond this small region, as $Y \to \infty$, the pressure ratio continues to increase to a maximum value inside the shock wave that formed at the sharp leading edge of the flat plate. After that, the pressure dramatically decreases, outside the shock wave, and reaches the freestream pressure value at the outer boundary of the computational domain.

Pressure ratio profiles for three sections along the cavity downstream surface, surface $S5$, are displayed in Figure 5.12, parameterized by the L/H ratio. Based on this set of plots, it is clearly seen that pressure ratio profiles follow a similar behavior as compared to those presented along the cavity upstream surface, surface $S1$. They differ from those for the flat-plate case in a small region above the surface at the vicinity of the cavity corner. In this small region, the pressure ratio for the L/H ratio investigated is larger than that for the flat-plate case. This behavior is in contrast to that observed in the cavity upstream surface, surface $S1$. This is explained by the fact that, at the vicinity of the back-face corner, the flow experiences an expansion. On the other hand, at the vicinity of the frontal-face corner, the flow experiences a compression.

Effects of the L/H ratio on pressure ratio profiles along surface $S3$ are demonstrated in Figure 5.13 for three sections defined by X_L' of 0.25, 0.50, and 0.75. In this family of plots, the left-column plots correspond to p/p_∞ inside the cavity and right-column plots to the profiles outside the cavity. Looking first to the left-column plots, it is very encouraging to observe that the pressure ratio inside the cavities decreases from the top to the bottom of the cavities for the L/H ratio investigated. In addition, at the bottom of the cavities, the pressure p is basically one order of magnitude larger than the freestream pressure p_∞. Turning to the right-column plots, at section X_L' = 0.25 and $Y = 0$, it is seen that the pressure ratio increases with decreasing the L/H ratio. Conversely, at section $X_L' = 0.75$ and $Y = 0$, the pressure ratio increases with increasing the L/H ratio.

In the following, it is desirable to present contour maps for the pressure ratio in the entire computational domain. In this fashion, Figure 5.14 depicts the pressure ratio distribution in the entire computational domain (left column) as well as a magnified view of the pressure ratio inside the cavities (right column). In this set of plots, dimensionless height and length, Y and X, respectively, are similar to those defined previously in the density ratio contours.

According to this set of plots, at the vicinity of the sharp leading edge of the flat plate, pressure is almost two orders of magnitude larger than the freestream pressure. The reason for that is because of the large amount of kinetic energy present in a hypersonic freestream. This energy is converted by molecular collisions into high thermal energy surrounding the body and by flow work into increased pressure. Inside the cavities, it is observed that the maximum pressure ratio takes place at the frontal-face corner, i.e., pressure p is fifty times the freestream pressure p_∞. It should be remarked that this pressure ratio is almost twice the maximum pressure ratio observed at the bottom of the cavities, for the L/H ratio investigated. As a result, it may be inferred in passing that particular attention should be paid to the cavity frontal face in terms of the pressure loads, since the vicinity of the corner represents a zone of strong compression.

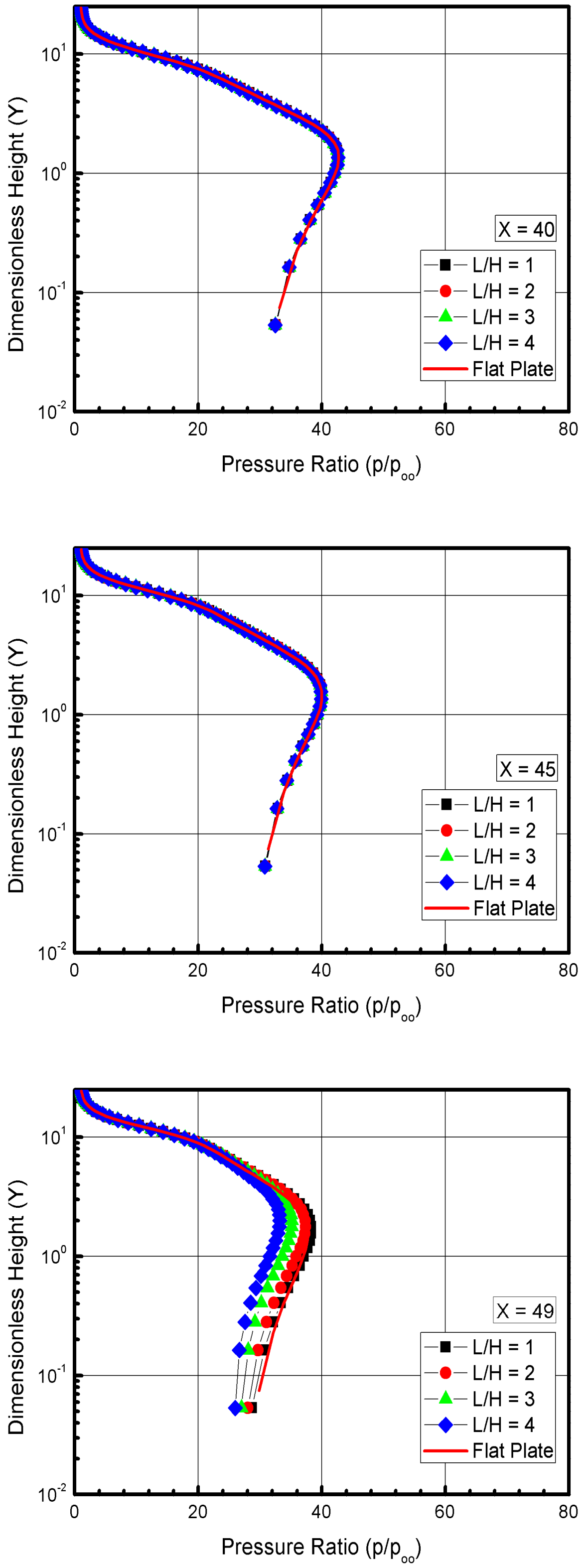

FIGURE 5.11 - Pressure ratio (p/p_∞) profiles for three sections along the cavity surface $S1$ parameterized by the L/H ratio.

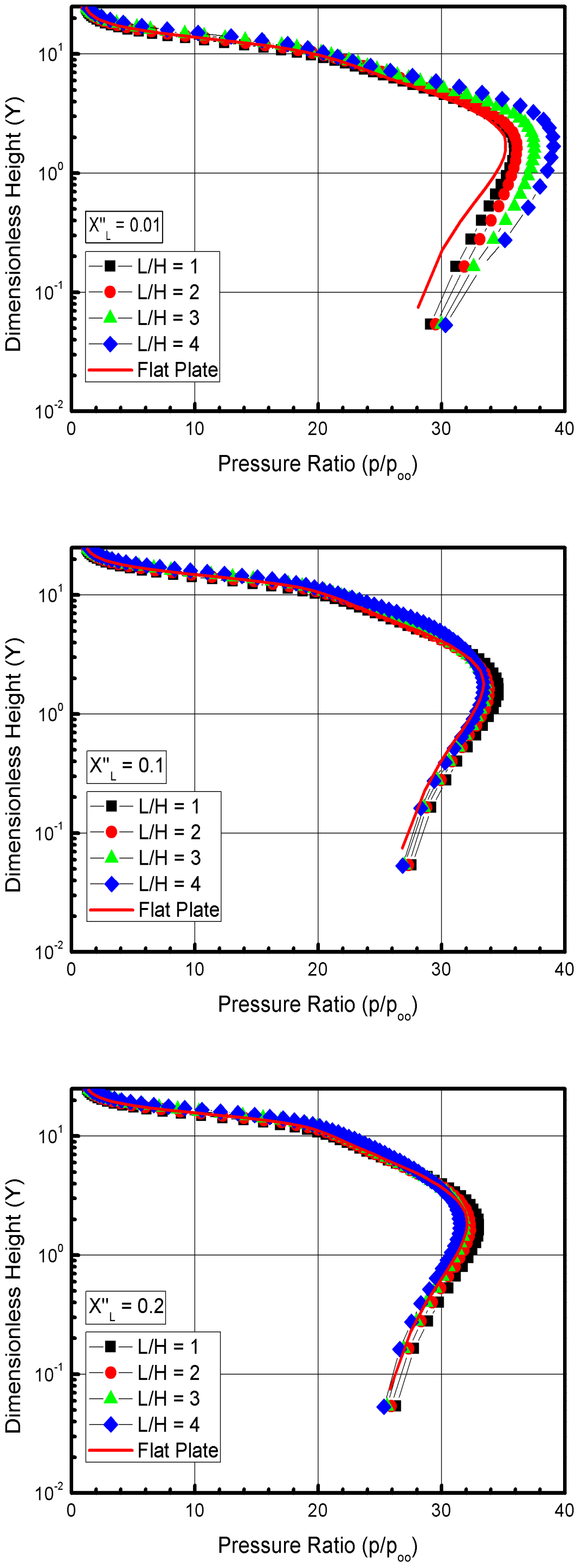

FIGURE 5.12 - Pressure ratio (p/p_∞) profiles for three sections along the cavity surface $S5$ parameterized by the L/H ratio.

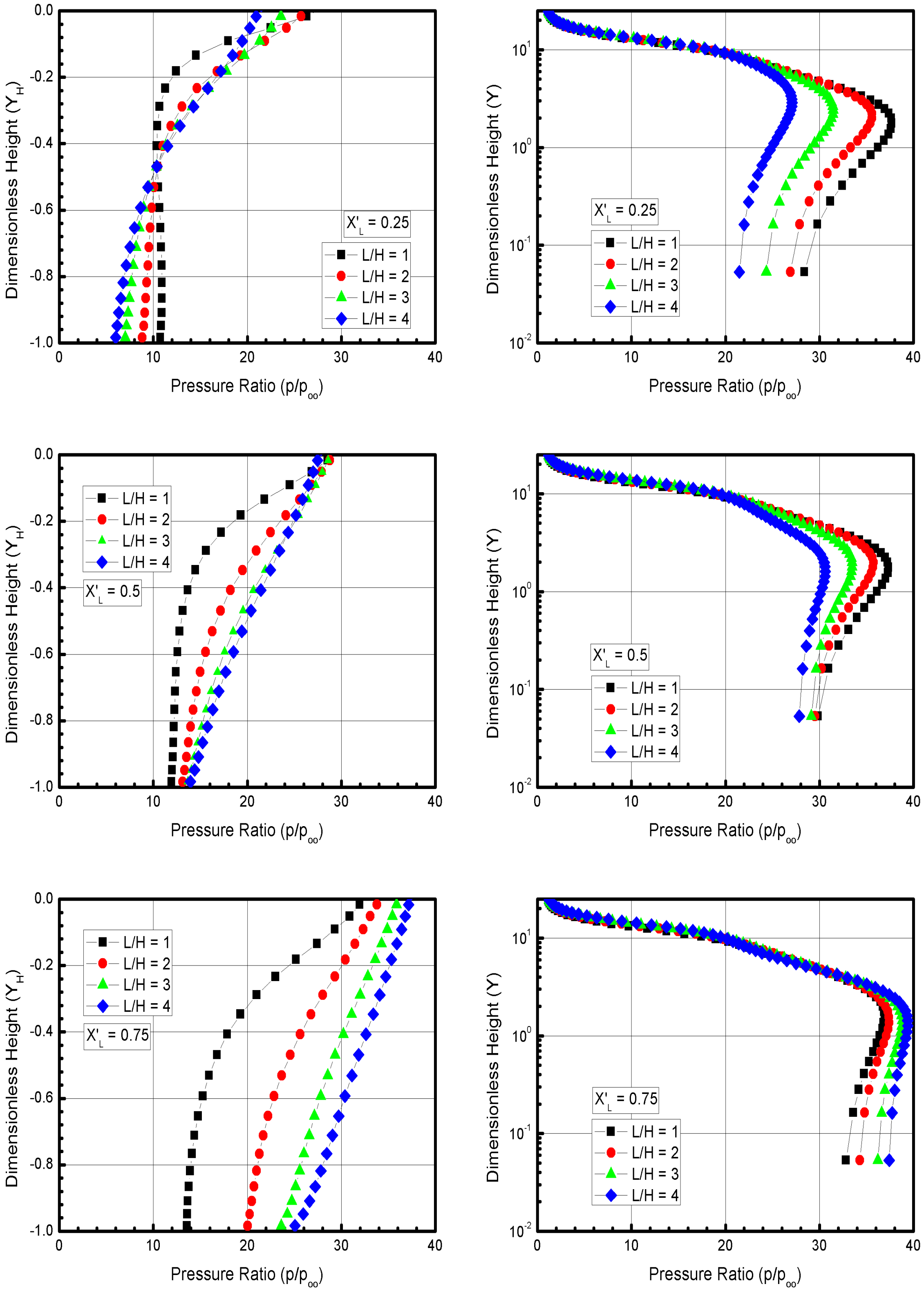

FIGURE 5.13 - Pressure ratio (p/p_∞) profiles for three sections along the cavity surface $S3$ parameterized by the L/H ratio.

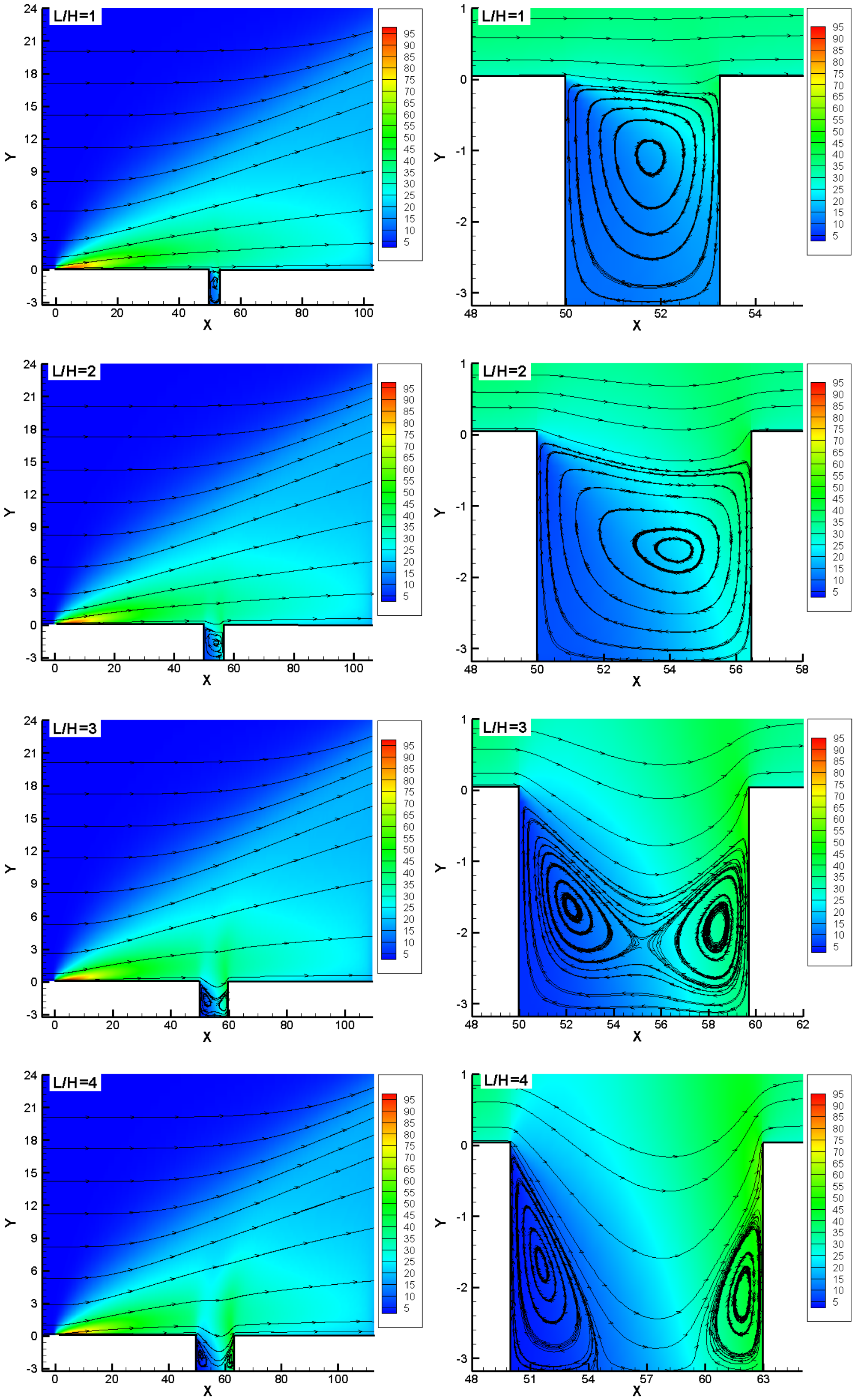

FIGURE 5.14 - Pressure ratio (p/p_∞) distribution outside (left) and inside (right) the cavities for L/H ratio of 1, 2, 3 and 4.

5.1.4 Kinetic Temperature Field

In a monoatomic gas, the translational temperature, related to the translational kinetic energy of molecules, is simply defined as temperature. In a diatomic or polyatomic gas, molecules have internal energy associated to the internal modes of rotation and vibration. In addition, for a gas in thermodynamic equilibrium, the translational temperature is equal to the temperature related to the internal modes, i.e., rotational and vibrational temperatures, and it is identified as thermodynamic temperature. Conversely, in a thermodynamic non-equilibrium gas, an overall temperature is defined as the weighted mean of the translational and internal temperatures (BIRD, 1994) as being,

$$T_{OV} = \frac{\zeta_T T_T + \zeta_R T_R + \zeta_V T_V}{\zeta_T + \zeta_R + \zeta_V} \tag{5.4}$$

where T and ζ stand for the temperature and the degree of freedom, respectively. The subscripts T, R and V refer to the translation, rotation and vibration, respectively.

Translational, rotational and vibrational temperatures are obtained for each cell in the computational domain through the following equations,

$$\overline{T}_T = \frac{1}{3\kappa} \sum_{j=1}^{N} \frac{(m\mathbf{c}'^2)_j}{N} \tag{5.5}$$

$$\overline{T}_R = \frac{2}{\kappa} \frac{\overline{\varepsilon}_R}{\zeta_R} \tag{5.6}$$

$$\overline{T}_V = \frac{\Theta_V}{\ln\left(1 + \frac{\kappa\Theta_V}{\overline{\varepsilon}_V}\right)} \tag{5.7}$$

where κ is the Boltzmann constant, Θ_V is the characteristic temperature of vibration, $\overline{\varepsilon}_R$ and $\overline{\varepsilon}_V$ are, respectively, rotational and vibrational average energies in each cell.

The L/H ratio effects on temperature profiles along surface $S1$ are exhibited in Figure 5.15 for three sections. In this set of plots, kinetic temperature ratio stands for the translational temperature T_T, rotational temperature T_R, vibrational temperature T_V, and overall temperature T_{OV} normalized by the freestream temperature T_∞, X'_L and Y are dimensionless variables as defined previously in the pressure ratio profiles. Furthermore, empty and filled symbols refer to profiles for L/H of 1 and 4, respectively. Results for L/H of 2 and 3 are intermediate and will not be shown.

Referring to Figure 5.15, it is clearly seen that thermodynamic non-equilibrium occurs outside the cavities, as shown by the lack of equilibrium between the translational and internal kinetic temperatures. As mentioned earlier, thermal non-equilibrium occurs when the temperatures associated with the translational, rotational, and vibrational modes of a polyatomic gas are different. It should be mentioned in this context that the overall temperature, defined by Equation 5.4, is equivalent to the thermodynamic temperature only under thermal equilibrium conditions. In addition, the ideal gas equation of state does not apply to this temperature in a non-equilibrium situation.

Still referring to Figure 5.15, it should be recognized that, in the undisturbed freestream far from the surface $S1$, $Y \to \infty$, the translational and internal kinetic temperatures have the same value and are equal to the thermodynamic temperature. Approaching the surface $S1$, say $Y \approx 2$, the translational kinetic temperature rises to well above the rotational and vibrational temperatures and reaches a maximum value that is a function of the section X. Since a large number of collisions is needed to excite molecules vibrationally from the ground state to the upper state, the vibrational temperature is seen to increase much more slowly than rotational temperature. Still further toward the surface $S1$, $Y \approx 0$, the translational, rotational, vibrational, and overall kinetic temperatures decrease, and reach a value on the wall that is above the wall temperature T_w ($\approx 4T_\infty$), resulting in a temperature jump as defined in continuum formulation (GRUPTA et al., 1985). Furthermore, the difference between translational temperature and internal temperatures at the vicinity of the surface $S1$ also indicates that the thermodynamic equilibrium is not achieved in the boundary layer. Moreover, it should be emphasized that no visible changes are observed in the temperature ratio profiles due to variations on the L/H ratio, since L/H of 1 and 4 represent, respectively, the largest and the smallest values investigated.

Proceeding in a manner analogous to the aforementioned analysis for the temperature ratio profiles, Figure 5.16 reveals that the essential features for the temperature ratio profiles, observed along the cavity upstream surface, also take place along the cavity downstream surface, i.e., surface $S5$. Temperature ratio profiles on both surfaces are similar at least in two major respects: (1) thermodynamic equilibrium is not achieved in the boundary layer, and (2) no significant effects are observed in the temperature ratio profiles due to changes on the L/H ratio.

In the results that follow, Figure 5.17 demonstrates the temperature ratio profiles for three sections along surface $S3$ defined by X'_L of 0.25, 0.50, and 0.75. Again, in this set of plots, the left-column plots correspond to T/T_∞ inside the cavity and right-column plots to the profiles outside the cavity. Also, empty and filled symbols stand for L/H of 1 and 4, respectively. Results for L/H of 2 and 3 are intermediate and will not be shown.

According to this set of plots, for the $L/H = 1$ case, it is seen that the kinetic temperature ratio T/T_∞ decreases and basically reaches a constant value on the bottom surface, which corresponds to the wall temperature T_w ($\approx 4T_\infty$). For this particular case, it is also seen that the flow is in thermal equilibrium, once the internal temperatures are basically equal to the translational temperature at the bottommost portion of the cavity. It is important to recall that, the density increased at the vicinity of the cavity bottom surface, as shown in Figures 5.9 and 5.10. Consequently, the local mean free path decreased and the mean collision frequency increased and, therefore, the flow tended to the thermal equilibrium. In contrast, for the $L/H = 4$ case, thermal equilibrium is not achieved, even though the temperature ratio decreases significantly from the top to the bottom of the cavity.

In what follows, it is important to exhibit contour maps for the translational temperature ratio in the entire computational domain. In this sense, Figure 5.18 illustrates the translational temperature ratio distribution in the entire computational domain (left column) as well as a magnified view of the translational temperature ratio inside the cavities (right column). In this family of plots, dimensionless height Y and length X are similar to those defined in the pressure ratio contours.

According to Figure 5.18, it is observed that, at the vicinity of the sharp leading edge of the flat plate, translational temperature is around fifty times the freestream temperature. As explained earlier, the large amount of kinetic energy present in a hypersonic freestream is converted by molecular collisions into high thermal energy surrounding the body.

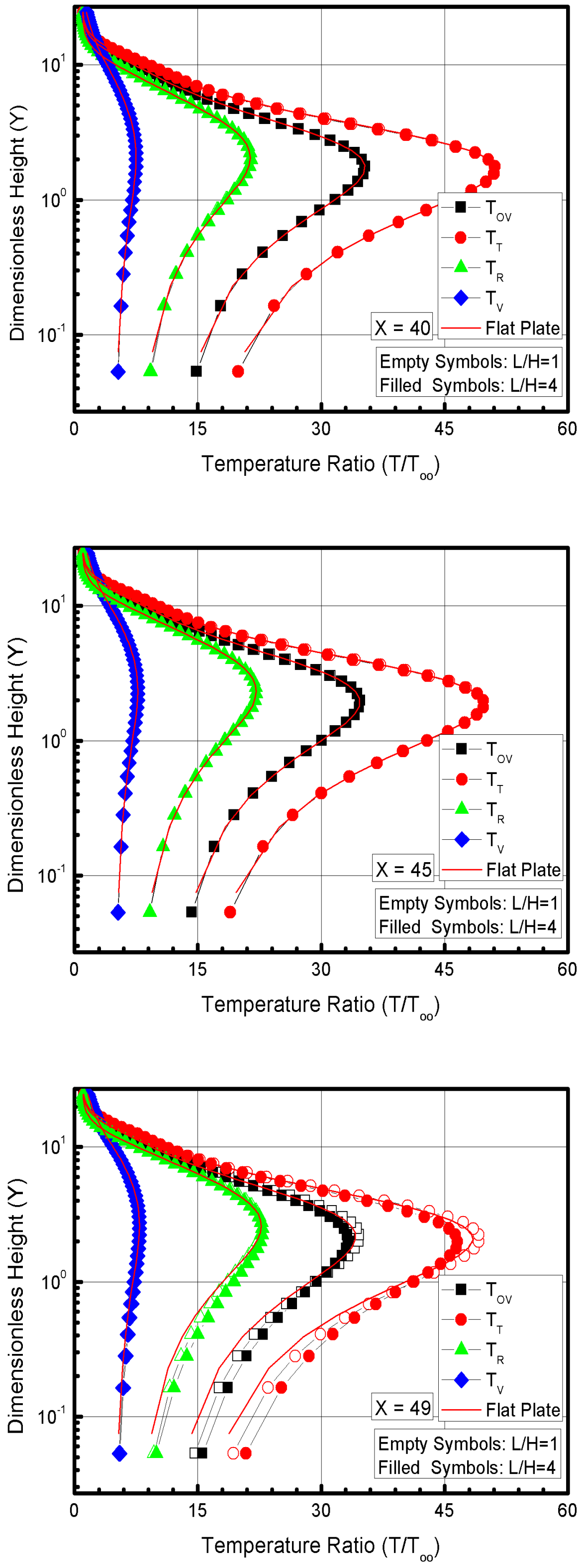

FIGURE 5.15 - Kinetic temperature ratio (T/T_∞) profiles for three sections along the cavity surface $S1$ parameterized by the L/H ratio.

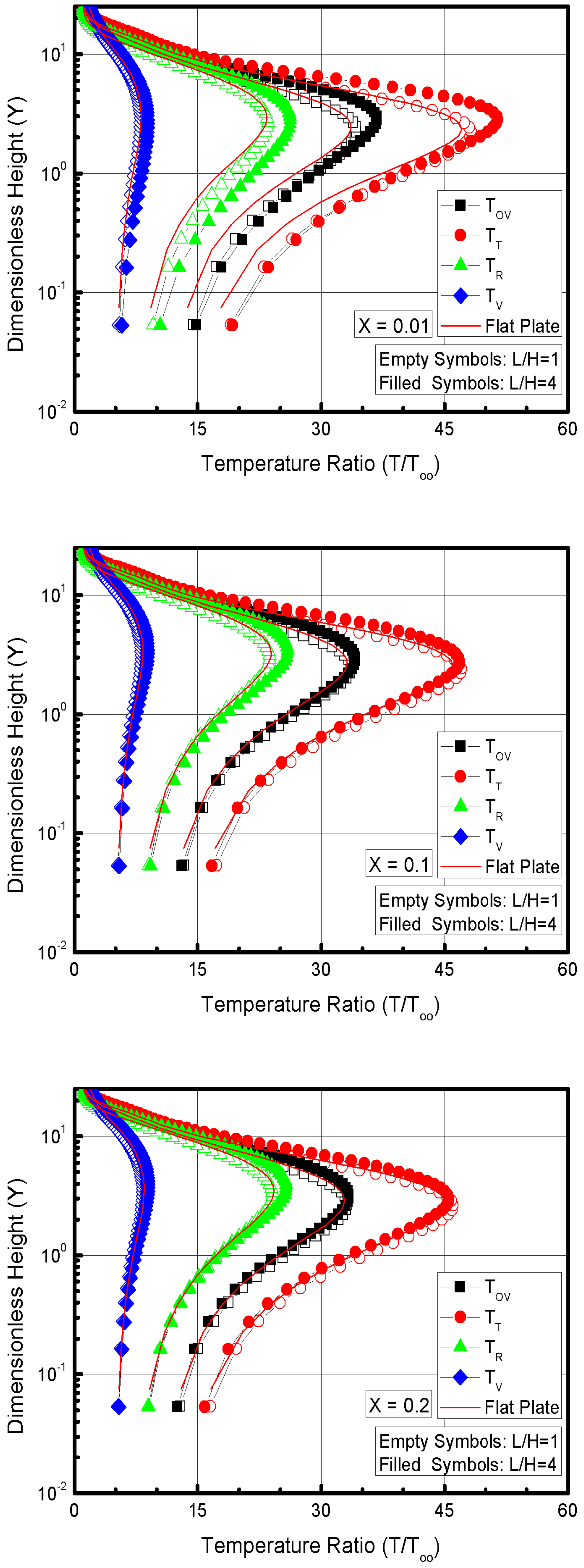

FIGURE 5.16 - Kinetic temperature ratio (T/T_{∞}) profiles for three sections along the cavity surface $S5$ parameterized by the L/H ratio.

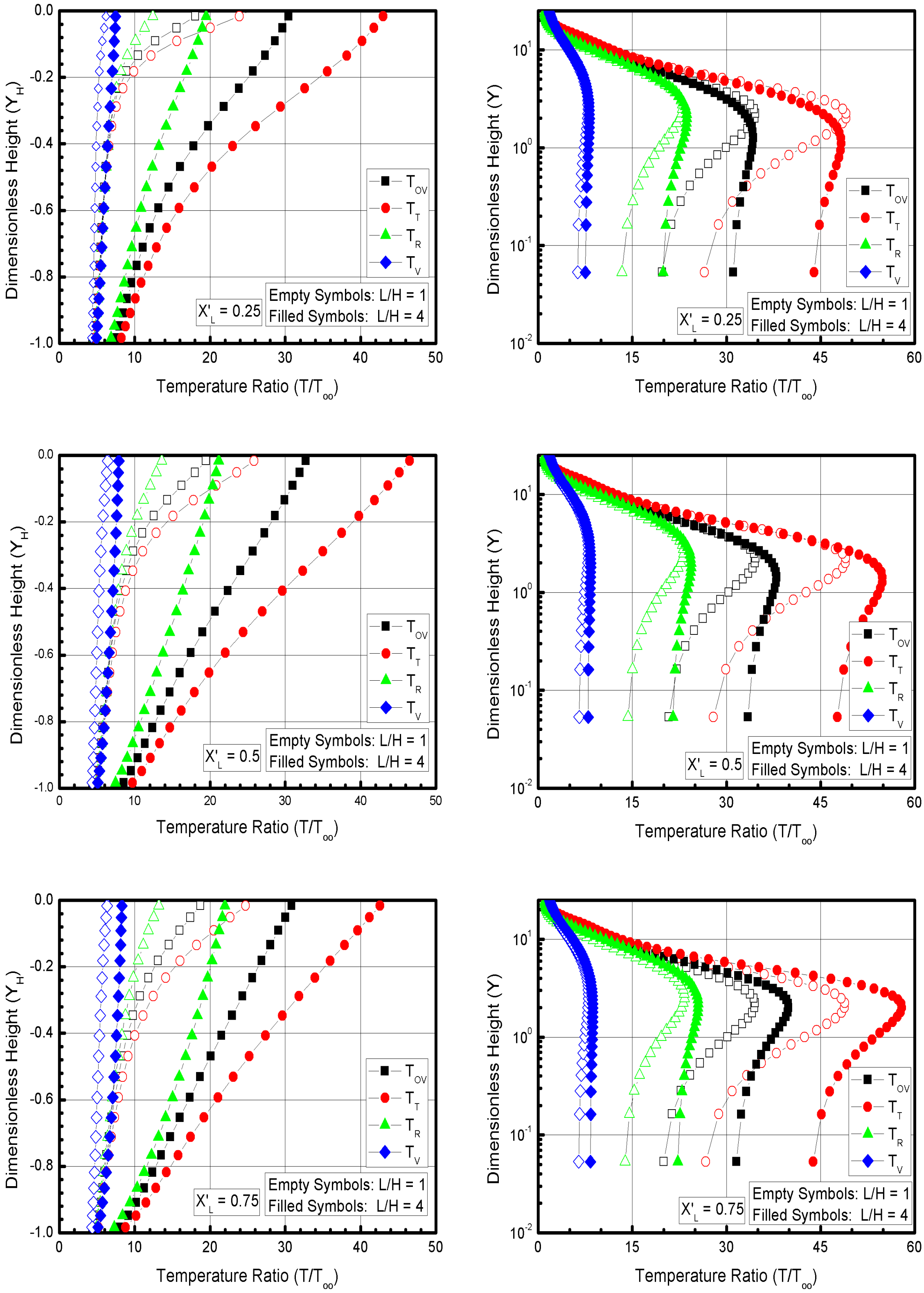

FIGURE 5.17 - Kinetic temperature ratio (T/T_∞) profiles for three sections along the cavity surface $S3$ parameterized by the L/H ratio.

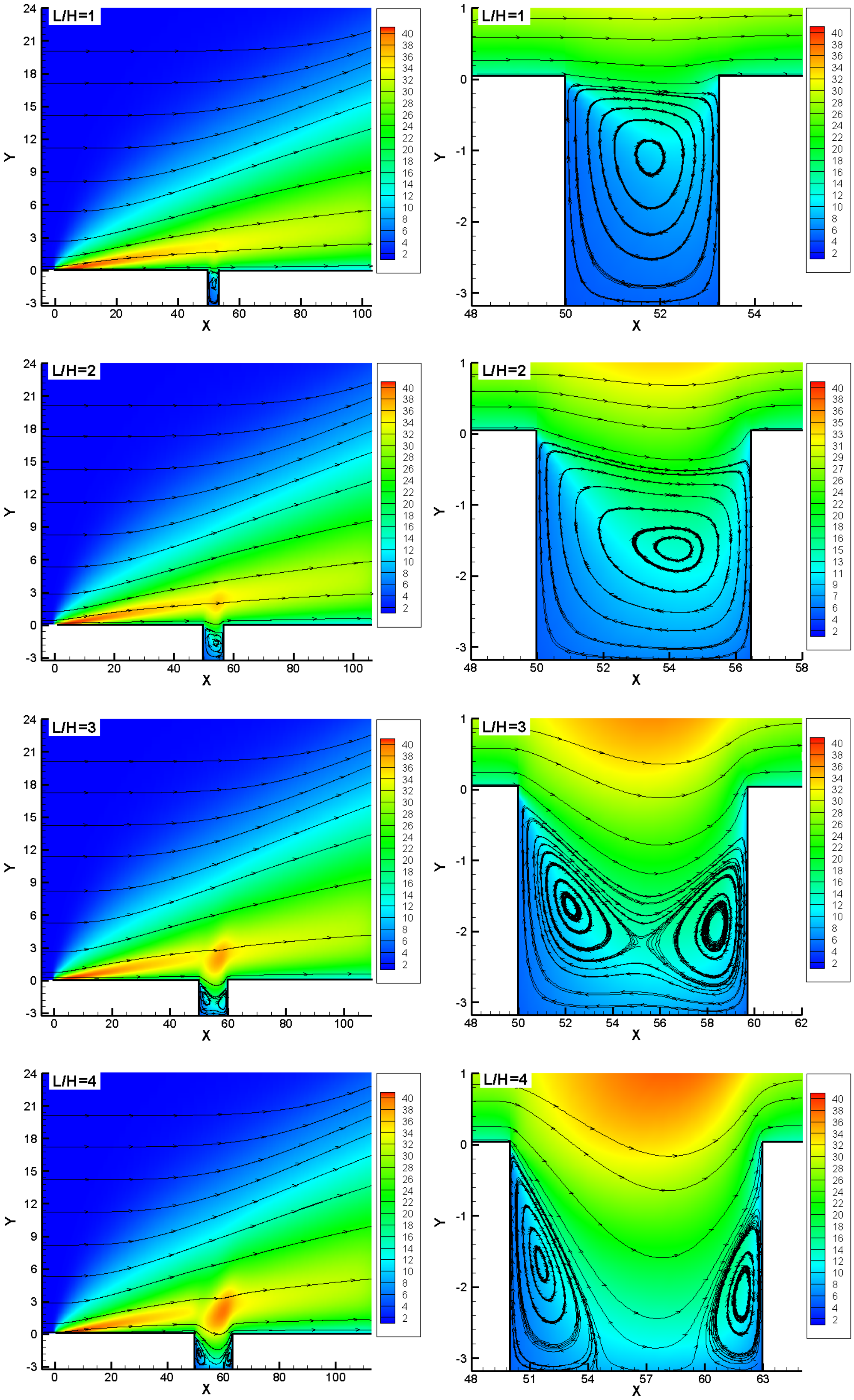

FIGURE 5.18 - Translational temperature ratio (T_T/T_∞) distribution outside (left) and inside (right) the cavities for L/H ratio of 1, 2, 3 and 4.

5.2 Aerodynamic Surface Quantities

Aerodynamic surface quantities of particular interest in the transition flow regime are number flux, heat transfer, pressure, and skin friction. In this sense, the purpose of this section is to present and to discuss the behavior of these quantities, expressed in coefficient form, due to variations on the cavity L/H ratio.

5.2.1 Number Flux

The number flux N is calculated by sampling the molecules impinging on the cavity surface by unit time and area. Effects of the L/H ratio on the number flux are illustrated in Figure 5.19. In this group of plots, N_f represents the number flux N normalized by $n_\infty U_\infty$, where n_∞ is the freestream number density and U_∞ is the freestream velocity. The left-column plots refer to the number flux distribution along the cavity upstream and downstream surfaces, i.e., surfaces $S1$ and $S5$, while the right-column plots stand for the distribution on the surfaces inside the cavity, i.e., surfaces $S2$, $S3$, and $S4$. In addition, X is the length x normalized by the freestream mean free path λ_∞, X'_L is the length $(x - L_u - L)$ normalized by the cavity length L, Y_H refers to the height y normalized by the cavity height H. Also, for the comparison purpose, the number flux distribution for the flat-plate case is illustrated in this group of plots.

Looking first to the left-column plots in Figure 5.19, it is seen that the dimensionless number flux N_f to the surfaces basically does not depend on the L/H ratio, for the conditions investigated. From the leading edge up to a station close to the cavity location ($X = 50$), the number flux behavior for the cavities is similar to that for the flat-plate case, i.e., a plate without a cavity. This is an expected behavior in the sense that this region is not affected by the presence of the cavities. However, close to the upstream cavity corner, i.e., the surface-$S1$/surface-$S2$ junction, there is a decrease in the number flux due to the flow expansion around the upstream corner. A magnified view of this behavior is shown in detail in the middle plot. Along the surface $S5$, it is seen that the dimensionless number flux N_f behavior is similar to that for the flat-plate case, except at the vicinity of the downstream corner, i.e., the surface-$S4$/surface-$S5$ junction. It should be remarked that the total length of the flat plate is equal to the largest cavity, i.e., the $L/H = 4$ case. It should be also mentioned that the significant number-flux drop at the end of the curves is due to the vacuum condition assumed to the downstream outflow boundary, side IV, in the computational domain.

Turning next to the right-column plots in Figure 5.19, it is clearly noticed that the number flux N_f to the surfaces $S2$, $S3$ and $S4$ depends on the cavity L/H ratio. Along the back face, surface $S2$, the dimensionless number flux is low at the top of the cavity, and increases monotonically along the surface up to the corner at the bottom surface. Conversely, for the frontal face, surface $S4$, the dimensionless number flux depends on the L/H ratio. For the $L/H = 1$ case, the number flux is high at the corner of the cavity, $Y_H = 0$, and decreases to a minimum value at the bottom surface. For the $L/H > 1$ cases, the number flux N_f basically starts increasing at the corner, $Y_H = 0$, slightly decreases up to the station $Y_H \simeq -0.7$, and increases again along the surface up to the corner at the bottom surface. Along the cavity bottom surface, surface $S3$, the dimensionless number flux behavior also depends on L/H ratio. It basically increases from one corner to another with increasing the L/H ratio.

Still referring to right-column plots, it may be recognized that, in general, the dimensionless number flux N_f along the frontal face, surface $S4$, is one order of magnitude larger than that along the back face, surface $S2$. An understanding of this behavior can be gained by considering the flow structure inside the cavities, as shown in Figure 5.5. Due to the clockwise recirculation region inside the cavities, density is low at the vicinity of the back face. In contrast, density is high at the vicinity of the frontal face, since the flow experiences a compression. Consequently, the number flux behavior is different along the two surfaces.

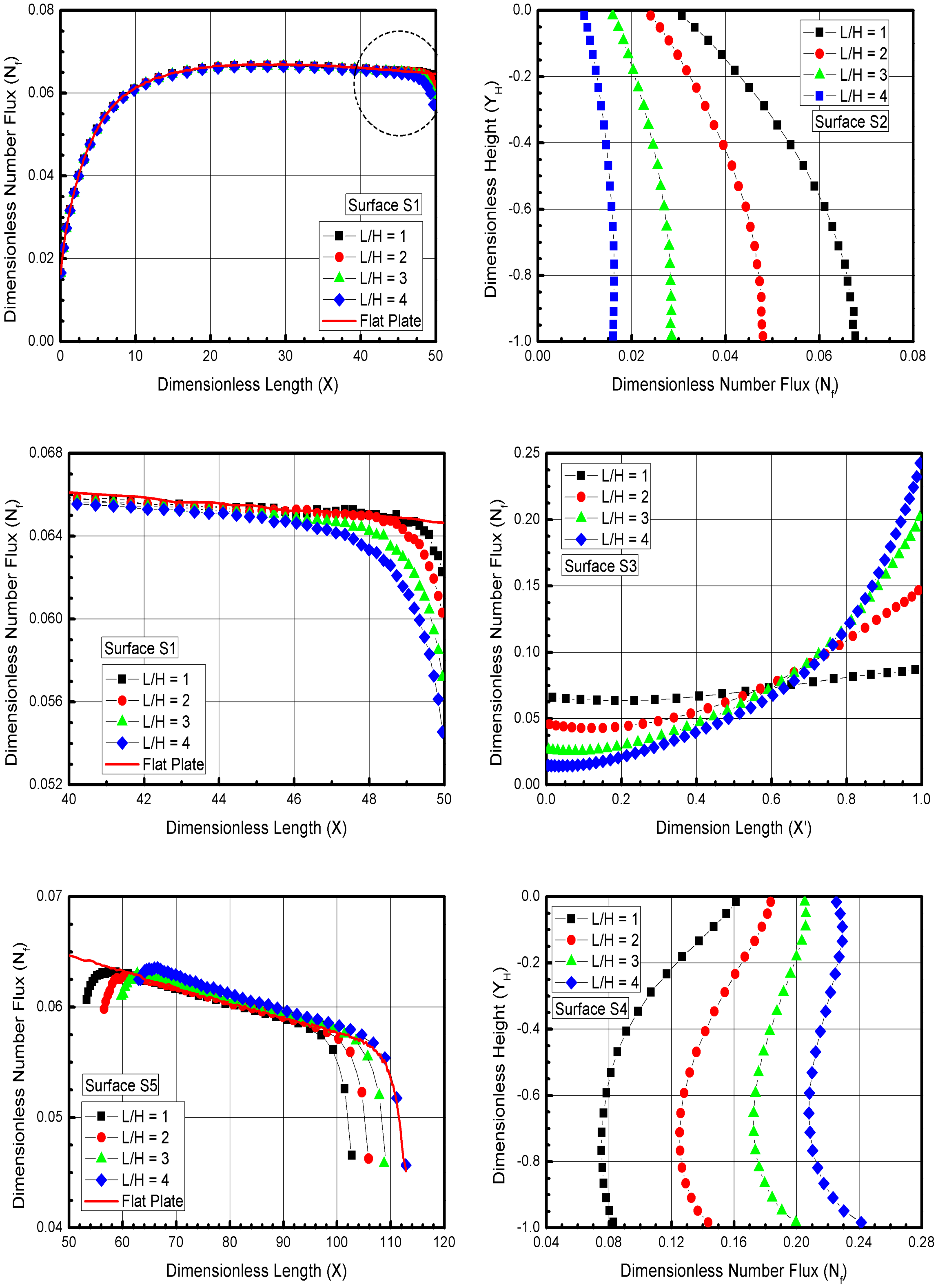

FIGURE 5.19 - Dimensionless number flux N_f distribution along the cavity surfaces as a function of the L/H ratio.

5.2.2 Heat Transfer Coefficient

The heat transfer coefficient is defined as follows,

$$C_h = \frac{q_w}{1/2\rho_\infty U_\infty^3} \tag{5.8}$$

where the heat flux q_w to the cavity surface is calculated by the net energy flux of the molecules impinging on the surface.

A flux is regarded as positive if it is directed toward the cavity surface. In this fashion, the net heat flux q_w is related to the sum of the translational, rotational and vibrational energies of both incident and reflected molecules as defined by,

$$q_w = q_i + q_r = \frac{1}{A\Delta t}\sum_{j=1}^{N}\left[\frac{1}{2}m_j c_j^2 + e_{Rj} + e_{Vj}\right]_i + \left[\frac{1}{2}m_j c_j^2 + e_{Rj} + e_{Vj}\right]_r \tag{5.9}$$

where N is the number of molecules colliding with the cavity surface by unit time and unit area, m is the mass of molecules, c is the velocity of the molecules, e_R and e_V stand for the rotational and vibrational energies, respectively. Subscripts i and r refer to incident and reflect molecules.

The dependence of the heat transfer coefficient C_h on the L/H ratio is demonstrated in Figure 5.20. Again, the left-column plots refer to the heat transfer distribution along the cavity surfaces $S1$ and $S5$, while the right-column plots stand for the distribution on the cavity surfaces $S2$, $S3$, and $S4$. As a basis of comparison, the heat transfer coefficient distribution for the flat-plate case is also illustrated in this figure.

On examining first the left-column plots, it is noticed that no appreciable changes are observed in the heat transfer coefficient C_h along the surface $S1$ due to the L/H ratio rise. Similar to the dimensionless number flux, it is seen that the heat transfer coefficient along the surface $S1$ exhibits the same behavior for the flat-plate case, from the leading edge up to near the upstream corner of the cavities. For the range of L/H investigated, C_h is low at the leading edge, increases to a peak value, $C_h = 0.0285$ at section $X = 8.82$, and then decreases downstream up to the cavity upstream corner, i.e., surface-$S1$/surface-$S2$ junction. Particular attention is paid to the upstream disturbance due to the presence of the cavities. It is observed that the extension of the upstream disturbance in the heat transfer coefficient is much less than that observed for the number flux. This behavior is elucidated in the magnified view presented in the middle plot. Along the surface $S5$, it is observed that the heat transfer coefficient C_h is larger than that for the flat-plate case, especially at the vicinity of the downstream corner of the cavities, defined by the surface-$S4$/surface-$S5$ junction. Nevertheless, as the flow moves downstream along the surface $S5$, the heat transfer coefficient C_h basically recovers the value obtained for the flat-plate case.

Turning next to the right-column plots, for surface $S2$, the heat transfer coefficient C_h is low at the cavity corner, $Y_H = 0$, and increases to a maximum value close to the station $Y_H \approx -0.4$. Afterwards, C_h decreases along the surface up to the corner at the bottom surface. Along the cavity floor, surface $S3$, the heat transfer coefficient depends on the L/H ratio. C_h roughly increases from zero, at station $X'_L = 0$, and reaches a maximum value around station $X'_L = 0.85$. In addition, the larger the L/H ratio is the larger the maximum value attained by the heat transfer coefficient C_h. After that, C_h drops off up to the surface-$S3$/surface-$S4$ junction. For surface $S4$, the heat transfer coefficient C_h is high at the top of the cavity, and monotonically decreases along the surface, reaching very low values at the corner. It is also very encouraging to observe that the peak values for the heat transfer coefficient C_h on the back face is one order of magnitude larger than that for the the frontal face. One possible reason for that is because, at the vicinity of the back face, the flow experiences an expansion. In contrast, at the vicinity of the frontal face, it experiences a compression due to the flow topology inside the cavity.

Before proceeding with the analysis, it is noteworthy that the heat flux to the cavity surfaces was defined in terms of the incident and reflected flow properties, Equation 5.9, and based upon the gas-surface interaction model of fully accommodated, complete diffuse reemission. The diffuse model assumes that the molecules are reflected equally in all directions, quite independently of their incident speed and direction. Due to the diffuse reflection model, the reflected velocity of the molecules impinging on the cavity surfaces is obtained from a Maxwellian distribution that takes into account for the temperature of the cavity surfaces. In this manner, according to Equation 5.9, not only the number of molecules impinging on the surface but also the wall temperature plays a important role on the reflected contribution to the net heat flux to the cavity surfaces.

At this point it is worth taking a closer look at the heat transfer coefficient results. In order to do that, the peak values for the heat transfer coefficient C_h, approximately 0.049, 0.056, 0.060, and 0.064 for the L/H ratio of 1, 2, 3, and 4, respectively, at the cavity corner of surface $S4$, are compared to that predicted for a smooth surface, i.e., a flat plate without a cavity. For the flat-plate case, the maximum value for C_h is around to 0.0285 at a station $8.82\lambda_\infty$ from the leading edge of surface S1. Therefore, the C_h peak value for the cavities is more than twice of that for a smooth surface.

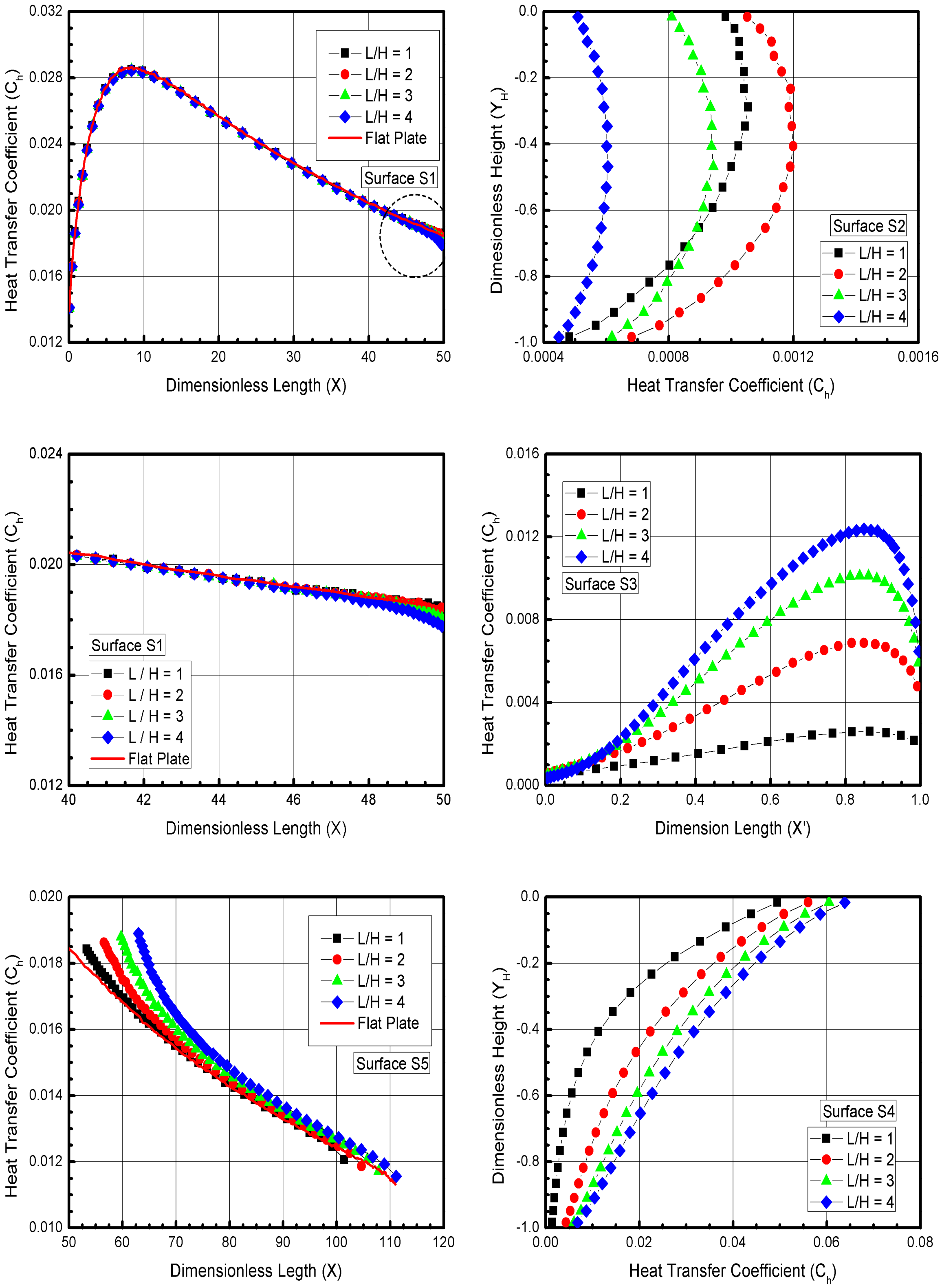

FIGURE 5.20 - Heat transfer coefficient C_h distribution along the cavity surfaces as a function of the L/H ratio.

5.2.3 Coefficient of Pressure

The pressure coefficient C_p is defined as follows,

$$C_p = \frac{p_w - p_\infty}{1/2\rho_\infty U_\infty^2} \tag{5.10}$$

where the pressure p_w on the cavity surface is calculated by the sum of the normal momentum fluxes of both incident and reflected molecules at each time step as follows,

$$p_w = p_i + p_r = \frac{1}{A\Delta t}\sum_{j=1}^{N}[m_j v_j]_i + [m_j v_j]_r \tag{5.11}$$

where v is the velocity component of the molecule j in the surface normal direction.

The effect on the pressure coefficient C_p due to variation in the L/H ratio is depicted in Figure 5.21. Again, the left-column plots correspond to the pressure coefficient distribution along the cavity surfaces $S1$ and $S5$, while the right-column plots stand for the distribution on the cavity surfaces $S2$, $S3$, and $S4$. Referring to the left-column plots, it is clearly noticed that the pressure coefficient C_p follows the same trend as that presented for the dimensionless number flux in the sense that, along the surface S1, the pressure coefficient presents the same behavior for the flat-plate case. From the leading edge up to a station close to the cavity location ($X = 50$), the pressure coefficient behavior for the cavities is similar to that for the flat-plate case. Again, close to the upstream cavity corner, i.e., the surface-$S1$/surface-$S2$ junction, a significant reduction in the pressure coefficient C_p is observed when compared to the pressure coefficient of the flat-plate case. As mentioned earlier, the reason for that is due to the flow expansion around the upstream corner. This behavior is shown in detail in a magnified view, the middle plot. Along the surface $S5$, it is observed that the pressure coefficient C_p behavior is similar to that for the flat-plate case, except at the vicinity of the downstream corner, i.e., the surface-$S4$/surface-$S5$ junction.

Turning to the right-column plots, it is seen that the pressure coefficient C_p roughly follows a similar behavior as that presented by the number flux in that, for the back face, surface $S2$, it is low at the corner, $Y_H = 0$, and increases downward along the surface, reaching the maximum value at the bottom, station $Y_H = -1.0$. In what follows, for the cavity floor, surface $S3$, the pressure coefficient C_p increases along the entire surface, and reaches the maximum value at the vicinity of the surface-$S3$/surface-$S4$ junction. Finally, along the frontal face, surface $S4$, the pressure coefficient C_p behavior is in contrast to that observed along the surface $S2$ in the sense that C_p presents the lower value at the station $Y_H = -1.0$, and increases monotonically upward along the surface, reaching the peak value at the corner, $Y_H = 0$. It may be inferred in passing that this is an expected behavior since the flow within the cavity is characterized by the appearance of a recirculation region. According to Figure 5.5, the streamline pattern shows that the flow is characterized by a primary vortex system for $L/H = 1$ and 2 cases, where a clockwise recirculation structure fills the entire cavities. Conversely, for the $L/H = 3$ and 4 cases, the flow is characterized by two vortex systems at the vicinity of the surfaces $S2$ and $S4$, with the freestream flow reaching the cavity floor, surface $S3$.

In the following, it proves instructive to compare the maximum values for the pressure coefficient observed in the cavities with that of a smooth surface, i.e., a flat-plate without a cavity. As a basis of comparison, for the $L/H = 4$ case, the pick values for C_p is around 0.092 and 0.193 observed at the cavity floor, surface $S3$, and at the cavity corner, surface $S4$, respectively. For the flat-plate case, the maximum value for C_p is around to 0.0392 at a station $23.9\lambda_\infty$ from the leading edge along surface $S1$. Therefore, the C_p peak values for the largest cavity are around 2.3 and 4.9 times larger than the peak value for a smooth surface.

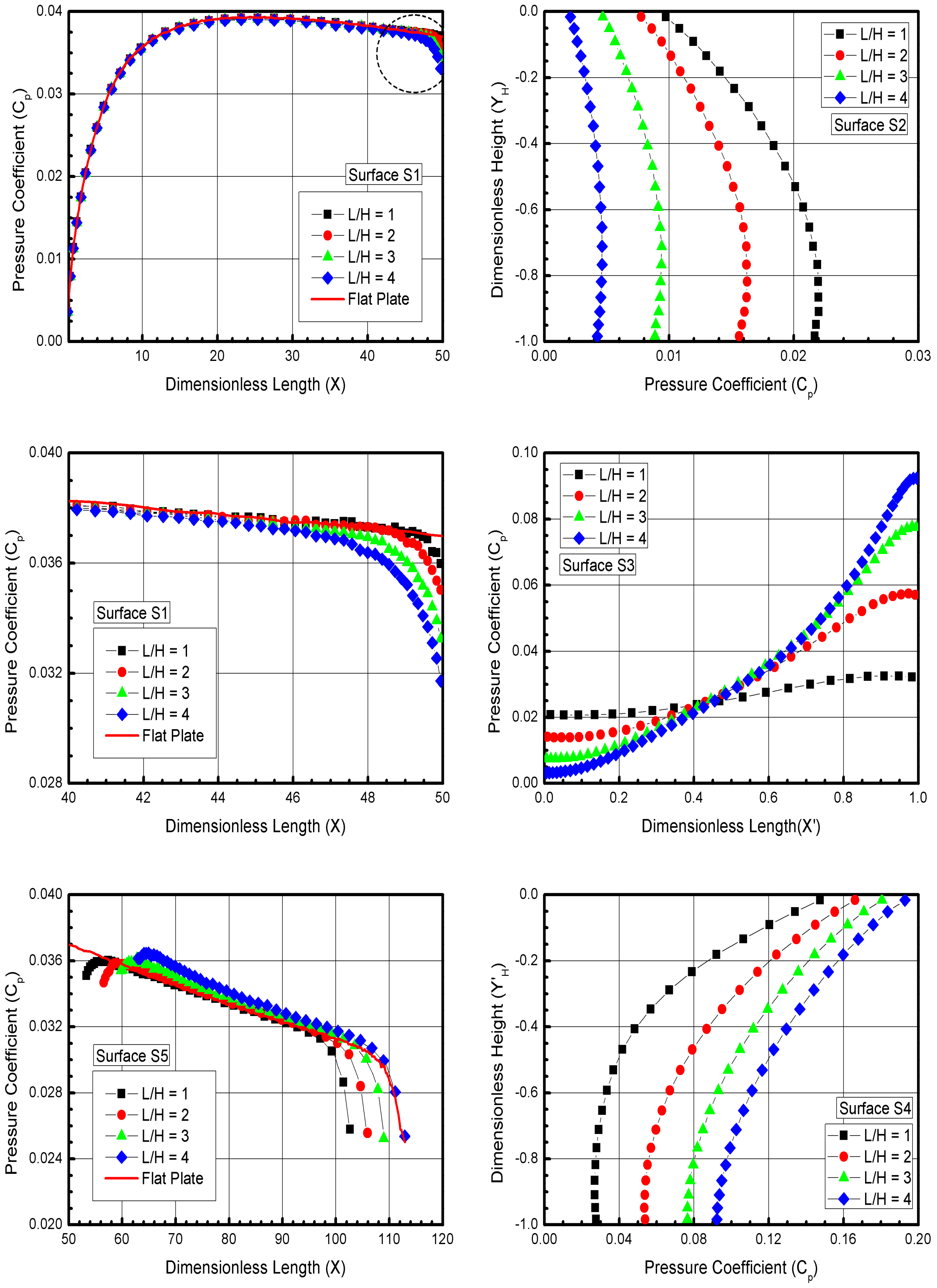

FIGURE 5.21 - Pressure coefficient C_p along the cavity surfaces as a function of the L/H ratio.

5.2.4 Skin Friction Coefficient

The skin friction coefficient C_f is defined as follows,

$$C_f = \frac{\tau_w}{1/2\rho_\infty U_\infty^2} \tag{5.12}$$

where the shear stress τ_w on the cavity surface is calculated by the sum of the tangential momentum fluxes of both incident and reflected molecules impinging on the surface at each time step by the following expression,

$$\tau_w = \tau_i + \tau_r = \frac{1}{A\Delta t}\sum_{j=1}^{N}[m_j u_j]_i + [m_j u_j]_r \tag{5.13}$$

where u is the velocity component of the molecule j in the surface tangential direction.

It is worthwhile to note that for the special case of diffuse reflection, the gas-surface interaction model adopted in present work, the reflected molecules have a tangential moment equal to zero, since the molecules essentially lose, on average, their tangential velocity components. In this fashion, the net tangential momentum flux is defined as follows,

$$\tau_w = \tau_i = \frac{1}{A\Delta t}\sum_{j=1}^{N}[m_j u_j]_i \tag{5.14}$$

The impact on the skin friction coefficient C_f due to changes on the cavity L/H ratio is demonstrated in Figure 5.22. According to the left-column plots in this figure, it is firmly established that the skin friction coefficient C_f follows a similar behavior of that presented by the heat transfer coefficient C_h. Along the surface $S1$, it is observed that C_f reproduces the skin friction distribution for the flat-plate case. In addition, broadly speaking, no upstream disturbance, due to the presence of the cavities, is observed, as is apparent from the magnified view in the middle plot. Along the surface $S5$, similar to the heat transfer coefficient, it is noticed that the skin friction coefficient C_f is larger than that for the flat-plate case, especially at the vicinity of the downstream corner of the cavity, defined by the surface-$S4$/surface-$S5$ junction. Nevertheless, as the flow moves downstream along the surface, the skin friction coefficient C_f basically recovers the value observed for the flat-plate case. Finally, it may be inferred that the peak values for the skin friction coefficient along surfaces $S1$ and $S5$ are larger than those observed for the pressure coefficient. As a result, tangential forces, associated to the shear stress, are larger than normal forces, related to the wall pressure.

Turning to right-column plots, for the back face, surface $S2$, it is observed that the skin friction coefficient presents the peak value at the corner, $Y_H = 0$, then it decreases downward along the surface up to station $Y_H \approx -0.75$, and becomes negative along the remaining part of the surface. In what follows, for the cavity floor, surface $S3$, the skin friction coefficient behavior relies on the L/H ratio. It is negative near the vicinity of the surface-$S2$/surface-$S3$ junction, then becomes positive and reaches a maximum value as a function of the L/H ratio. Due to the recirculation region inside the cavities, along the surface $S3$, the skin friction coefficient distribution is similar for the $L/H = 1$ and 2 cases. In addition, the distribution for the $L/H = 3$ case presents a similar behavior as that for the $L/H = 4$ case. Along the frontal face, surface $S4$, the skin friction coefficient increases negatively upward along the entire surface.

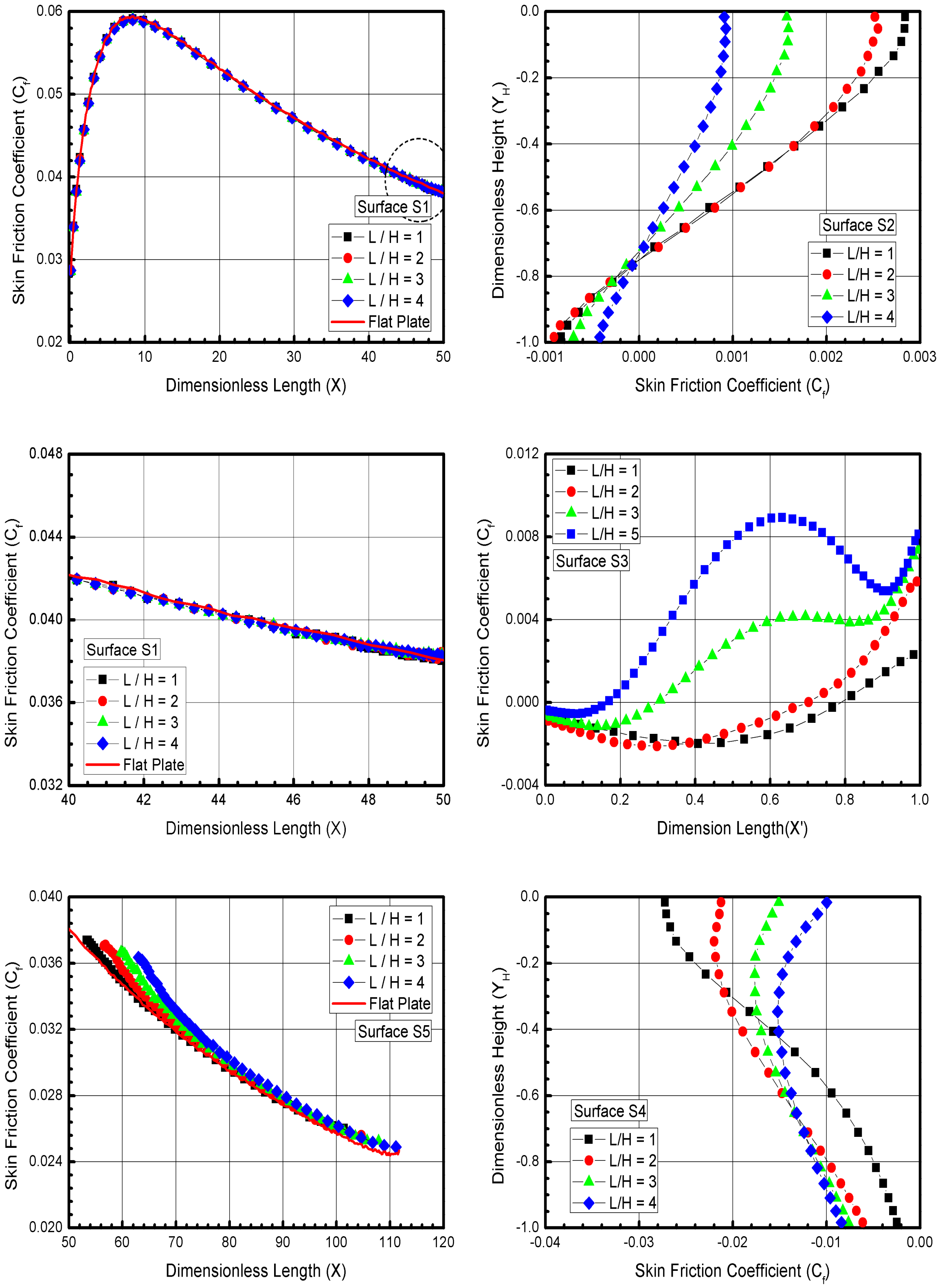

FIGURE 5.22 - Skin friction coefficient C_f distribution along the cavity surfaces as a function of the L/H ratio.

6 CONCLUSIONS

6.1 Concluding Remark

Through the use of the Direct Simulation Monte Carlo (DSMC) method, the flowfield structure and the aerodynamic surface quantities on cavities have been investigated. The calculations provided information concerning the nature of the flow on cavities resulting from variations in the length-to-depth (L/H) ratio for the idealized situation of two-dimensional rarefied hypersonic flow. A very detailed description of the flowfield properties, such as velocity, density, pressure, and temperature, and aerodynamic surface quantities, such as number flux, heat transfer, pressure and skin friction, were presented separately outside and inside the cavities by a numerical method that properly accounts for non-equilibrium effects. Performance results for cavities, defined by L/H ratio of 1, 2, 3, and 4, were compared to those of a flat-plate without cavities.

It was observed that the cavity L/H ratio did not disturbed the flowfield far upstream and far downstream, as compared to the freestream mean free path, and the domain of influence along the upstream and downstream surfaces increased with increasing the L/H ratio.

One of the main findings of this research is related to the flow topology inside the cavities. The analysis showed that the recirculation region inside the cavities is a function of the L/H ratio. It was found that for the $L/H = 1$ and 2 cases, the flow structure was characterized by a primary vortex system, with the recirculation region filling the entire cavities. For the $L/H = 3$ and 4 cases, it was observed the formation of two vortices. However, the external stream reached the bottom surface of the cavity only for the $L/H = 4$ case. As a result, the flow topology observed for the $L/H = 1$ and 2 cases corresponded to that of an "open cavity", as defined in the continuum flow regime. Conversely, the flow topology for the $L/H = 4$ case corresponded to that of a "closed cavity", usually observed in the continuum flow regime for $L/H > 14$.

Another issue that stimulated this study was the heat flux and pressure acting on the cavity surfaces. Results showed that both depends on the L/H ratio. It was found that the peak values for the heat transfer coefficient C_h took place on the cavity frontal face, and they were more than twice of the maximum value observed for a smooth surface, i.e., a flat-plate without a cavity. A similar behavior was found for the pressure loads. The peak value for the pressure coefficient C_p occurred at the frontal face for the largest cavity, and it was around 4.9 times larger than the peak value for a smooth surface.

6.2 Future Work

The present work has described an initial investigation of a hypersonic rarefied flow over cavities in order to simulate discontinuities or defects present on hypersonic vehicle surfaces. Although this investigation has taken into account a representative range for the L/H ratio, a number of improvements to a realistic investigation on surface discontinuities is still desirable.

First on the list is to incorporate a new model for the gas-surface interaction. The diffuse reflection model employed in this research assumes that the molecules are reflected equally in all directions, quite independently of their incident speed and direction. Nevertheless, as a space flight vehicle is exposed to a rarefied environment over a considerable time, a departure from the fully diffuse model is observed, resulting from the colliding molecules that clean the surface of the vehicle, which becomes gradually decontaminated. Molecules reflected from clean surfaces show lobular distribution in direction. In this scenario, incomplete surface accommodation effects might provide more insight into the sensitivity of the aerothermodynamic surface quantities to gas-surface model.

The DSMC method has been used to assess the flowfield structure on cavities by considering constant wall temperature. In a realistic design, temperature not only changes along the body surface but also inside the cavities. In this context, a more detailed analysis that includes the conjugate heat transfer problem seems to be challenge.

Finally, the Mach number effect, the angle-of-attack effect as well as the geometrical effect, i.e., the axisymmetric cavity, might be included in this list.

REFERENCES

ABE, T. Rarefied gas flow analysis by direct simulation monte carlo method in body-fitted coordinate system. **Journal of Computational Physics**, v. 83, p. 424–432, 1989. 41

_____. Generalized scheme of the no-time-counter scheme for the dsmc in rarefied gas flow analysis. **Computer Fluids**, v. 22, n. 2, p. 253–257, 1993. 19, 24

ALDER B. J.; WAINWRIGHT, T. E. Studies in molecular dynamics. **Journal of Chemical Physics**, v. 27, p. 1208–1209, 1957. 14

ALDER, S. F. B.; ROTENBERG, M. **Method of computational physics: the solution of two molecular flow problem by the Monte Carlo method**. New York: Academic Press, 1965. 109–209 p. 14

ALEXANDER, F. J.; GARCIA, A. L.; ALDER, B. J. Cell size dependence of transport coefficients in stochastic particle algorithms. **Physics of Fluids**, v. 10, n. 6, p. 1540–1542, 1998. 16

_____. Erratum: Cell size dependence of transport coefficient in stochastic particle algorithms. **Physics of Fluids**, v. 12, p. 731–731, 2000. 16

ANDERSON, J. D. **Hypersonic and high temperature gas dynamics**. New York: McGraw-Hill, 1989. 4

BAGANOFF D.; MCDONALD, J. D. A collision-selection rule for particle simulation method suited to vector computers. **Physics of Fluids A - Fluid Dynamics**, v. 2, n. 7, p. 1248–1259, 1990. 26

BECKER, D.; ROBBEN, F.; CATTOLICA, R. Velocity distribution function near the leading edge of a flat plate. **AIAA Journal**, v. 12, n. 9, p. 1247–1253, 1974. 44, 52

BERGEMANN F.; BOYD, I. D. Rarered gas dynamics: theory and simulation: new discrete vibrational energy model for the direct simulation Monte Carlo. In: SHIZGAL, B. D.; WEAVER, D. P. (Ed.). **Progress in Astronautics and Aeronautics**. Washington, DC: AIAA, 1994. p. 174–183. 32

BERTRAN, M. H.; WEINSTEIN, L. M. C. J.; M., A.; ARRINGTON, J. P. Heat transfer to wavy wall in hypersonic flow. **AIAA Journal**, v. 5, n. 10, p. 1760–1767, 1967. 1, 4, 5

BERTRAN M. H.; WIGGS, M. M. Effect of surface distortions on heat transfer to a wing at hypersonic speeds. **AIAA Journal**, v. 1, n. 6, p. 1313–1319, 1963. 1, 4, 5

BIRD, G. A. **Molecular gas dynamics**. Oxford: Clarendon Press, 1976. 14, 15, 19, 24, 25, 26

_____. Rarefied gas dynamics: Monte carlo simulation in a engineering context. **AIAA Journal**, v. 74, p. 239–255, 1981. 21

_____. Definition of mean free path for real gases. **Physics of Fluids**, v. 26, n. 11, p. 3222–3223, 1983. 37

_____. Direct simulation of hight-vorticity gas flow. **Physics of Fluids**, v. 30, n. 2, p. 364–366, 1987. 16

_____. Rarefied gas dynamics: theorical and computational techniques. In: MUNTZ, D. P. W. E. P.; CAPBEL, D. H. (Ed.). **Progress in astronautics and aeronautics**. Washington, DC.: AIAA, 1989. p. 374–395. 19, 24

_____. **Molecular gas dynamics and the Direct Simulation Monte Carlo of gas flow**. Oxford: Clarendon Press, 1994. 14, 15, 16, 17, 32, 36, 38, 42, 49, 96

_____. **The DS2G program user´s guide**. Australia: N.S.W Killara, 1999. 43

BORGNAKKE C.; LARSEN, P. Statiscal collision model for monte carlo simulation of a polyatomic gas mixture. **Journal of Computational Physics**, v. 18, p. 405–420, 1975. 30, 36

BOYD, I. D. Monte carlo study of vibrational relaxation process. In: **International Symposium on Rarefied Gas Dynamics**. Aachen: A. E. Beylic, 1990. p. 792–799. 32

_____. Rotational and vibrational relaxation nonequilibrium effects in rarefied hypersonic flow. **Journal of Thermophysics and Heat Transfer**, v. 4, n. 4, p. 478–484, 1990. 31

_____. Rotational-tranlational energy transfer in rarefied nonequilibrium flows. **Physics of Fluids A - Fluid Dynamics**, v. 2, n. 3, p. 447–452, 1990. 31

_____. Analysis of rotational nonequilibrium in standing shock waves of nitrogen. **AIAA Journal**, v. 28, n. 11, p. 1997–1999, 1990a. 31

_____. Analysis of vibrational-translational energy transfer using the direct simulation monte carlo method. **Physics of Fluids A - Fluid Dynamics**, v. 3, n. 7, p. 1785–1791, 1991. 32

BURNETT, D. The distribuition of molecular velocities and the mean motion in a non-uniform gas. **Proceedings of the London Mathematical Society**, v. 40, p. 382–435, 1936. 13

CERCIGNANI, C. **The Boltzmann equation and its applications**. New York: Springer-Verlag, 1988. 15

CERCIGNANI C.; FREZZOTTI, A. Rarefied gas dynamics: theorical and computational techniques. In: MUNTZ, D. P. W. E. P.; CAMPBELL, D. H. (Ed.). **Progress in astronautics and aeronautics**. Pasadena, CA: AIAA, 1989. p. 552–566. 14, 36, 44, 52, 54

CHAPMAN, D. R.; KUEHN, D. M.; LARSON, H. K. Investigation of separeted flow in supersonic and supersonic streams with emphasis on the effect of transition. **NACA Report**, n. 1356, 1958. 4, 5

CHAPMAN S.; COWLING, T. G. **The matematical theory of non-uniform gases**. London: Cambridge University Press, 1970. 13

CHARBONNIER J.; BOERRIGTER, H. Contribution to the study of gap induced boundary layer transition in hypersonic flow. In: **Proceedings of the International Aerospace Plane and Hypersonics Technologies Conference**. Munich: [s.n.], 1993. 4, 5

CHARWAT, A. F. Separation of a supersonic accelerated flow over notches. **AIAA Journal**, v. 9, p. 1656–1657, 1971. 4, 5

CHARWAT, A. F.; DEWEY, C. F.; ROSS, J. N.; HITZ, J. A. An investigation of separated flows - part 1: the pressure field. **Journal of Aerospace Sciences**, v. 28, p. 457–470, 1961. 4, 5

_____. An investigation of separated flows - part 2: flow in the cavity and heat transfer. **Journal of Aerospace Sciences**, v. 28, p. 513–527, 1961. 4, 5

CHENG H. K.; EMMANUEL, G. Perspective on hypersonic non-equilibrium flows. **AIAA Journal**, v. 33, n. 3, p. 385–400, 1995. 14

CHENG M.; HUNG, K. C. Vortex structure of steady flow in a rectangular cavity. **Computer and Fluids**, v. 35, p. 1046–1062, 2006. 4, 5

COMEAUX, K. A.; MACCOMARCK, R. W.; CHAPMAN, D. R. An analysis of the burnett equations based on the second law of themodynamics. In: **Proceedings AIAA Aerospace Sciences Meeting and Exhibit**. Reno: [s.n.], 1995. p. 382–435. 13, 14

DIETRICH, S. Efficient computational of particle movement in 3d dsmc calculations on structured body-fitted grids. In: **Proceedings of the International Symposium on Rarefied Gas Dynamics**. Aechen: A. E. Beylich, 1990. p. 745–752. 17

EVERHART, J.; ALTER, S. J.; MERSKI, N. R.; WOOD, W. A. Pressure gradient effects on hypersonic flow heating. In: **Proceedings of the AIAA Aerospace Sciences Meetings an Ehhibit**. Reno: [s.n.], 2006. p. 2241–2268. 1, 4, 5, 7, 35

FISCKO K. A.; CHAPMAN, D. R. Hypersonic shock structure with burnett terms in the viscous stress and heat transfer. In: **Proceedings of the AIAA Thermophysics, Plasmadynamics and Lasers Conference**. San Antonio: [s.n.], 1988. 13

GAI S.; MILTHORPE, J. F. Hypersonic high-enthalpy flow over a blunt-stepped cone. In: **Proceedings of the International Symposium on Shock Wave**. [S.l.]: B. Sturtevant and J. E. Shepherd and H. G. Hornung, 1995. p. 234–244. 4, 5, 35

GARCIA A. L.; WAGNER, W. Time step trucation error in direct simulation monte carlo. **Physics of Fluids**, v. 12, p. 2621–2633, 2000. 17

GROTOWSKY I. M. G.; BALLMANN, J. Numerical investigation of hypersonic step-flows. **Shock Waves**, v. 10, p. 57–72, 2000. 4, 5, 35

GRUPTA, R. N.; SCOTT, C. D.; MOSS, J. N. Surface-slip equations for low reynolds number multicomponet air flow. In: **Progress in astronautics and aeronautics**. [S.l.]: H. F. Nelson, 1985. p. 465–490. 97

HADJICONSTANTINOU, N. Analysis of discretization in the direct simulation monte carlo. **Physics of Fluids**, v. 12, n. 10, p. 2634–2638, 2000. 17

HAHN, M. Experimental investigation of separated flow over a cavity at hypersonic speed. **AIAA Journal**, v. 7, n. 6, p. 1092–1098, 1969. 1, 4, 5

HARVEY, J. K. Rarefied gas dynamics: thermophysical aspect of re-entry flow. **Physics of Fluids**, v. 103, n. 37, p. 253–257, 1986. 15

HARVEY J. K.; GALLIS, M. A. A review of the code validation studies in hight-speed low-density flow. **Journal of Spacecraft and Rockets**, v. 37, n. 1, p. 8–20, 2000. 15

_____. A review of a validation exercice on the use of a dsmc method to compute viscous/inviscid interactions in hypersonic flow. **AIAA Journal**, n. 3643, 2003. 15

HASH, D. B.; MOSS, J. N.; HASSAN, H. A. A direct simulation of diatomic gases using the generalized hard sphere model. **Journal of Themophysics and Heat Transfer**, v. 8, n. 4, p. 758–764, 1993. 24

HASSAN H. A.; HASH, D. B. A generalized hard-sphere model for monte carlo simulation. **Physics of Fluids A - Fluid Dynamics**, v. 5, n. 3, p. 738–744, 1993. 24

HAVILAND J. K.; LAVIN, M. L. Application of monte carlo method to heat transfer in rarefied gases. **Physics of Fluid**, v. 5, p. 1399–1405, 1962. 14

HERMINA, W. L. Monte carlo simulation of rarefied gas flow along a flat plate. **Journal Thermophysics and Heat Transfer**, v. 3, n. 1, p. 7–12, 1989. 44, 52, 54

HINDERSKS M.; RADESPIEL, R. Simulation of hypersonic gap flow with consideration of fluid structure interation. In: **Proceedings of the Fluid Dynamics Conference and Exhibit**. Portland: AIAA, 2004. p. 2238. 4, 5

_____. Investigation of hypersonic gap flow of a reentry nosecap with consideration of fluid structure interaction. In: **Proceedings of the AIAA Aerospace Sciences Meetings an Ehhibit**. [S.l.: s.n.], 2006. p. 2288–2300. 1, 4, 5, 35

HOLDEN M. S.; WADHAMS, T. P. A review of experimental studies for dsmc and navier-stokes code validation in laminar regions of shock/shock and shock/boundary layer interaction including real gas effects in hypersonic flows. **AIAA Journal**, p. 3641, 2003. 15

HOZUMI, K.; KOYAMA, T.; HIRABAYASHI, N. Experimental study on hypersonic heating characteristics of cavity wake flow. In: **Proceedings of the International Congress of the Aeronautical Sciences**. [S.l.: s.n.], 2004. 4, 5, 35

HURLBULT, F. C. Monte carlo simulation of rerefied flow along a flat plate. **Journal Thermophysics and Heat Transfer**, v. 3, n. 1, p. 7–12, 1989. 54

_____. Sensivity of hypersonic flow to wall/gas interaction models using dsmc. **Journal Thermophysics and Heat Transfer**, v. 3, n. 4, p. 374–379, 1989. 44

JACKSON, A. P.; HILLIER, R.; SOLTANI, S. Experimental and computational study of laminar cavity flows at hypersonic speeds. **Journal of Fluid Mechanics**, v. 427, p. 329–358, 2001. 4, 5, 35

JAKUBOWKI A. K.; LEWIS, C. H. Experimental study of supersonic laminar base flow with and without suction. **AIAA Journal**, v. 11, n. 12, p. 1670–1677, 1973. 1

KANNENBERG K. C.; BOYD, I. Strategies for efficient particle resolution in the direct simulation monte carlo method. **Journal of Computational Physics**, v. 157, p. 727–745, 2000. 42

KOURA K.; MATSUMOTO, H. Variable soft sphere molecular model for inverse-power-law of leonard-jones potential. **Physics of Fluids A - Fluid Dynamics**, v. 3, n. 10, p. 2459–2465, 1991. 19, 24

_____. Variable soft sphere molecular model for air species. **Physics of Fluids A - Fluid Dynamics**, v. 4, n. 5, p. 1083–1085, 1992. 24

KUNC, J. A.; HASSAN, H. A.; HASH, D. B. The ghs interaction model for strong attractive potentials. **Physics of Fluids**, v. 7, n. 3, p. 1173–1175, 1995. 24

LAUX, M. Optimization and parallelization of the dsmc method on unstructured grids. In: **Proceedings of the AIAA Thermophysics Conference**. Atlanta: [s.n.], 1997. p. 364–366. 17

LEE, C. J. Unique determination of solutions to the burnett equations. **AIAA Journal**, v. 32, n. 5, p. 985–990, 1994. 13

LEE G.; CHANDRA, S. Numerical analysis of heat transfer enhancement from surfaces with cavities. In: **Proceedings of the AIAA Aerospace Sciences Meeting and Exhibit**. [S.l.: s.n.], 2006. p. 2269–2277. 4, 5

LORD, R. Application of the cercignani-lampis scattering kernel to direct dimulation monte carlo method. In: **Proceedings of the International Symposium on Rarefied Gas Dynamics**. Aachen: A. E. Beylich, 1991. p. 1427–1433. 53

______. Direct simulation of rarefied hypersonic flow over a flat plate with incomplete surface accomodation. In: SHIZGAL, B. D.; WEAVER, D. P. (Ed.). **Progress in astronautics and aeronautics**. Stuttgard, Germany: AIAA, 1994. p. 221–228. 44, 53, 54

LUMPKIN, F. E.; HASS, B. L.; BOYD, I. D. Resolution of differences between collision number definitions and continuum simulations. **Physics of Fluids A - Fluid Dynamics**, v. 3, n. 9, p. 2282–2284, 1991. 31

MACHADO, H.; DANTON.; BOAS, J. Calculo da pressão em superfícies sujeitas a aquecimento aerodinâmico. In: **Proceedings of the Brazilian Congress of Thermal Sciences and Engineering**. [S.l.]: Brasilian Society of Mechanical Sciences and Engineeting, 2006. 39

MORGENSTERN A.; CHOKANI, N. Hypersonic flow past open cavities. **AIAA Journal**, v. 32, n. 12, p. 2387–2393, 1994. 1, 4, 5, 6

NAMBU, K. Theorical basis of the direct simulation monte carlo method. In: **Proceedings of the International Symposium on Rarefied Gas Dynamics**. Stuttgard: [s.n.], 1986. 19, 24

NANCE, R. P.; WILMOTH, R. G.; HASSAN, H. A. Comparison of grid-definition schemes for monte carlo simulations. **Journal of Thermophysics and Heat Transfer**, v. 11, n. 2, p. 296–303, 1997. 17, 41

NARIS S.; VALOUGEORGIS, D. The driven cavity flow over the whole range of the knudsen number. **Physics of Fluids**, v. 17, n. 9, p. 1–2, 2005. 4, 5

NESTLER, D. E. An experimental study of hypersonic cavity flow. **Journal of Spacecraft and Rockets**, v. 19, n. 3, p. 195–196, 1982. 1

NESTLER, D. E.; SAYDAH, A. R.; AUXER, W. L. Heat transfer to steps and cavities in hypersonic turbulent flow. **AIAA Journal**, v. 7, n. 7, p. 1368–1370, 1969. 1, 4, 5

OLYNICK, D. P.; MOSS, J. N.; HASSAN, H. A. Grid generation and adaptation for direct simulation monte carlo method. **Journal of Thermophysics and Heat Transfer**, v. 3, n. 4, p. 368–373, 1989. 41

PLENTOVICH, E. B.; STALLINGS, R. L.; TRACY, M. B. **Experimental cavity pressure measurements at a subsonic and transonic speeds**. 1993. 4, 5, 7

RAULT, D. F. G. Aerodynamic of the shuttle orbiter at hight altitude. **Journal of Spacecraft and Rockets**, v. 31, n. 6, p. 944–952, 1994. 41

RIEFFEL, M. A. A method for estimating the computational requirements of dsmc simulations. **Journal of Computational Physics**, v. 149, p. 95–113, 1999. 43

ROWLEY, C. W. W. D. R. Dynamics control of high-reynolds-number flow over open cavities. **Journal of Fluid Mechanics**, v. 38, p. 251–276, 2000. 4, 5

SHANKAR P. N.; DESHPANDE, M. D. Fluid mechanics in the driven cavity. **Journal of Fluid Mechanics**, v. 32, p. 93–136, 2000. 4, 5

SHU, C.; MAO, X.; CHEW, Y. Particle number per cell and scalling factor effect on accuracy of dsmc simulation of micro flows. **International Jornal of Numerical Methods for Heat and Fluid Flows**, v. 15, n. 8, p. 827–841, 2005. 43

TANNEHILL J. C.; EISLER, G. R. Numerical computation of the hypersonic leading edge problem using the burnett equations. **Physics of Fluids**, v. 19, n. 1, p. 09–15, 1976. 13

USAMI M.; NAKAYAMA, T. Intermolecular collision scheme of dsmc taking molecular locations within a cell into account. In: **Proceedings of the International Symposium on Rarefied Gas Dynamics**. [S.l.: s.n.], 2003. p. 374–384. 17

WAINWRIGHT, T. E. A. B. J. Molecular dynamics by electronic computers: transport processes in statistical mechanics. In: INTERNATIONAL SYMPOSIUM ON TRANSPORT PROCESSES IN STATISTICAL MECHANICS, 1956, Brussels. **Transport Processes in Statistical Mechanic**. New York: Wiley Interscience, 1958. p. 97–131. 14

WILMOTH, R. G.; LEBEAU, G. J.; CARLSON, A. B. Dsmc grid methodologies for computing low-density, hypersonic flow about reusable launch vehicles. In: **Proceedings of the AIAA Thermophysics Conference**. New Orleans: AIAA, 1996. p. 364–366. 17, 41

ZDANSKI, P. S. B.; ORTEGA, M. A.; FICOJR, N. G. C. R. Heat transfer on shallow cavities: aspect ratio and reynolds number influence. In: **Proceedings of the Applied Aerodynamics Conference and Exhibit**. Providence: [s.n.], 2004. p. 422–442. 4, 5

ZHONG, X.; MCCORMACK, R. W.; CHAPMAN, D. R. Stabilization of the burnet equations and application to hypersonic flow. **AIAA Journal**, v. 31, n. 6, p. 1036–1043, 1993. 13